THE FABRICATION OF DIRECT-WRITE WAVEGUIDES VIA THE GLASSY-STATE PROCESSING OF POROUS FILMS: UV-INDUCED POROSITY AND SOLVENT-INDUCED POROSITY

A Dissertation
Presented to
The Academic Faculty

By

Jassem Abdallah

In Partial Fulfillment
Of the Requirements for the Degree
Master of Science in the
School of Chemical Engineering

Georgia Institute of Technology

August, 2007

THE FABRICATION OF DIRECT-WRITE WAVEGUIDES VIA THE GLASSY-STATE PROCESSING OF POROUS FILMS: UV-INDUCED POROSITY AND SOLVENT-INDUCED POROSITY

Dr. Paul Kohl, Advisor
School of Chemical and Biomolecular Engineering
Georgia Institute of Technology

Dr. Sue Ann Bidstrup-Allen, Co-Advisor
School of Chemical and Biomolecular Engineering
Georgia Institute of Technology

Dr. Amyn Teja
School of Chemical and Biomolecular Engineering
Georgia Institute of Technology

Dr. Dennis Hess
School of Chemical and Biomolecular Engineering
Georgia Institute of Technology

Date Approved: April 13, 2007

ACKNOWLEDGEMENTS

I would like to thank my advisors for the guidance that they provided throughout my research. I would like to acknowledge Marshall Silver for the pivotal role he played in preliminary work, specifically in the assistance he gave me in the design of a basic process for producing direct-write porosity. I would like to thank Takashi Okada, a visiting scientist from JSR, for synthesizing N-methyl nifidepine, purifying its crystals, and verifying their structure using ^{1}H-NMR analysis. I would also like to thank Professor Seth Marder in the Department of Chemistry at the Georgia Institute of Technology for offering advice in synthesizing photobase generators. Martin Brucherseifer of the FIB2 Center at the Georgia Institute of Technology for performed focused ion beam (FIB) services to prepare thin cross-sections of samples prior to TEM analyses. TEM analyses were performed by Yolande Berta using the facilities in the Center of Nanostructure Characterization and Fabrication at the Georgia Institute of Technology. AFM analyses were performed by Dhananjay Bhusari and Xiaohong Zhang using the facilities located in the Microelectronics Research Center located at the Georgia Institute of Technology. I would like to thank Justin Stay, Ricardo Villalaz, and Brent Bachim for assisting me with modeling and determining the propagation losses of fabricated waveguides. I would like to acknowledge the guidance that I received from numerous cleanroom users in the Microelectronics Research Center during the fabrication of the IDEs. I wish to thank Promerus LLC and Dow Corning Corp. for donating the PNC sacrificial polymer and FOx-1x® resin samples, respectively. I would like to acknowledge the financial support received from the STC program of the National Science Foundation under agreement #

DMR-0120967. Lastly, I would like to thank my family and friends for the encouragement and advice that they continually provided.

TABLE OF CONTENTS

LIST OF TABLES

LIST OF FIGURES

LIST OF SYMBOLS

θ_i	The angle of incidence. It is the angle between path of incident light ray and the normal
θ_t	The angle of transmission, which is also the angle of refraction. It is the angle between path of transmitted light ray and the normal after undergoing refraction
θ_c	The critical angle, largest angle of incidence that results in refraction. Also the angle of incidence that produces an angle of refraction of 90^o
θ	Zigzag angle between propagating light rays within a guiding layer and the normal
n_H	Higher refractive index (n_H)
n_L	Lower refractive index (n_L)
n_f	Refractive index of the core in a slab waveguide structure. Since the core always has a higher refractive index than the cladding materials, $n_f = n_H$
n_c	Refractive index of layer above the core in a slab waveguide structure, also known as the cover layer
n_s	Refractive index of layer below the core in a slab waveguide structure, also known as the substrate layer
λ	Wavelength of light
h	Thickness of guiding layer in a slab waveguide
ν	Mode number of an electromagnetic field propagating in a waveguide. They are whole numbers with the 1^{st} mode starting at $\nu = 0$, the 2^{nd} mode at $\nu = 1$, etc.
E_r,	Reduced Modulus of indented films reported in units of 10^9 pascals (GPa)
T_d	Temperature at which thermal degradation begins; at the T_d of a PAG, acid is thermally released without any prior irradiation
T_g	Glass transition temperature
ϕ_2	Volume fraction occupied by air in a porous film, i.e. the induced porosity

ϕ_1	Volume fraction occupied by host matrix in porous film ($1-\phi_2$)
n_{12}	Effective bulk refractive index of a mixed-component film
n_1	Refractive index of host matrix in a porous film, same value as the non-porous control sample
n_2	Refractive index of air ($1.0003 \cong 1$)[1]
ε_{12}	Effective bulk dielectric constant of a porous film
ε_1	Relative dielectric constant of host matrix in a porous film, same value as that of the non-porous control sample
ε_2	Relative dielectric constant of air, equal to unity
z	The distance traveled by light in a waveguide along the direction of mode propagation
P_0	The initial power of the light propagating in a waveguide (i.e. power at a distance of $z = 0$)
P(z)	The power of the light propagating in a waveguide at the point z.
β	Propagation constant of guided mode
$\alpha(cm^{-1})$	The power loss per centimeter of the light propagating in a waveguide in the exponential scale
α(dB/cm)	The power loss per centimeter of the light propagating in a waveguide in units of decibels per centimeter (dB/cm)

LIST OF ABBREVIATIONS

SOG	Spin-on glass
low-k	Low dielectric constant material (has a dielectric constant < 4.0).
Ultra low-k	Material with a dielectric constant < 2.0. Materials usually achieve such low dielectric constants via the incorporation of porosity within the films
HSQ	Hydrogen silsesquioxane
MSQ	Methyl silsesquioxane
TMAH	Tetra-methyl ammonium hydroxide
SiO_2	Silicon dioxide
CMOS	Complimentary metal-oxide-semiconductor
XLK	Tradename for porous HSQ films made using Dow Corning's patented process
TEOS	Tetra-ethoxy silane
PECVD	Plasma-enhanced chemical vapor deposition
MIBK	Methyl isobutyl ketone
FOx-1x®	Flowable oxide (a commercial resin of HSQ in MIBK solvent)
PNC	Poly(norbornene carbonate)
PAG	Photoacid generator (a photoinitiator that releases an acid when excited by radiation)
TIR	Total internal reflection, phenomena of light being reflected at the boundary of two interfaces due to the angle of incidence exceeding the critical angle
HTPFPB	Hydrogen tetrakis(perflourophenyl)borate
TTBPS-Tf	tris(tert-butyl phenyl)sulfonium triflate
TTBPS-Nf	tris(tert-butyl phenyl)sulfonium nonaflate

PBG	Photobase generator (a photoinitiator that releases a base when excited by radiation)
CTS	N-cyclohexl-*p*-toluene sulfonamide
NBC	*o*-nitrobenzyl cyclohexylcarbamate
TGA	Thermogravimmetric analysis
FTIR	Fourier transform infrared spectroscopy
ATR	The attenuated total reflectance mode of FTIR analysis
S_ni-Si	The mechanism, proposed by Sommer to describe his hypothesis of how silane bonds are hydrolyzed to form silanol bonds[2]
c/n	The ratio of the areas underneath the FTIR peaks corresponding to cage-type siloxane and network-type siloxane, respectively
GPA	10^9 pascals
DUV	Deep ultraviolet radiation
PEB	Post-exposure bake
EMA	Effective medium Approximation, an optical or dielectric models used to predict the effective properties of multi-component materials
DSC	Differential scanning calorimetry
IDE	Interdigitated electrodes
UV-VIS	Ultraviolet-visible light spectroscopy
AFM	Atomic force microscopy
rms	Root mean square, the value of the standard deviation of a distribution
FIB	Focused ion beam
TEM	Transmission electron microscopy
keV	Kiloelectron volts; a unit of energy equivalent to 1.602×10^{-6} Joules
PC	Propylene Carbonate

THF	Tetrahydrofuran
NMP	N-Methyl-2-pyrrolidinone
GBL	Gamma-butyrolactone
sccm	Standard cm^3; a unit of measuring volumetric flowrates of gases
N_{eff}	Effective indices
dB/cm	Decibels per centimeter

SUMMARY

Two processing techniques were developed to produce porosity in thin dielectric films at temperatures below the glass transition temperature of the host matrix. These glassy-regime processing methods relied on the susceptibility of hydrogen silsesquioxane (HSQ) to gelation in the glassy regime when exposed to polar substances. The processing time for both glassy-state porosity methods was about 50 minutes, which is shorter than most of the traditional techniques for producing porous films (typically at least 2 hours).

The first method used UV-radiation to initiate acid-catalyzed decomposition of photodefinable sacrificial polymers after first using bases to catalyze the gelation of HSQ. The UV-initiated (direct-write) process was used to selective incorporate of porosity and tune the optical and dielectric properties of spin-on glass (SOG) dielectric films. The direct-write process offered the advantage of lower processing temperatures as well as processing times shorter than traditional techniques based on thermally-induced decomposition of sacrificial polymers. The direct-write process presented used UV-generated acids to catalyze the decomposition of sacrificial polymers templated in a crosslinked matrix resulting in the formation of porosity and the decrease of refractive index in irradiated regions. In unexposed areas, no acid molecules were generated, thus these areas remained non-porous and their refractive index remained relatively high compared with the porous regions. Base-catalyzed gelation was used to crosslink the matrix at temperatures well below its glass transition temperature in order to avoid thermally-induced generation of acids. After crosslinking the matrix, deep ultraviolet (DUV) radiation was used to initiate the direct-write reactions thus creating a refractive

index profile within the film. A blanket UV-exposure followed by immediate quenching of the acid using a base was used to deactivate the system. Depending on the loadings of photobase generator (PBG), photoacid generator (PAG), and porogen, the amount of porosity induced was estimated to be as high as 23%. Transmission electron microscopy (TEM) imaging showed that elongated closed-cell mesopores (measuring 10 nm by about 20-30 nm), and elongated closed-cell macropores (measuring 100 nm by about 200 nm in size) were produced within the internal structure of direct-written films.

Additionally, a process was developed for creating solvent-induced porosity in thin HSQ films using organic solvents with large dipole moments. The process relied on the susceptibility of HSQ to sol-gel hydrolysis and condensation reactions in the presence of polar organic solvents even at temperatures as low as ambient. HSQ films were soaked in co-solvent mixtures and as the solvents penetrated the films, they initiated the low-temperature crosslinking of the HSQ matrix. Afterwards the gelled films were heated to volatilize the entrapped solvents, leaving behind pores within the rigid matrix. Porosities as high as 30 vol% were achieved, and since the co-solvents used were completely miscible, a wide range of co-solvent compositions could potentially be used to vary the amount of induced porosity within films. The processing time for producing co-solvent-produced porosity was about 50 minutes, and the temperatures needed to form porosity ranged from 120-150^{o}C. In contrast, porosity methods that use thermal decomposition of sacrificial polymers usually require processing times of at least 2 hours and temperatures well above 250^{o}C in order to decompose the porogen.[5, 6, 14, 16-19] AFM studies showed the solvent-induced porous films were relatively smooth, without any of

the surface roughness effects observed when sacrificial polymers were used as pore-generators

Glassy-state processing of porous films was used to build the two types of slab waveguide structures, called type I and type II depending on the type of slab waveguide structure fabricated. For both types of waveguides, the solvent-processed porous films were the lowest layers while the direct-written porous films served as topmost slab layers. For the type I waveguides, the direct-write layer was the guiding layer and air served as the upper-cladding, or cover layer of the waveguides. For type II waveguides, silicon dioxide (SiO_2) layers, which were deposited by plasma enhanced chemical vapor deposition (PECVD), were the guiding layers and the direct-write films were their upper-cladding layers. For both types of waveguides, photomasks were used to selectively expose the direct-write guiding layers during the UV-exposure step such that the unexposed regions remained non-porous and had higher refractive index values than the irradiated porous regions. Thus the photomask patterns allowed lateral refractive index profiles to be created within the direct-write layers of the waveguides. These refractive index profiles directly and indirectly defined the cores (highest index areas) and side-cladding areas of the guiding layers of the type I and type II waveguide structures, respectively.

For type I waveguides, the non-porous regions acted as the waveguide cores since these regions had the highest refractive index values (other regions were either porous or occupied by air). The UV-induced porous regions were the side-cladding areas, since they were laterally adjacent to the cores. For type II waveguides, the cores and side-cladding areas were situated in the SiO_2 layers and directly below the non-porous and

porous areas of the direct-write films, respectively. The reason that the direct-write patterning was able to define core and side-cladding regions within the SiO_2 below them was due to their influence on the effective refractive index of the entire waveguides.

Optical characterization experiments showed that type I and type II porous waveguides had average propagation losses of 16 - 27 dB/cm for the first guided TE mode and about 36-40 dB/cm, for the second guided mode. It is believed that the large propagation loss values were caused by a combination of the Rayleigh scattering from the relatively large UV-induced pores produced in the direct-write layers as well as scattering induced by surface roughness. The UV-induced macropore sizes were likely a result of structural changes caused by film shrinkage caused by gelation. If film shrinkage is reduced or eliminated, this may result in smaller pore sizes, and thus reduce the attenuation due to Rayleigh scattering. More work needs to be done in order to identify suitable materials and processing conditions that may allow direct-write porous waveguides to be fabricated with low (< 2 dB/cm) propagation losses.

INTRODUCTION

The incorporation of porosity in a material potentially results in the changes in electrical, mechanical and electrical properties (eg. lowering of dielectric constant, enhancement in flexibility and crack-resistance, and the lowering in refractive index) and has generated much interest by researchers.[3-16] Porous thin films have found wide use in the microelectronics industry due to their low dielectric constant properties, which allow them to replace silicon dioxide as an intralevel dielectric material. The development of new techniques for inducing porosity in thin films may prove advantageous if they lead to a decrease in processing complexity, or an increase in the processing flexibility by widening the window of compatible physical conditions, or improving the final properties of the porous materials. The final physical properties of porous films are dependent on the pore structure characteristics, such as the total amount of porosity, the pore sizes and pore size distribution, and presence or absence of pore interconnectivity.[4, 5, 10, 16] The differences in the morphology of the final pore structure are a result of variations in physical conditions used when fabricating porous films; important factors include the type of porogen used, the porogen loading, presence or absence of phase segregation of porogen during processing, and the processing temperatures required.[16]

Although a variety of methods exist for producing porous films, the majority of these techniques require high processing temperatures to crosslink the host matrix prior to pore formation and/or to remove the pore-generator (porogen). This thesis describes two techniques that were developed to produce porosity in thin dielectric films at temperatures below the glass transition temperature of the host matrix. These glassy-

regime processing methods for producing porosity rely on the susceptibility of hydrogen silsesquioxane to gelation in the glassy regime when exposed to polar substances.

The first method used UV-radiation to initiate acid-catalyzed decomposition of photodefinable sacrificial polymers after first using bases to catalyze the gelation of HSQ. This radiation-based (direct-write) method of decomposing photodefinable polymers had several advantages over the traditional method of thermally decomposing templated sacrificial polymers at high temperature. By using radiation to induce the decomposition of templated polymer chains, the processing temperature required to produce porosity was decreased, which led to a decrease in the overall processing time since there was no need to ramp a furnace to a high temperature to initiate polymer decomposition. Lower processing temperatures potentially allow organic substrates to be used as well as reduce tendency for polymers to phase segregate during the procedure. Furthermore, UV-induced decomposition enables the patterning of porosity in selective areas of the exposed films i.e. lateral patterning of porosity. This patterning capability may be used to make interesting devices in which functionality is dependent on the level of porosity present (eg. phase masks, or lateral confinement in waveguides due induced refractive index profiles).

The second glassy-state processing method for producing porous films made use of non-protic organic co-solvent mixtures to serve both as a gelation catalysts and a pore-generators. The development of this technique was motivated by the discovery that, in addition to aqueous bases, non-protic organic solvents with strong dipoles were efficient catalysts for the low-temperature sol-gel crosslinking of HSQ. Among the advantages of using this processing method, the processing conditions were flexible enough to allow

HSQ to be highly crosslinked at temperatures as low as ambient, while still being able to easily remove them from the rigid films by using a single heating step to form pores. Owing to the complete miscibility of the co-solvents, this technique potentially allows wide ranges of porosities to be produced; hence, enabling the properties of the porous films to be varied with co-solvent composition. The dual use of the co-solvents as both crosslinking agents and as placeholders for air pockets decreased the processing complexity relative to other solvent-processing techniques, since the need for a separate crosslinking catalyst was eliminated. Additionally, this technique had all of the processing advantages of other solvent-processing methods for porous films, such as relatively short processing times (about 50 minutes), and low processing temperatures (120-150^{o}C). In contrast, porosity methods that use thermal decomposition of sacrificial polymers usually require processing times of at least 2 hours and temperatures well above 250^{o}C in order to decompose the porogen.[5, 6, 14, 16-19]

CHAPTER 2: BACKGROUND

2.1 Methods of Inducing Porosity in Thin Films

A variety of methods have been reported in literature for producing porosity in thin films. These methods can be broadly categorized under two main categories, namely those that employ sacrificial polymers to serve as templates for pores after their decomposition and those that use solvents to generate the pores. These processing methods are summarized in the following subsections of this thesis.

2.1.1 Thermal Decomposition of Templated Sacrificial Polymers

The traditional template technique for fabricating a porous thin film makes use of a porogen (thermally decomposable polymer or volatile solvent) distributed in a crosslinkable matrix.[5, 6, 14-16, 18, 19] During processing, the matrix is cured to instill mechanical integrity, before the film is heated to high temperatures to decompose and volatilize the templated polymer. As the decomposition by-products diffuse out of the films, air diffuses in to replace the porogen, resulting in the formation of air pockets in-place of the sacrificial polymer chains. The total processing time for the template technique may be several hours because of the necessity of thermally setting the matrix as well as decomposing the polymer via a slow ramp in temperature to the decomposition point of the porogen and a dwell time to ensure the removal of all of the porogen.[5, 6] Additionally, films must be allowed to cool slowly prior to removal from furnaces otherwise there will be formation of cracks due to internal stress, which arises from thermal shock of exposing the very hot films to ambient conditions. An additional

disadvantage of thermally decomposing a porogen to produce porosity is that many organic materials cannot be used as substrates owing to their degradation at the high temperatures required to decompose the templated polymers. Finally, the high temperatures required to thermally decompose polymers encourage phase segregation and agglomeration of the macromolecules prior to decomposition thus producing large, non-uniformly dispersed pores that may produce undesirable final properties in the porous films.[20-29] To avoid phase-segregation during thermal processing, sacrificial polymers chains must be chemically bonded to the matrix backbone to prevents their movement at high temperatures.[5, 6, 14, 16-19]

2.1.2 Radiation-Induced Decomposition of Photodefinable Sacrificial Polymers

There exist certain classes of sacrificial polymers that are susceptible to either direct or indirect decomposition via photolytic reactions. The polymers that are discussed in the following subsections are polysilanes, which are directly decomposable via radiation, and polycarbonates, which may be decomposed via the use of photogenerated acids. In accordance with terminology used in literature, the photocleavage reactions that lead to the decomposition of polysilanes are referred to as photobleaching. [20-29]

2.1.2.1 Photobleaching Method via Photocleavable Polysilanes

Researchers have made use of the photocleavable nature of Si-Si bonds in the structure of polysilanes to UV-induce porosity in hybrid films composed of methacrylate-polysilane copolymers (MPS) chemically bonded to inorganic sol-gel matrix materials.[22]

Miura et al. reported that when an MPS-titania film with 50 wt% MPS was exposed for 10 seconds to 248 nm UV radiation having an intensity of 105 mW cm^{-2}, the refractive index of the film dropped by 0.18 while a MPS-silica film with 50 wt% MPS had a refractive index drop of 0.16.[22] These decreases in refractive indices were due to the incorporation of air within the matrix materials since air has a refractive index of only 1.0003.[1] While investigating the use of poly(methyl phenylsilane) (PMPS) films in the formation of phase masks, Nagayama et al. reported that 0.3 μm PMPS films exposed to 308 nm light had a refractive index drop from 1.70 to 1.63 while films exposed to 254 nm light showed a drop in refractive index from 1.70 to 1.58 due to photodecomposition of the PMPS.[23] Mimura et al. reported that when a MPS-silica (24wt% MPS) hybrid film was exposed to UV radiation, the refractive index of the film dropped from 1.60 to 1.53 before rinsing with hexane, and dropped further to 1.40 after the hexane rinse leading them to conclude that all of the polysilane had decomposed.[21]

2.1.2.2 Direct-Write Porosity via Photodefinable Polycarbonates

The polysilane-based photobleaching system described above relies on the direct photosensitivity of polysilane and will only work for polymers that can be directly decomposed by radiation. As opposed to polysilanes, polycarbonates, although not directly photocleavable, may be indirectly decomposed via UV radiation due to their vulnerability to acidolysis.[30, 31] By mixing bulk polycarbonate films with photoinitiators that release acids upon irradiation ie. photoacid generators (PAGs), the polymers molecules may be selectively decomposed via photogeneration of acids under a photomask thus enabling their use as positive-tone resists materials.[32-41] The mechanisms

for the acid-catalyzed de-polymerization of both aromatic and aliphatic polycarbonates have been presented by Frechet et al.[30] and Jayachandran et al.[31] The direct-write process presented here relies on the PAG/polycarbonate chemistry but instead of only dispersing PAG molecules in a bulk polycarbonate film, both PAG and polycarbonate molecules are templated within a crosslinkable SOG matrix. Prior to acid-induced decomposition of the polycarbonate chains, the matrix is hardened to allow it to mechanically support porosity. UV-exposure and a post-exposure bake (PEB) are used to drive the acidolysis of the sacrificial polymer, resulting in the production of porosity and the lowering of the refractive index. By performing irradiation through a photomask, one may laterally pattern porous regions (cladding) and non-porous regions (cores) to create refractive index profiles within the processed film. To prevent acid-catalyzed decomposition of the polycarbonate molecules in non-porous regions, a blanket UV-irradiation is used to generate acids before their neutralization via the diffusion of a basic gas through the film. As an alternative to using a basic gas to neutralize the acid molecules, a vacuum environment or a high purge flowrate may be used to sweep away volatile acid molecules after their photogeneration.

2.1.3 Solvent Leaching and Particle Dissolution

Another method by which solvents have been used to generate porosity is via dissolution of soluble particles or co-polymer segments dispersed within films. This method if called a subtractive method due to the removal of the pore-generator via dissolution by solvents.[3] In this processing method, coated films are leached with appropriate solvents that are able to swell an insoluble matrix and also dissolve the

dispersed sacrificial solid material. Following this leach and dissolution step, the solvents and the dissolved particles) are removed, and the films are then dried to produce pores in place of the particles.[3, 42, 43] Polymers are used as the insoluble host matrix materials since a large number of polymer films are easily penetrated solvents and can be chemically bonded with soluble co-polymer segments or sacrificial particles to ensure that the resultant pore structure is homogenous. The pore sizes are highly dependent on the sizes of the sacrificial solids that are originally dispersed within the matrix. The sacrificial co-polymer segments and colloidal particles that have been reported to be used are fairly large, producing pores ranging in size from several hundred nanometers to hundreds of micrometers. [3, 42, 43] Given the large sizes of the pores and the tendency of porous polymeric films to quickly absorb atmospheric moisture due to the high permeability of water in polymers compared to inorganic glasses, these leaching methods have not been adopted by the IC industry for producing porous dielectrics.[3, 14, 16, 44, 45]

2.1.4 Porosity Induced via Volatilization of Encapsulated Solvent

As stated earlier, an alternative method for producing porous films is to volatilize encapsulated solvents from rigid films. Although a wide selection of solvents are available that can be mixed into spinnable formulation and later boiled off from matrix materials, solvents are carefully selected to ensure that it has physiochemical compatibility with the host matrix used (i.e. the solvent must not dissolve or otherwise degrade the bulk material that is meant to host the pores nor volatilize before the matrix has been fully vitrified). The methods of crosslinking the films prior to solvent removal depend on the nature of the matrix material. Many organic materials (i.e. polymers) can

be thermally cured at moderate temperatures, where some high boiling point solvents will not prematurely be removed.[45] Alternatively, polymers may be crosslinked at low temperature via radical-, cationic-, or anionic-catalysis.[3, 45-48] Researchers have produced solvent-induced porosity in poly(aryl ethers) via a process of phase separation and evaporation.[49] The pores produced were about 3 nm in size but the processing times were long because of the extensive mixing times required (over 24 hours) to ensure that the degree of phase segregation was sufficient prior to spin-coating.

Spinnable inorganic materials are sol-gel based, and their thermal cure reactions take place at such high temperatures that few solvent molecules would remain trapped within a thermally cured matrix. To overcome this constraint, the their crosslinking reactions of sol-gel films are catalyzed at low temperatures via the use of acids or bases to induce silanol condensation in order to allow all of the solvent molecules to be encapsulated and ensure high induced porosities when they are removed. A multitude of inorganic materials have been successfully incorporated with solvent-induced pores, such as silica (aeorgels, xerogels) and silsesquioxane-based matrices (e.g. XLK, which is Dow Corning's porous version of HSQ).[3, 4, 8, 10, 50-53] Porous silica films are produced by spin-coating resins of silica-precursors, such as tetra-ethoxy silane (TEOS), and then crosslinking them via exposure of to bases under tightly controlled conditions (pH, temperature, water content, alcohol content, etc) prior to removal of entrapped solvents.[52-55] Aerogels have porosities as high as 98%, but require supercritical conditions to generate these levels of porosity, while xerogels can be produced at moderate volatilization temperatures but their porosities are much lower (50-90%).[52, 53] Although aerogels and xerogels have high porosities, their pore structure has low

reproducibility, since there are many physical and chemical factors that affect the rate of gelation and thus the degree of film shrinkage prior to pore formation.[52-55]

The solvent-processing of porous silsesquioxane SOGs is less tedious, because sol-gel based SOGs are easily gelled after spin-coating via the use of catalysts. They are then baked at moderate to high temperatures to produce levels of porosity comparable to xerogels.[4, 8, 10, 50, 51] For instance, during the processing of XLK, films are spin-coated from a resin that already contains the porogen, and then these films are crosslinked using aqueous ammonia for 30-60 seconds at ambient temperature.[4, 10, 12] The ammonia soak step is used to initiate base-catalyzed gelation, which makes the matrix rigid enough to support porosity. Finally, the films are baked on a 150^{o}C hotplate for 1 minute and subsequently in a 450^{o}C furnace for an hour to completely volatilize solvents trapped within the rigid film structure.[3, 4, 7, 8, 10, 12, 50] XLK films have high levels of porosity (> 50%), very low dielectric constants (1.5 - 2.2), and small pores (< 4 nm), making them very attractive dielectric materials.[56]

2.2 Applications

2.2.1 Dielectrics

As the dimensions of complimentary metal-oxide-semiconductor (CMOS) transistors in integrated circuits (ICs) have continued to shrink to obtain higher performance, the gate switching time has been surpassed by the signal propagation time as the timescale limiting the overall speed of micro-processors.[56] This is because although the transistor switching time has scaled down with the decreasing feature sizes, the global and semi-global RC delay time has *increased* as the dimensions of electrical

interconnects have decreased.[3, 44, 56] Thus, further reductions in transistor dimensions alone do not guarantee reductions in micro-processing times, since switching times are no longer the dominate timescale that dictates the overall delay time of ICs. To ensure that that the RC delay remains low, the traditional dielectric (SiO_2) must be replaced by alternative materials that have lower dielectric constants at frequencies used in integrated circuits.[44]

2.2.1.1 Low-k and Ultra Low-k Materials

Low-k materials, which are defined as materials with dielectric constants below 4, exhibit lower polarizabilities than SiO_2 when subjected to electrical fields as driving forces.[3, 44, 45] The substitution of low-k films in place of SiO_2 as intralevel dielectric materials leads to a decrease in the capacitance compared to SiO_2 layers, thus decreasing the RC delay.[3, 44, 56] However, the IC industry has placed stringent requirements for low-k materials to be considered compatible with IC processing, namely the low-k materials should have low dielectric constants, allow low leakage currents, have high breakdown voltages, have good mechanical properties, have good adhesion properties, be able to withstand the high temperatures that ICs are commonly subjected to, and be resistant to the chemicals used in wet-processing of ICs.[9, 45, 51, 57-73] Over several years, a multitude of low-k materials have been investigated, including silsesquioxanes, xerogels, polymers, and PECVD films to determine if the final material properties and the processing conditions are compatible with standard CMOS processing.[44, 45, 57, 59, 60, 63-65]

One of the low-k materials that has been shown to satisfy many of the criteria is HSQ, and its properties have been widely reported in literature.[57, 58, 63, 64] HSQ is a purely

inorganic SOG with the general formula $HSiO_{1.5}$, and it is spin-coated prior to being thermally cured in a 350-400^{o}C nitrogen-purged furnace at high temperatures to form rigid SiO2-like structure.[57, 63, 65] The thermal cure reactions of HSQ occur over a wide range of temperatures (200-800^{o}C), and the final dielectric and optical properties of HSQ films depend on the cure temperature used.[59, 60] At optimal processing conditions for low-k applications, HSQ has a dielectric constant of 2.7, which is stable at ambient humidity for extended periods of storage.[3, 74, 75] A major disadvantage of using HSQ as a low-k film is it has poor resistance to chemical attack, and it degrades easily when exposed to polar liquids, plasma conditions, and ashing conditions.[51, 62] In the presence of bases, the hydrophobic silane bonds in HSQ films undergo hydrolysis resulting in their conversion to hydrophilic silanol bonds, leading to moisture uptake and increases in their dielectric constant. Since aqueous bases, such as tetra-methyl ammonium hydroxide (TMAH), are frequently used as developers during photolithography, exposure of films to polar media cannot be avoided during IC processing. To avoid film degradation, the surfaces of HSQ films are modified by either making their surfaces more hydrophobic (e.g. converting the silane bonds on the surface to Si-CH_3) or by capping them with diffusion barriers.[4, 7, 8, 10, 12, 50, 76, 77] Inorganic-organic hybrid SOGs, such as methyl silsesquioxane (MSQ) have excellent chemical resistance due to their hydrophobicity, which affords them the ability to maintain low-k properties even when exposed to polar media.[78] For this reason, organo-silicon SOGs are among the most popular types of materials for low-k films.[3, 5, 6, 18, 19, 58, 62, 79]

Since porosity is known to decrease the polarizability of a material, several porous films have been investigated as potential ultra low-k materials (dielectric

constants < 2.0). Among the potential ultra low-k materials, porous SOGs, such as XLK and porous MSQ, have been widely reported. XLK is a porous version of HSQ and its pores are induced by the volatilization of entrapped solvent, as described in a previous section. Depending on the processing conditions used, XLK can have a dielectric constant as low as 1.5, induced- porosities as high as 60%, pore sizes ranging from 2-4 nm, fair mechanical integrity and fairly stable dielectric properties even when left uncapped at ambient conditions.[3, 10, 51, 62, 80] However, as with non-porous HSQ, XLK films must either be capped with barrier layers or have its surface sites chemically modified to avoid degradation of their ultra low-k qualities upon exposure to reactive environments.[5, 6, 18, 19, 49, 58, 79, 81]

Porous MSQ films, formed via the decomposition of templated sacrificial polymers, have been shown to possess tunable dielectric constants as low as 2.2, pore sizes comparable to XLK films, and superior chemical resistance properties.[3, 5, 6, 8, 18, 19, 50, 58, 62, 77, 79] Because of their overall qualities, porous MSQ films have attracted a great deal of interest from the IC industry and it remains one of the leading candidates for selection for use as a suitable ultra low-k material.[3] Although the porous films presented in this thesis are all based on the HSQ host matrix, their processing methods and their final film properties are unique from those of XLK films.

2.2.2 Waveguides

As the demand in the IC industry for higher bandwidth and higher data transmission rates of interconnects continues to increase, so has the investment into the development of integrated optoelectronic systems as long-term substitutes for present day

CMOS circuitry. Optoelectronic systems can have higher interconnect and gate packing densities than purely electronic systems, since optical signals do not interfere with each other when they have different wavelengths. Thus, optical interconnects may transmit multiple signals of different wavelengths without interference. Additionally, optoelectronic systems are less vulnerable than electrical systems to electromagnetic interference (EMI) and have lower power and heat dissipation. Currently the largest market for optoelectronics in the IC industry is in the manufacture of backplanes.[45, 82-92] Widespread research is currently being performed to fabricate on-board and on-chip integrated waveguides designs due to the numerous benefits that optoelectronics provides.[82, 93, 94]

2.2.2.1 Slab Waveguide Theory

According to the theory of refraction, when light travels from a medium of higher refractive index (n_H) to one of lower refractive index (n_L), its path in the second medium is bent away from the normal due to refraction. Thus, the angle between the incident light rays and the normal, called the angle of incidence (θ_i), is lower than the angle between the transmitted light and the normal, called the angle of refraction (θ_t). There exists an angle of incidence, called the critical angle (θ_c), at which light is no longer transmitted into the second medium but is instead refracted along the boundary between the two media, i.e. the angle of refraction is 90^o. Thus the critical angle represents the largest angle at which refraction takes place and is calculated by using equation (2.1).

$$\theta_c = \sin^{-1}\sqrt{\left(\frac{n_H}{n_L}\right)} \tag{2.1}$$

When the angle of incidence is above the critical angle ($\theta_i > \theta_c$), light is no longer refracted nor transmitted into the second medium, rather, it is totally internally reflected (TIR) from the interface between the media so that light remains within the first medium. Optical fibers and waveguides operate on the basis of confinement of light in a region of higher refractive index (cores) via TIR, by surrounding the cores with regions of lower refractive indices (cladding areas), and ensuring that the angles of incidence at the core/cladding boundaries are above the critical angle. However, TIR is not the only requirement for light to be guided within optical fibers and waveguides.[82, 93, 94]

As light propagates in a waveguide core, it undergoes phase changes due to interactions within the guiding layer and its upper and lower interfaces such that the total phase change is 2π during one zigzag path.[82, 93, 94] This phase rule, commonly referred to as mode matching, must be satisfied in order for electromagnetic fields (modes) to be supported as light propagates along the waveguide core. Equation (2.2) shows the characteristic equation for slab waveguides for mode propagation of TE-polarized light.[93, 94] As shown in equation (2.2), for fixed values of wavelength of light, and refractive indices of core and cladding areas, only discrete values of film (core) thickness, h and zigzag angles will support the propagation of any given mode.

$$\frac{2\pi\, n_f h\cos\theta}{\lambda} - \tan^{-1}\left(\frac{\sqrt{n_f^{\,2}\sin^2\theta - n_s^{\,2}}}{n_f\cos\theta}\right) - \tan^{-1}\left(\frac{\sqrt{n_f^{\,2}\sin^2\theta - n_c^{\,2}}}{n_f\cos\theta}\right) = \nu\pi, \qquad (2.2)$$

$$\nu = 0, 1, 2, \ldots$$

The symbols n_f, n_c, and n_s refer to the refractive indices of the core, the layer directly above guiding layer (cover), and the layer directly below guiding layer

(substrate), respectively. θ, ν, and h, refer to the zigzag angle, mode number, and thickness of the guiding layer, respectively.

2.2.2.2 Waveguide Materials

Since light confinement in waveguides occurs due to total internal reflection, large differences between the refractive indices of cores and cladding regions are desirable since this affords better confinement of light within the waveguide core.[93, 94] Waveguides may either be made of composite materials which have different intrinsic refractive indices in combination with surface-relief geometry or their optical differences may be due to internal structural differences, such as in direct-written waveguides. Ideally, a potential waveguide material needs to have the following properties to be a good candidate for optoelectronic use:

- Uniform optical properties [44, 45, 82]
- Negligible intrinsic losses due to absorption (i.e. have high transparency at the wavelengths of the propagating light) [95-97]
- Negligible Rayleigh scattering effects: by having a very low amount of scattering centers (eg. particulates or pores) and/or by having scattering centers with domain sizes much smaller than the wavelength (e.g. << 10 nm for optical wavelengths) [85, 87, 88, 98-100]
- Its surfaces should be very smooth so as to avoid producing large extrinsic losses due to light scattering from surface roughness [44]

- Its material properties should make it resistant to physiochemical degradation during processing (e.g. chemical resistance to typical solvents used during processing) [44]
- Good adhesion to other common waveguide materials [44, 45, 82, 83]

Polymeric materials have many of the properties outlined above, making them attractive for use in waveguides.[1, 44, 45, 82] Although polymers typically have higher absorption properties than silica-based materials, they are flexible, require lower processing temperatures, and multiple polymer coating methods exist that are compatible with mass production of waveguides (e.g. lamination into sheets).[45, 82] Additionally, polymers may be coated into thick layers without cracking, making them attractive materials for multimode waveguide applications.[91, 92, 101, 102]

The use of sol-gel materials to fabricate optical devices has been studied by numerous researchers due to the ability to incorporate dopants or porogens into the films and thus have tunable optical properties while still retaining low attenuation losses (<0.2 dB/cm) of silica-like films.[91] Traditionally, sol-gel films have been limited to thicknesses under 1.5 μm due to the propensity of thicker films to crack due to the internal mechanical stress that developing during heating cycles. Thus, lower cladding layers based on SOG technology would be limited in thickness, and the radiation loss of the waveguide due to substrate interaction with the evanescent wave may be significant. In such a case, the signal loss of a thin film waveguide per unit distance would be large and there would be little incentive for optoelectronic researchers to pursue the use of an SOG with cracking-tendencies as a matrix material in a waveguide system. However, Yeatman and Dawnay showed that by performing rapid thermal annealing steps between

multiple sub-micron coats of sol-gel films the internal stress within the films can be relieved allowing crack-free films to be formed which have thickness on the order of tens of micrometers.[91] This allows sol-gels films to be made thick enough to isolate waveguide modes from absorptive substrates, thus reducing losses due to undesired substrate interactions negligible.

It has been shown in literature that porosity increases the maximum crack-free thickness of SOGs due to the ability of elastic pores to reduce internal stresses within the SOG matrix. For example, non-porous HSQ has a maximum crack-free thickness of about 1.2 μm, and the porous version (XLK®) has a crack-free thicknesses above 2 μm.[21-23, 27, 83, 103] Since porosity is known to decrease the refractive index of solids, porous films potential can serve as novel cladding materials for optical waveguides.[83, 97] Porosity can be incorporated in a variety of organic and inorganic host matrix materials, but materials selection is critical to avoid any incompatibility with either the processing conditions or the final optical properties of the final waveguides. Since optics is not a commonly associated with application for porous films, very little research has been performed to evaluate the applicability of porous films in optical waveguides.[45, 82, 84] The successful fabrication and characterization of porous direct-written waveguides would represent a new area of research in direct-write waveguide processing.

2.2.2.3 Methods of Processing Waveguides

Lithography, reactive ion etching (RIE), laser patterning, and hot-embossing are the most common methods of forming core/cladding waveguide patterns.[45, 83, 89] These methods are used to create surface relief profiles that allow light to be confined within the

patterned waveguide channels. However, these procedure require complicated and time-consuming processing sequences such as multiple lithography steps and curing cycles in order to produce the required geometry of the waveguides.[83]

Direct-write processing of waveguides is less tedious since the cores and side-cladding regions are photodefined upon UV-exposure of the direct-write layer under a photomask.[45] UV-radiation produces differences in optical properties arising from internal structural changes; hence, surface-relief profiles are not needed to confine light within the direct-written waveguide cores. Thus direct-write processing reduces both the complexity and overall time required for producing waveguides. Conventionally, direct-write waveguides are formed via photo-induced changes in refractive index whereby ultraviolet radiation is used to induce cross-linking of photosensitive materials thus increasing the refractive index of exposed regions due to the increase in density.[20, 25, 26, 104] The UV-patterning of silicon dioxide channels via the photooxidation of polysilane and polysilyne precursors has been reported. [57, 58, 60, 64] When polysilanes are exposed to UV radiation and heat treated, the photosensitive Si-Si bonds photocleave to produce radicals, which react with oxygen molecules to produce siloxane bonds.[57, 58, 60, 64]

CHAPTER 3: EXPERIMENTAL METHODS

3.1 Materials

The spin-on glass (SOG) matrix material used in this study was a resin of hydrogen silsesquioxane (HSQ) dissolved in methyl isobutyl ketone (MIBK) solvent and sold under the tradename FOx® by Dow Corning Corp. HSQ has a distribution of structures ranging from the simple cage structure to the highly complex, 3D networked structure. As HSQ films are cured, the internal bonds break and rearrange themselves into predominantly networked structures, as discussed in literature.[40, 41, 48, 105-109] The sacrificial polymer used was poly(norbornene carbonate) or PNC. The macromolecular structure of PNC, **1**, is shown in Figure 3.1.

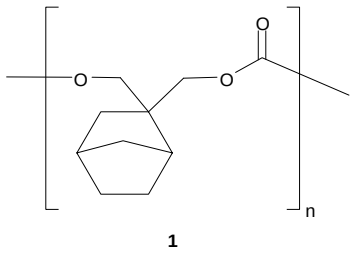

1

Figure 3.1 – Chemical structure of PNC repeating units.

Photobase generators (PBGs) refer to photoinitiators that release bases when activated by radiation.[40, 41, 46-48, 105, 107-117] The photobase generators (PBGs) used in this study were N-cyclohexl-*p*-toluene sulfonamide (CTS), *o*-nitrobenzyl cyclohexylcarbamate (NBC), and N-methylnifedipine with their respective structures (**2**, **3**, and **4**), shown in Figure 3.2. CTS and NBC were commercially obtained from

Lancaster Synthesis and Midori Kagaku respectively. Since N-methylnifedipine was not commercially available, it was synthesized and purified according to the method reported in literature and its structure, **4**, was verified by ^{1}H-NMR analysis.[63]

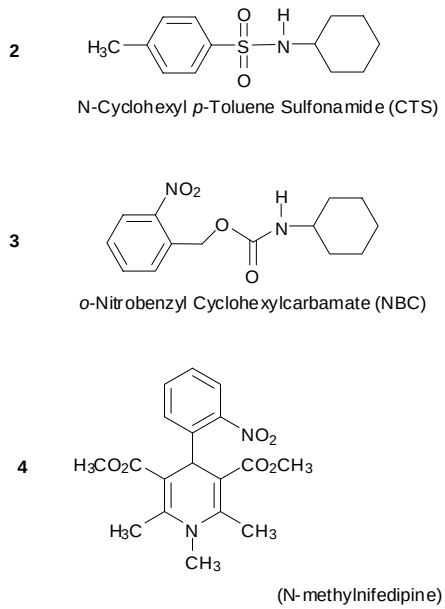

Figure 3.2 – Chemical structures of PBGs.

The photoacid generators (PAG) used in this study were Rhodorsil 2074, tris(tert-butyl phenyl)sulfonium triflate [TTBPS-Tf], and tris(tert-butyl phenyl)sulfonium nonaflate [TTBPS-Nf], with their respective structures (**5, 6,** and **7**), shown in Figure 3.3. Rhodorsil 2074, TTBPS-Tf, and TTBPS-Nf were purchased from Rhodia, Sigma-Aldrich and Midori-Kagaku, respectively. HPLC grade MIBK solvent was obtained from Sigma-Aldrich and used without further purification.

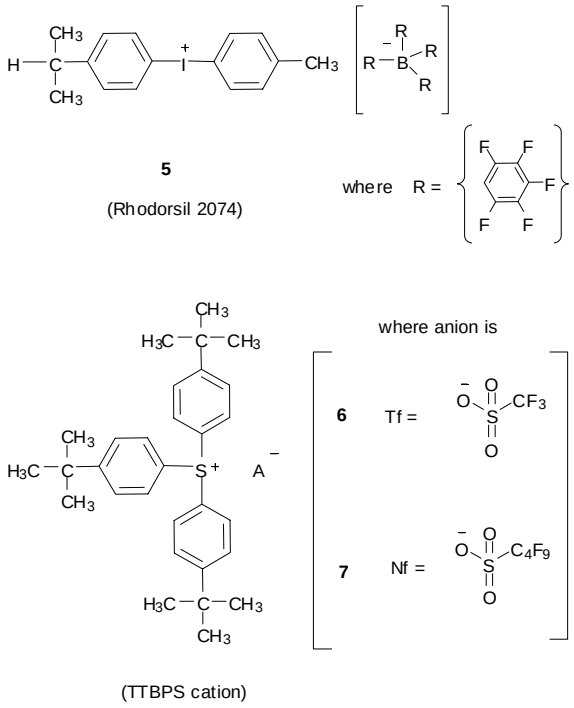

Figure 3.3 – Chemical structures of ionic PAGs

3.2 Thermogravimmetric Analyses (TGAs)

Thermogravimmetric analyses (TGAs) were used to obtain decomposition profiles of the neat sacrificial polymer as well as polymer-PAG mixtures. To make polymer-PAG mixtures, separate solutions of PNC and each PAG were made using MIBK solvent. Then these PNC and PAG solutions were mixed such that the solids content of dry PAG with respect to dry PNC solids was 3 wt%. The PAG/PNC mixtures were pipetted onto aluminum dishes and dried at about 110^{o}C for 1-2 hours in a vacuum oven prior to each TGA run in order to avoid the influence of solvent volatilization on the TGA results. Non-isothermal TGAs were performed by recording tared sample weight as the TGA oven was heated at 3^{o}C min^{-1} from ambient to about 325^{o}C and held at 325^{o}C for 90 minutes to completely decompose PNC. Isothermal TGAs were performed by

recording tared sample weights only after ramping the TGA at 20°C min^{-1} to the desired dwell temperature before tracking the weight of the sample against time. All TGA runs were performed with nitrogen purge flowrates lower than 30 cm^3 min^{-1} to avoid the effect of photoacid volatilization on the rate of acid-catalyzed PNC decomposition. Differential scanning calorimetry (DSC) was used to determine the glass transition temperature of HSQ according to the method reported by Siew et al.[118-120] Both TGA and DSC studies were performed using a Sieko TG/DTA 320.

3.4 Gelation Studies

3.4.1 Liquid-Phase Gelation of HSQ (FOx-1x® Resin)

Experiments were conducted to investigate the susceptibility of HSQ to gelation both in the liquid-phase and in the solid-phase. For liquid-phase experiments, FOx-1x® resin was mixed with an equal volume of a polar organic solvent in sealed high density polyethylene (HDPE) vials at room temperature. To ensure fair comparisons between the influences of each of the solvents, the solvents were chosen to ensure that they were all hydrophilic, capable of hydrogen bonding with the silane bonds in HSQ, and completely miscible with the resin's MIBK solvent, thus avoiding complications arising from differences related to phase equilibria.[121, 122] In all cases, a single liquid phase was observed after the contents of the vial were swirled for a few seconds to ensure good mixing. Similar to techniques reported in literature, the gelation time was defined as the time taken for a mixture to completely solidify, such that when a vial was overturned, the gelled mixture remained fixed to the bottom of the vial due to its rigidity.[58, 60, 64, 65] The fluidity contents of the vials were checked continuously for the first hour then

observations were made every half hour until 5 hours had passed. For formulations with gelation times longer than five hours, observations were made on an hourly basis from the fifth until the twelfth hour, and then every twelve hours after the twelfth hour. The experiments were then repeated to check for consistency of the recorded gelation times. The liquid-phase gelation results are listed in section 5.1 of this thesis.

3.4.2 Solid-Phase Gelation of HSQ Films

Three types of solid-phase gelation experiments were performed. For the first type of gelation experiment, a tin filled with a 26 mol% aqueous ammonia solution was placed underneath an overturned dish and the closed vapor-liquid system was allowed to come into equilibrium. Then spin-coated HSQ films of 0.7-1.2 μm thickness were placed under the overturned dish to expose them to ammonia vapor so as to catalyze the hydrolysis of HSQ. The ammonia treatments were performed at ambient temperature for various times ranging from 1-45 minutes. To determine the overall influence of temperature gelation via the ammonia treatment, the ammonia system was placed in preheated ovens (50^{o}C, and 100^{o}C) and equilibrated before inserting HSQ films for similar amounts of time to the ambient gelation experiments. The results of the first two types of sold-phase gelation experiments are discussed in section 4.2 of this thesis.

The second type of solid-phase gelation involved the use of photogenerated bases to catalyze the crosslinking of HSQ. Solutions of each of the PBGs shown in Figure 3.2 were made in MIBK solvent and then mixed with FOx-1x® to form PBG-HSQ mixtures with PBG loadings of 1-13 wt% with respect to dry HSQ. The PBG-HSQ solutions were then spin-coated onto silicon wafers and then exposed to ultraviolet radiation followed by

a PEB for 30 minutes at temperatures above 120^{o}C in order to release bases and catalyze the crosslinking of the HSQ films.

For the third type of gelation experiment, non-protic polar organic solvents were used to initiate the crosslinking spun-coated HSQ films, either in the form of pure solvents or as polar co-solvent mixtures. In both cases, spun-coated HSQ films of 0.7-1.2 μm thickness were immersed in polar organic solvents for soak times ranging from 20 minutes. To determine the overall influence of temperature on solvent-induced gelation, the dishes containing the polar solvents were first placed in preheated ovens at temperatures ranging from ambient to 150^{o}C and equilibrated prior to inserting HSQ films. After completion of a soak step, the surface of the dipped film was dried using a nitrogen spray gun prior to any characterization of its material properties. The results of the third type of sold-phase gelation experiments are discussed in section 5.2 of this thesis.

HSQ films gelled by all three catalysts (ammonia gas, photogenerated bases, and polar organic solvents) were characterized by fourier transform infrared spectroscopy (FTIR) in attenuated total reflectance (ATR) mode and also by nanoindentation analyses as described in the following subsections.

3.4.3 FTIR Studies

FTIR was used to determine the bond transformations, and thus the chemical interactions that occurred during the gelation of HSQ films. A Thermo-Nicolet 520 spectrophotometer was used to perform FTIR studies on spun-coated HSQ films of 0.7-1.2 μm thickness using ATR mode. Literature sources were used to identify the FTIR

stretch peaks corresponding to HSQ's silane, cage-type siloxane, and network-type siloxane bonds. These peaks were centered at (2250 cm^{-1}), (1130 cm^{-1}) and (1070 cm^{-1}), respectively.[57, 58, 64] In accordance with methods used in literature, the extent of gelation of HSQ was tracked by recording the ratio of the area underneath the FTIR peak corresponding to cage-type to that underneath the network-type siloxane stretch peak. [57, 58, 64] This ratio is referred to as the c/n ratio when discussed later in the thesis (sections 4.2, 5.1, and 5.2).

3.4.4 Nanoindentation Analysis

After FITR analyses were performed, a Hysitron Triboindenter® was used to nanoindent each of the gelled HSQ films in order to quantify the mechanical rigidity induced by gelation. During nanoindentation, each of the films was probed multiple times using a Berkovich tip according to the method outlined by Oliver and Pharr.[123] After nanoindentation the reduced moduli, E_r, of the gelled films were compared with their c/n ratio (obtained from FTIR data) so as to correlate the chemical interactions of gelled films with changes in their mechanical properties. The nanoindentation results of gelled films are discussed in sections 4.2, 4.7, 5.1, and 5.2.

3.5 Processing of Porous Films

The porous films used in this study were formed either using the sacrificial polymers or solvents as the pore generators after first hardening the HSQ matrix enough to mechanically support porosity. As outlined in the following subsections, sacrificial polymer chains were decomposed either via thermolysis or acid-catalyzed decomposition

to generate air pockets, while for solvent-induced porous films, volatilization of entrapped was used to generate the pores.

3.5.1 Thermally-Induced Porosity: Traditional Template Technique

For porous films formed via the traditional template technique, a dilute solution of PNC in MIBK solvent was mixed with FOx-1x® resin to make mixtures with the mass ratios of PNC to dry HSQ ranging from 1:10 to 3:10. These solutions were spin-coated onto silicon wafers and then the films were heated in a nitrogen-purged Lindbergh furnace at $3^{o}C\ min^{-1}$ from $270^{o}C$ to $325^{o}C$ and held at $325^{o}C$ for 90 minutes to completely decompose PNC. The properties of these thermally processed porous films were compared to pure HSQ control films that underwent the same heating procedure to elucidate the effect of induced porosity on the average properties of the matrix.

3.5.2 UV-induced Porosity: Direct-Write layer

3.5.2.1 A-type and B-type Direct-Write Formulations

Prior to mixing direct-write formulations, separate dilute solutions were made for the following substances in MIBK solvent: CTS, N-methylnifedipine, TTBPS-Tf, and PNC. FOx-1x® resin was used as supplied from Dow Corning. Although both CTS and N-methylnifedipine PBGs were thermally unstable, their absorbance spectra were very different (CTS was highly absorptive at wavelengths <300 nm and N-methylnifedipine was highly absorptive up to 400 nm). Owing to the different properties of the PBGs, two separate types of direct-write formulations were made, named A and B.

For A-type formulations, the separate solutions of CTS, TTBPS-Tf, PNC, and FOx-1x® resin were mixed to produce the following mass ratios with respect to dry solids: wt PBG to wt PAG to wt PNC to wt HSQ = 1:2:2:20. For B-type formulations, the separate solutions of N-methylnifedipine, TTBPS-Tf, PNC, and FOx-1x® resin were mixed to produce the following mass ratios with respect to dry solids: wt PBG to wt PAG to wt PNC to wt HSQ = 1:5:10:50 and 1:10:20:100. Both types of direct-write solutions were passed through 0.2 μm PTFE membrane filters prior to spin-coating onto silicon wafers to avoid film non-uniformities arising from the presence of particulates.

3.5.2.2 Direct-Write Processing

The basic sequence for the direct-write process is shown in Figure 3.4. The first step involved the dispensing of a direct-write formulation onto silicon wafer. The spin-coated film was then cured or hardened below the thermal activation temperature of the PAG to avoid decomposing the sacrificial polymer throughout the film. The low-temperature curing occurred via base-catalyzed gelation of the SOG matrix where the bases used were either ammonia gas or photogenerated bases released from activated photobase generator (PBG) species incorporated in the formulation of the dispensed solution.

To crosslink A-type films, the samples were placed in a Lindbergh furnace already at 160-170^{o}C and baked for 30 minutes in stagnant air. The baking activated the CTS PBG molecules resulting in the release of cyclohexylamine, which catalyzed the gelation of HSQ.[3] Since N-methylnifedipine could be activated either thermally or by UV-exposure >300 nm, B-type films were crosslinked either by a similar bake procedure

to A-type films or exposed to 1 J cm^{-2} of 365 nm UV underneath a filter to prevent DUV from reaching the samples and prematurely activating the TTBPS-Tf PAG followed by a PEB above 120°C in a Lindbergh furnace in stagnant air.

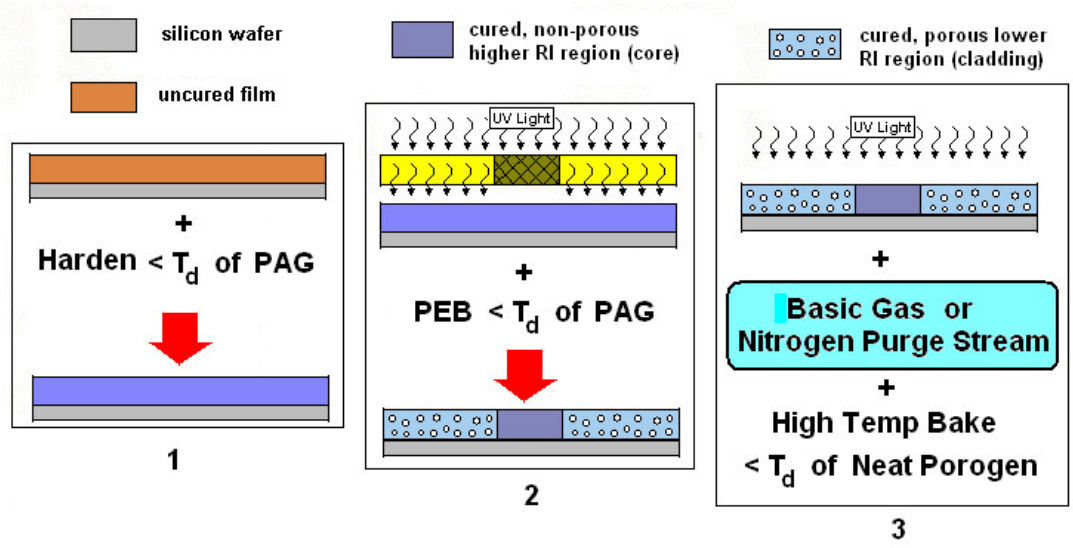

Figure 3.4 – Basic sequence for lateral patterning of direct-write porosity. T_d refers to the temperature at which thermal degradation begins.

After the crosslinking step shown in Figure 3.4, the films were exposed to DUV radiation and post-exposure baked (PEB) to activate the PAG and release acid in irradiated regions and hence selectively decompose the sacrificial polymer.[30, 31] The minimum dose of DUV radiation used to fully activate the PAG was 3.8 J cm^{-2}, and the PEB was performed in a preheated Lindbergh furnace at 160-170°C (stagnant air atmosphere) for at least 20 minutes.

To prevent PNC decomposition in unexposed regions and thus maintain the refractive index profile, films were blanket exposed with DUV radiation to activate remaining PAG, followed by either volatilization of acid molecules at high temperature

or immediate treatment with a basic gas (ammonia gas) to neutralize the photogenerated acids at ambient temperature. Finally, the films were heated to about 250^{o}C for 30 minutes while purging the tube furnace with 2 L/min flowrate of nitrogen in order to drive off any polar species and condense residual silanol groups within the SOG matrix, since both would degrade the low-k and optical properties of the film by encouraging moisture uptake. Direct-write control films (HSQPBGPAG), which had the same HSQ, PBG, and PAG loadings as direct-write formulations without any PNC content were processed in a similar manner to direct-written films to determine the effect of porosity on the average properties of the direct-written matrix. The dielectric and optical properties of direct-write films and their respective control samples are shown in sections 4.4 and 4.5 of this thesis.

UV-patterned films were processed in a similar manner to blanket irradiated films except a quartz photomask containing opaque line patterns was used during the DUV exposure to define features on the films. An Oriel 92521 floodlit lamp was used to carry out blanket DUV exposures whereas a Karl-Suss MJB-3 contact aligner and photomask were used for UV-patterning of lateral porosity patterns. DUV intensities were measured at 240-250 nm using calibrated UV intensity probes.

3.5.3 Solvent-Induced Porosity: Undercladding layer

3.5.3.1 Soak Step: Solvent Penetration and Gelation

Propylene carbonate and MIBK solvent were mixed in volumetric ratios of 1:1 and 3:1 to give co-solvent PC/MIBK solution. Although pure PC is a good gelation agent, it was observed that pure PC was unable to penetrate HSQ films owing to the rapid

crosslinking of the surface of the film on contact with the solvent. MIBK was used to facilitate the swelling of the HSQ films by the PC co-solvent. 100-150 ml volumes of these co-solvent solutions were poured into aluminum pans and then placed in preheated ovens at temperatures ranging from 60^{o}C to 150^{o}C. Spun-coated HSQ films of 0.9-1.2 μm thickness were then soaked for 20 minutes in the heated solutions to allow the co-solvents to penetrate the HSQ films. The PC molecules catalyzed the gelation of HSQ during the soak step, and the crosslinked films were either analyzed using FTIR (dried using a nitrogen spray gun) or immediately baked to volatilize the solvents as explained in the following subsection.

.

3.5.3.2 Bake Step: Solvent Volatilization

HSQ films penetrated by the PC-MIBK co-solvent mixtures were placed on a preheated hotplate to volatilize entrapped solvent from the crosslinked matrix, thus inducing porosity. The bake step was performed for over 30 minutes at temperatures ranging from 100^{o}C to 160^{o}C to drive off all residual solvent. The resultant porous films were then analyzed by FTIR to ensure removal of all solvents; the detection of carbonyl peaks (centered at about 1780 cm-1) in the FTIR spectra confirmed the presence of residual PC-MIBK molecules within the films. Ellipsometry was used to determine the drop in refractive index and thus estimate the extent of induced porosity within the HSQ films. Physical and chemical factors affecting the soak and bake steps are discussed in section 5.2 of the thesis.

3.6 Characterization of Refractive Indices

A J.A. Woollam M2000 VI spectroscopic ellipsometer was used together with a Cauchy model to find the refractive index values of porous and non-porous films during processing.[124] All refractive indices reported in this thesis are for a wavelength of 632 nm and when necessary, the extinction coefficients of the processed thin films were also fit using ellipsometry software. To track the refractive index differences between porous and non-porous areas of direct-written samples, one half of each sample was covered with a polished wafer during the UV-exposure step so as to prevent any UV-induced decomposition of polymer in the covered half. For all other steps, the entire direct-write film underwent identical processing conditions. The refractive indices of direct-write and thermally-processed porous films and their non-porous control samples are discussed in section 4.5. The refractive index values of solvent-induced porous films processed under varying bake temperatures are listed in section 5.2. The experimental refractive indices of slab waveguide regions are listed in sections 6.1 and 6.2 of the thesis.

3.7 Characterization of Dielectric Constants

In order to determine the intralayer dielectric constant of porous films and their non-porous controls samples, interdigitated electrodes (IDEs) were fabricated on oxidized silicon wafers, such as the one shown in Figure 3.5. Each IDE had 200 comb-like fingers connected to each bond pad with a 1 cm overlap length between adjacent comb fingers to give an overall field length of 4 m. Using the lift-off technique (photolithography followed by metal deposition onto patterned photoresist, followed by photoresist removal), the IDEs were patterned with 5 μm wide metal lines and 5 μm wide gap

spacing between each metal line. An e-beam evaporator was used to deposit 10-15 nm of titanium followed by 200 nm of gold at high vacuum onto least 10 μm thick PECVD SiO_2. A Tencor KLA profilometer and calibrated microscope were used to measure the actual dimensions of the IDEs and a Nanospec refractometer was used to measure the thickness of the PECVD oxide layer.

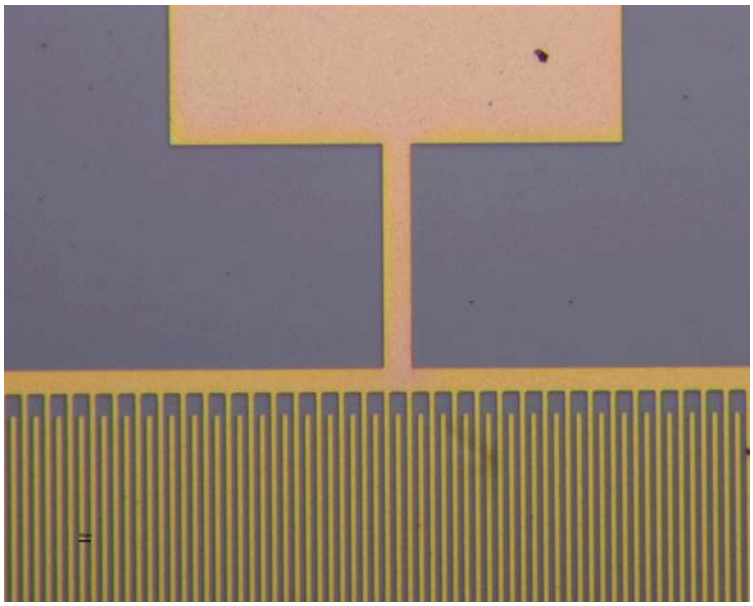

Figure 3.5 – Microscope image showing the top down view of an IDE.

An HP 4253 LCR meter and Karl Suss PM5 probe system were used to measure the capacitances of multiple IDEs at a frequency of 100 kHz both before and after spin-coating the silicon wafers with films. After spin-coating films onto the IDEs, portions of the films were removed by scraping to allow film thickness measurements to be performed by the profilometer. Both the thicknesses of the coated films and the capacitances of the coated IDEs were re-measured after each processing step. By utilizing the measured dimensions of the IDEs, and the measured thicknesses of the oxide

and coated films, electrostatic simulations (Ansoft's Maxwell software) were used to accurately model the capacitances of the IDEs and thus empirically determine the intralayer dielectric constants of the films.[3, 6, 9, 15-17, 50, 125, 126] The dielectric constants of the UV-processed and thermally-processed porous films and their control samples are compared in section 4.4 of the thesis.

3.8 The Use of Mixing Rules to Estimate Porosity

Effective medium approximations (EMAs) or refractive index and dielectric mixing rules are a widely used method of estimating porosity within thin films.[3, 9, 50, 126-128] In order to do this, the refractive indices (n) and/or dielectric constants (ε) of porous films are compared with those of a non-porous control samples and the EMAs are then used to solve for the relative porosity induced in the porous films.

3.8.1 Porosity Estimates via the Lorentz-Lorenz Mixing Rule

After using spectroscopic ellipsometry to determine the refractive indices of porous films, pure HSQ films were processed in a similar manner to their porous counterparts and their refractive indices were recorded. The Lorentz-Lorenz equation, shown in equation (3.1), was used then to model the effective refractive index, n_{12}, of a porous film.[3, 9, 50, 126] Since the refractive index of air (n_2 = 1.0003) is approximately equal to 1, the second term on the right hand side of the Lorentz-Lorenz equation was eliminated.[1] The resultant expression was then rearranged to explicitly solve for the volume fraction of air, ϕ_2, in a porous film, as shown in equation (3.2).[3, 9, 50, 126, 127] The refractive index values of the non-porous control samples (n_1) and their porous

counterparts (n_{12}) were then substituted into equation (3.2) to solve for the porosity, ϕ_2, of each porous film.

$$\frac{{n_{12}}^2 - 1}{{n_{12}}^2 + 2} = \phi_1 \left(\frac{{n_1}^2 - 1}{{n_1}^2 + 2} \right) + \phi_2 \left(\frac{{n_2}^2 - 1}{{n_2}^2 + 2} \right) \tag{3.1}$$

$$\phi_2 = (1 - \phi_1) = 1 - \left(\left[\frac{{n_{12}}^2 - 1}{{n_{12}}^2 + 2} \right] \Big/ \left[\frac{{n_1}^2 - 1}{{n_1}^2 + 2} \right] \right) \tag{3.2}$$

The symbols ϕ_1 and ϕ_2 are the volume fractions occupied by the host matrix and air pockets, respectively. The symbol n_{12} refers to the effective refractive index of the bulk porous film, while n_1 and n_2 are the refractive indices of the non-porous control film and air, respectively. [125, 127, 128] The porosity values estimated by the Lorentz-Lorenz EMA are shown in sections 4.5 and 5.2 of the thesis.

3.8.1 Porosity Estimates via the Maxwell-Garnett Mixing Rule

After determining the intralayer dielectric constants (ε) of the porous films using IDEs, pure HSQ films were coated on bare IDEs and processed and characterized in a similar manner to their porous counterparts and their non-porous control ε values were recorded. The Maxwell-Garnett mixing rule, equation (3.3), was then used to model the effective relative dielectric constant, n_{12}, of a porous film.[3, 9, 50, 126] In order to estimate the level of induced porosity from the dielectric constant data, equation (3.3) was then rearranged to explicitly solve for the volume fraction of air, $(1-\phi_1)$, in a porous film, as shown in equation (3.4).[6, 16, 17, 125, 127] The ε values of air, ε_2 the non-porous control

samples (ε_1) and their porous counterparts (ε_2) were then substituted into equation (3.4) to solve for the level of porosity induced within the porous films. [17]

$$\frac{{\varepsilon_{12}}^2 - \varepsilon_2}{{\varepsilon_{12}}^2 + 2\varepsilon_2} = \phi_1 \left(\frac{{\varepsilon_1}^2 - \varepsilon_2}{{\varepsilon_1}^2 + 2\varepsilon_2} \right) \tag{3.3}$$

$$\phi_2 = (1 - \phi_1) = 1 - \left(\left[\frac{\varepsilon_{12} - \varepsilon_2}{\varepsilon_{12} + 2\varepsilon_2} \right] \Big/ \left[\frac{\varepsilon_1 - \varepsilon_2}{\varepsilon_1 + 2\varepsilon_2} \right] \right) \tag{3.4}$$

Similar to equation (3.2), the symbols ϕ_1 and ϕ_2 are the volume fractions occupied by the host matrix and the pores, respectively. The symbol ε_{12} refers to the effective dielectric constant of the porous film, and ε_1 and ε_2 refer to the relative dielectric constants of the host matrix and air, respectively. Since ε_2 is equal to unity for air, and since the square of the refractive index of any component is equal to its relative dielectric constant value, equations (3.2) and (3.4) are mathematically equivalent for a porous film. This indicates that theoretically, the porosities that were estimated using experimental data and Lorentz-Lorenz and Maxwell Garnett rules should have matched. To test for consistencies of the porosity estimations the calculated using optical experimental data were compared with those calculated from experimental dielectric constant data and any discrepancies were noted. As an additional method of validating the porosity estimates, comparison were made between the EMA results and films porosities reported in literature for similar sacrificial polymer loadings. The porosity values estimated by the Maxwell-Garnett EMA are shown in section 4.4 of the thesis.

3.9 Characterization of Internal Pore Structure via TEM

A focused gallium ion beam (FIB) was used to prepare thin cross-sections of porous films after first sputtering each of these samples with protective gold and platinum layers to prevent gallium implantation during milling.[93, 94, 129] In order to characterize the internal pore structure of the porous layers, the thin cross-sections were mounted onto TEM grids and then analyzed using a Hitachi HF-2000 high resolution TEM. The TEM was operated using an accelerating voltage of 200 kiloelectron volts (keV), and the TEM results are discussed in sections 4.6 and 4.7.

3.10 Characterization of Surface Morphology via AFM

In order to determine the surface profiles of porous films, they were analyzed using a Veeco Dimension 3100 atomic force microscope (AFM). The AFM was operated in TappingMode™ (intermittent contact) using silicon nitride tips, which had radii of curvature of 7 nm. 512 raster scans were used to generate each AFM image and the sizes of the scanned areas ranged from 2 μm by 2 μm to 10 μm by 10 μm. The root mean square (rms) roughness values of the films surfaces were recorded along with the dimensions of surface anomalies such as depressions. The AFM results are discussed in section 4.7.

3.11 Direct-Write Porous Waveguides

3.11.1 Design and Fabrication of Type I and Type II Porous Slab Waveguides

Glassy-state processing of porous films was used to build the two types of slab waveguide structures, called type I and type II depending on the type of slab waveguide

structure fabricated. For both types of waveguides, the solvent-processed porous films were the lowest layers while the direct-written porous films served as topmost layers. For the type I waveguides, the direct-write layer was the guiding layer and air served as the upper-cladding, or cover layer of the waveguides. For type II waveguides, PECVD SiO_2 layers were the guiding layers and the direct-write films were their upper-cladding layers. For both types of waveguides, photomasks were used to selectively expose the direct-write guiding layers during the UV-exposure step such that the unexposed regions remained non-porous and had higher refractive index values than the irradiated porous regions. Thus the photomask patterns allowed lateral refractive index profiles to be created within the direct-write layers of the waveguides. These refractive index profiles directly and indirectly defined the cores (highest index areas) and side-cladding areas of the guiding layers of the type I and type II waveguide structures, respectively.

For type I waveguides, the non-porous regions acted as the waveguide cores since these regions had the highest refractive index values (other regions were either porous or occupied by air). The UV-induced porous regions were the side-cladding areas, since they were laterally adjacent to the cores. The layers within the waveguide structures were processed sequentially, as shown in Figure 3.6. The lowest layer consisted of a solvent-induced porous film that was processed in a similar manner to other solvent-induced porous as described in an earlier section. Above this solvent-processed layer was a middle layer of either a non-porous HSQ film or PECVD SiO_2 for type I and type II structures, respectively. The purpose of these buffer layers was to isolate the solvent-processed layers from the upper direct-write layers, since it was observed that residual

solvents in the undercladding layers adversely affected the processing of the direct-write layer when the buffer layers were not used.

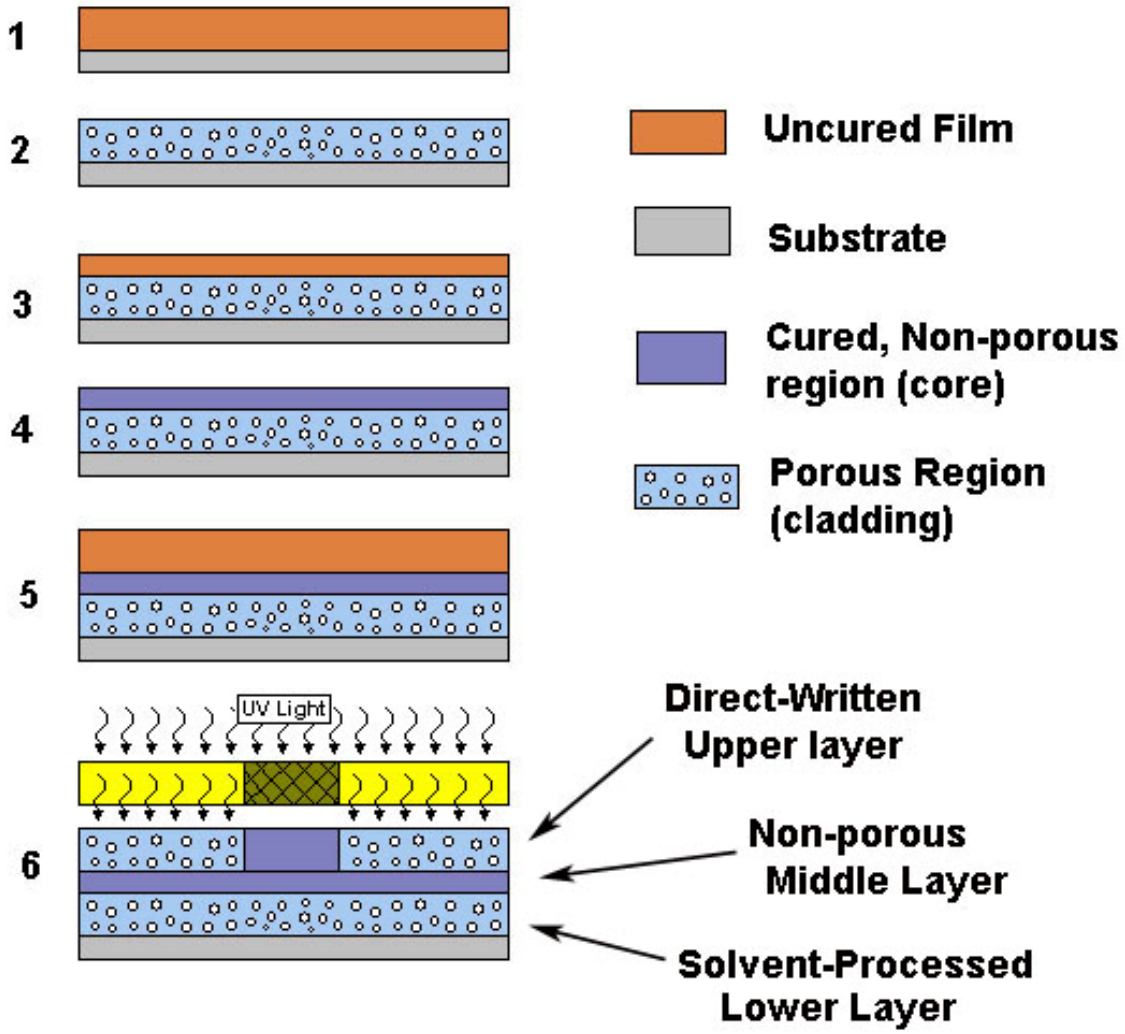

Figure 3.6 – General processing sequence for fabricating porous direct-write slab waveguides

For type I waveguides, the pure HSQ layers were spin-coated from FOx-1x resin onto solvent-induced porous films to thicknesses of about 200 nm prior to thermally curing by heating the wafer in a nitrogen-purged Lindbergh furnace at 200^{o}C for 2 hours.

For type II waveguides, about 700 nm of SiO_2 was directly deposited via PECVD using the following plasma chamber conditions: chamber temperature of 300°C, RF power of 20 W, 1420 standard cm^3 (sccm) of N_2O gas and 400 sccm of 2% SiH_4 in N_2 carrier gas.

To produce the upper layers, direct-write formulations were spun-coated above the middle layers and processed in a similar manner to other direct-write films, as described in earlier sections. After each stage of the waveguide fabrication, ellipsometry and AFM analyses were used to track the refractive indices and surface roughness of each of the layers, respectively. For type II waveguides, the cores and side-cladding areas were situated in the SiO_2 layers and directly below the non-porous and porous areas of the direct-write films, respectively.

3.11.2 Modeling of Slab Waveguide Properties

3.11.2.1 Determination of Guiding Layer Cutoff Thickness

According to established waveguide theory, slab waveguides with symmetric refractive index profiles (both in vertical and lateral directions) always support at least one guided mode. However, waveguides with asymmetric refractive index profiles have cutoff guiding layer thicknesses, below which light can no longer be confined within the waveguide (i.e. no light guiding takes place). To ensure that the fabricated type I and type II waveguides were able to support guided modes, slab waveguide calculations were used to determine the cutoff thicknesses of the guiding layers in each of the structures, as shown in equations 3.5 and 3.6.

$$a_{TE} = \frac{\left| {n_S}^2 - {n_c}^2 \right|}{{n_f}^2 - {n_S}^2} \tag{3.5}$$

$$h_{\infty} = \lambda \left(\frac{\tan^{-1} \sqrt{a_{TE}} + v\pi}{2\pi \sqrt{{n_f}^2 - {n_S}^2}} \right) \tag{3.6}$$

The symbols a_{TE} and h_{∞} refer to the asymmetric parameter of the TE mode (equal to zero for symmetric slab waveguides), and the cutoff thickness of the guiding layer, respectively. The calculated cutoff thicknesses of the guiding layers of the type I and type II waveguides are compared in section 6.1 of the thesis.

3.11.2.2 Determination of Effective Index and Propagation Constant

According to established optical theories of thin films, the effective refractive index of a multi-layered structure is an aggregate of the refractive indices and heights of all the layers that comprise it. Thus when one or more layers have a lateral refractive index profile, this induces a lateral effective index profile within the entire multi-layered structure. This is because when a vertical slice is made, which passes through the higher indexed regions of the direct-write layer, the calculated effective refractive index is higher than if the vertical slice passes through the lower refractive index regions (i.e. the porous areas of the direct-write layers).

As shown in section 6.2, the refractive index profiles within direct-write layers affected the location of cores and side-cladding regions due to their influence on the overall effective index profile of both types of waveguide structures. For this reason, light was laterally confined in areas that were located along the same vertical axes as the non-porous parts of the direct-write films (since these regions had higher effective refractive indices than those lying along the same vertical axes as the UV- porous areas).

Side-cladding regions, by definition, are laterally adjacent to cores thus the side-cladding regions were also located within the guiding layers but along the vertical axes that passed through the UV-induced porous regions. For each type of waveguide, light was vertically confined within the layer with the highest intrinsic refractive index. For type I waveguides, the guiding layer was the direct-write film since the its non-porous region had a higher index than the other regions in its waveguide structure, but for type II waveguides, the guiding layer was the SiO2 layer. Thus, even though the *intrinsic* refractive index of SiO_2 was uniform across each wafer, the effect of the direct-written index profiles allowed light to be confined laterally within the SiO_2 guiding layers of type II waveguides.

Since mode matching between layers is necessary for guiding in multilayered structures, optics researchers solve complex eigenvalue equations to determine their effective indices.[129] Numerical optical models were used to solve the complex transcendental equations describing the type I and type II multilayered slab waveguide structures in order to determine the effective indices and propagation constants of for each of the guided modes supported by the waveguides.[45, 82, 89]

3.11.3 Characterization of Waveguide Attenuation

Attenuation is one of the key parameters used to characterize optical interconnect performance and it refers to the loss of signal strength due to absorption, scattering, and coupling losses from light source to the detector.[89] Thus the distance that light may be transmitted by a single channel before having to be sent to a detector is limited by transmission losses. After using a photomask to pattern the direct-write layer, the

waveguide substrate (silicon wafer) was cleaved such that the cleaved edges were perpendicular to the non-porous waveguide channels. An optical fiber, which was used to confine light that was emitted at 635 nm by a photodiode, was then aligned to an exposed edge patterned waveguide core and then brought into intimate contact with the input face of the channel in order to couple light into the waveguides (endfire coupling).[89] To characterize the propagation of light in the direct-written cores, an optical apparatus setup was used, as shown in Figure 3.7.[89]

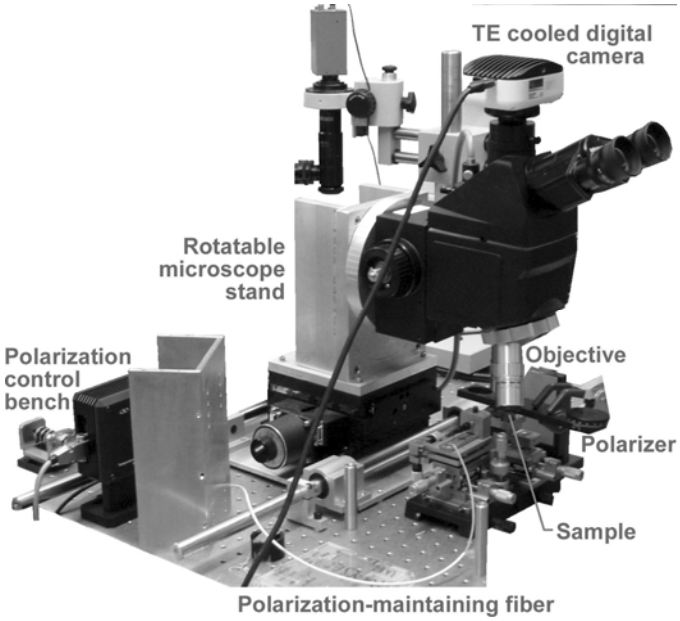

Figure 3.7 – Optical apparatus used to analyze the guiding of light in the waveguides

An end-view CCD camera objective was aligned to the output edge of the channel that was aligned to the optical fiber in order to capture the image of the waveguide core that is illuminated by the propagating light.[45, 82, 89] The purpose of the end-view images was to observe mode patterns of light propagating in the direct-written cores and thus ensure light confinement within the waveguide channel. Another CCD camera objective

was used to capture a top-down view of the light scattered from the top of the waveguide channel.[89] The purpose of the aerial image was to characterize the light power loss per unit length along the waveguide.[89, 94]

The image of the light scattered from each waveguide channel was digitized and then analyzed by MATLAB software and the normalized power loss per unit length of the channels (in cm^{-1}) was plotted and fit to the exponential decay function shown in Equation (3.7).[89, 94] By using the logarithmic conversion shown in Equation (3.8), the power loss along each waveguide was converted to decibels per centimeter (dB/cm).[31] The average power loss in dB/cm was then found for each direct-written wafer and recorded.

$$P(z) = P_0 e^{-\alpha * z} \tag{3.7}$$

$$\alpha(dB/cm) = 10 * \left[\log_{10}(e)\right] * \alpha(cm^{-1}) \tag{3.8}$$

The symbol z refers to the distance traveled by light along the direction of mode propagation, P_0 represents the initial power of the light in the waveguide (i.e. power at z = 0), and P(z) represents the power of the light in the waveguide at the point z. The symbols $\alpha(cm^{-1})$ and α(dB/cm) refer to the power loss per centimeter in exponential and decibel scales.

CHAPTER 4: PROPERTIES OF POROUS FILMS FORMED VIA DECOMPOSITION OF POLY(NORBORNENE CARBONATE)

4.1 Thermal and Acid-Catalyzed Decomposition of Polycarbonates

The onset of thermolysis of neat PNC begins just above 270^{o}C, and its final decomposition temperature is 325^{o}C.[30, 31] According to literature, acids are able to catalyze the decomposition of polycarbonates, effectively decreasing the temperature at which they begin to depolymerize and volatilize.[30, 31] According to the reported mechanism, protons from the acid attack the carbonyl group of a polycarbonate, such as the one shown in Figure 3.1, resulting in main chain scission of the sacrificial polymer and the evolution of volatile decomposition products.[30, 31] By performing TGA studies, researchers have been able to determine the usefulness of PAGs in facilitating the of acid-catalyzed decomposition of polycarbonate-based polymers.[30, 31] The larger the temperature difference between the onset of photolytic decomposition (irradiated PAG, UV-released acid) TGA curve and the thermolytic decomposition (no UV, acid thermally-released) TGA curve for a polymer/PAG mixture, the wider the temperature window for the PEB i.e. the higher the likelihood of decomposing most or even all of the polymer in the exposed region without decomposing any of the PNC in the unexposed region of the wafer. Thus, PAG/PNC mixtures with the largest differences between thermolytic and photolytic TGA curves were deemed optimal for use in the PAG/polycarbonate direct-write formulations, since they could be used both for producing blanket as well as patterned porosity within films. The thermal stabilities of neat PNC and PNC/PAG mixtures (PAGs shown in Figure 3.3) were compared using

TGA analysis, and their decomposition profiles are discussed in the following subsections.

4.1.1 Non-Isothermal Decomposition Profiles of PNC

4.1.1.1 Neat PNC vs PNC/Diphenyl Iodonium PAG Mixtures

PAGs with diphenyl iodonium cations tend to have low thermal stability as can be seen in the TGA plot of Rhodorsil 2074/PNC mixtures shown in Figure 4.1.[41]

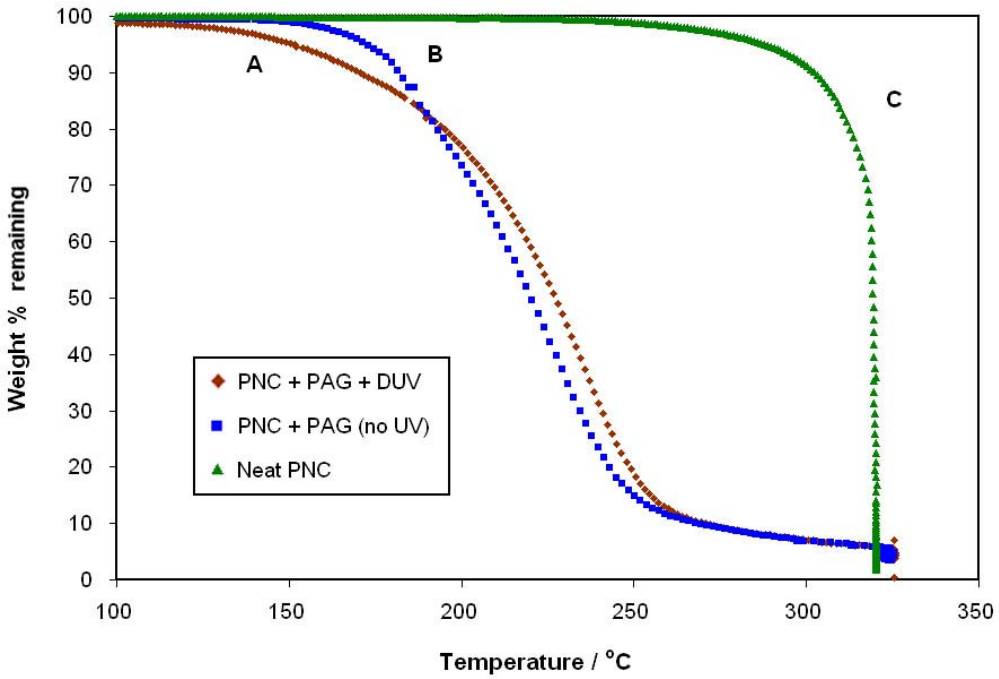

Figure 4.1 – Non-isothermal TGAs of (A) a PNC/Rhodorsil 2074 mixture exposed to 1 J cm^{-2} DUV radiation, (B) an unexposed PNC/Rhodorsil 2074 mixture, and (C) pure PNC.

The onset temperature for thermal degradation (T_d) of Rhodorsil 2074 was not significantly higher than the PEB temperature required to photogenerate the acid [hydrogen tetrakis(perflourophenyl)borate or HTPFPB]. However, as state previously a

PAG must have a high thermal stability to be compatible with selective decomposition of PNC. Otherwise, direct-written refractive index profiles in a film will be destroyed upon heating the film to moderate temperatures due to the thermal activation of the PAG. This is because sacrificial polymer chains both in exposed and unexposed regions would be decomposed by the acid molecules, hence, selective decomposition would not be achieved. Thus Rhodorsil 2074 was likely to thermally release its acid during direct-write processing and was not compatible with selective UV-patterning of porosity.

4.1.1.2 Neat PNC vs PNC/Triphenyl Sulfonium PAGs

Ionic PAGs with cations derived from the photosensitive triphenyl sulfonium moiety are attractive due to their high thermal stability relative to diphenyl iodonium PAGs.[41] As seen in Figure 4.2, TTBPS-Tf had the following desirable properties: relatively high thermal stability with respect to the PEB temperatures required to decompose PNC after UV-exposure as well as the ability to decompose PNC rapidly due to the high strength of the photoacid released (triflic acid).[60, 65]

Further TGA studies showed that TTBPS-Nf had desirable properties similar to TTBPS-Tf as seen in Figure 4.3. Hence, it was determined that TTBPS-Tf and TTBPS-Nf were suitable PAGs to incorporate in the direct-write system.

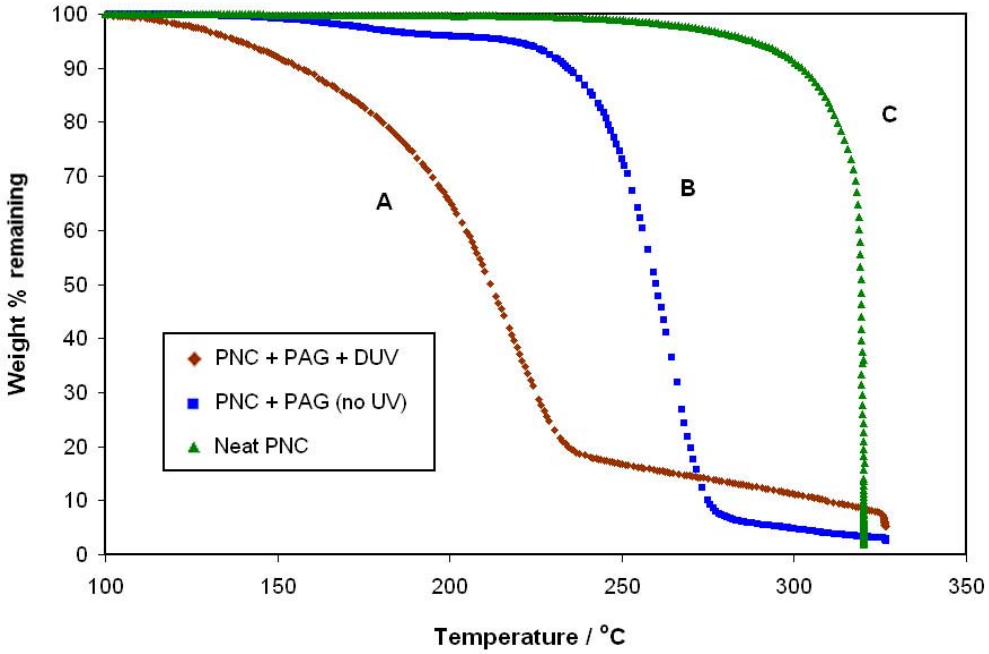

Figure 4.2 – Non-isothermal TGAs of (A) a PNC/TTBPS-Tf mixture exposed to 1 J cm^{-2} DUV radiation, (B) an unexposed PNC/ TTBPS-Tf mixture, and (C) pure PNC.

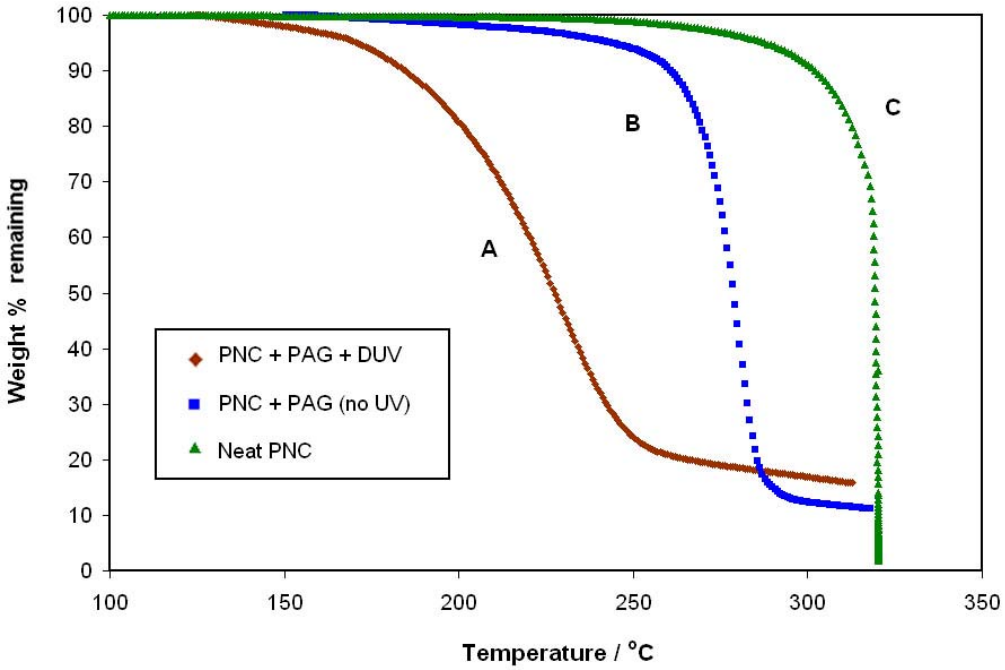

Figure 4.3 - Non-isothermal TGAs of (A) a PNC/TTBPS-Nf mixture exposed to 1 J cm^{-2} DUV radiation, (B) an unexposed PNC/ TTBPS-Nf mixture, and (C) pure PNC.

4.1.2 Isothermal Decomposition Profiles of PNC/TTBPS-Tf Mixtures

In order for the SOG matrix to mechanically support porosity, it must be rigid enough to avoid pore collapse during decomposition of the sacrificial polymer. In conventional SOG processing, the resins are spin-coated onto silicon wafers to form planar dielectric films that become rigid when heated above their glass transition temperature. [61, 57, 60, 65] Although HSQ is typically thermally cured above 350°C, researchers reported evidence for HSQ cure reactions below 350°C, [63] and we have successfully hardened HSQ by baking them at 200°C for 2 hours. To determine the compatibility of thermal curing with the direct-write process shown in Figure 3.4, isothermal TGA studies of TTBPS-Tf/PNC mixtures were performed for several temperatures above and below the glass transition temperature of the HSQ matrix (194-195°C determined by DSC).[65] The results of the isothermal TGA experiments, shown in Figure 4.4, indicated that above the glass transition temperature, the PNC/PAG mixtures experienced significant loss, and the rate of the weight loss increased with increasing temperature.

This is because at temperatures above 195°C, TTBPS-Tf was thermally activated to produce triflic acid, leading to acid-catalyzed decomposition and volatilization of PNC. However, at temperatures below 195°C, the PNC/PAG mixture experienced a total weight loss of less than 5 wt% even after being heated isothermally for up to 2 hours, showing that at temperatures below the glass transition temperature of the HSQ matrix, either the PAG was thermally stable or the rate of acidolytic decomposition of PNC was very low.

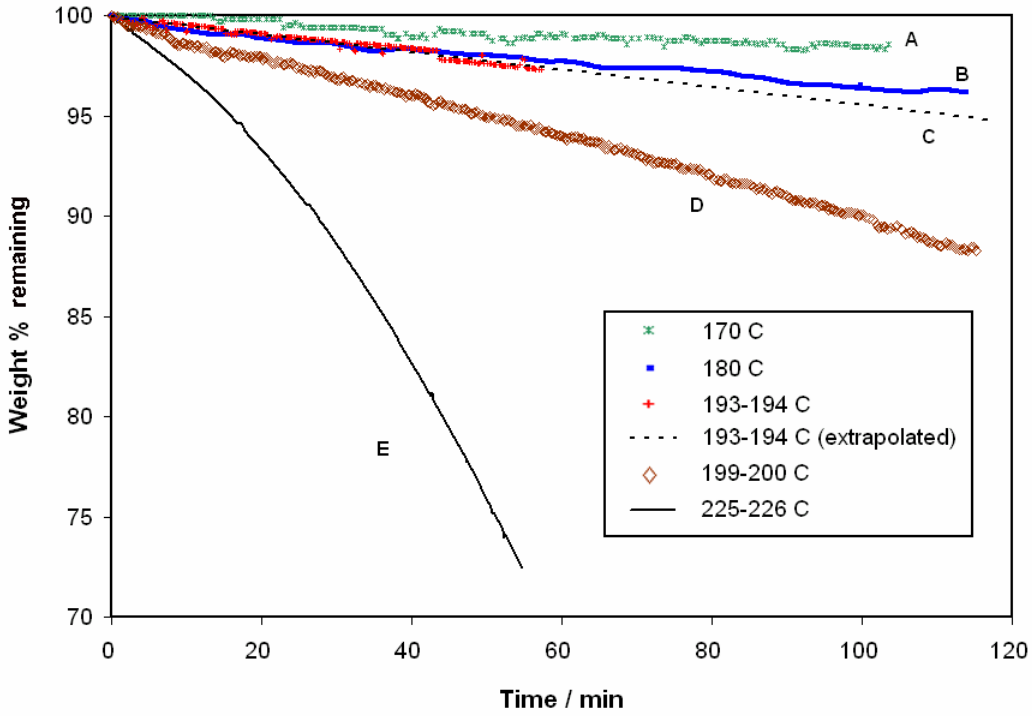

Figure 4.4 – Isothermal TGAs of unexposed PNC/TTBPS-Tf mixtures held at (A) 170°C, (B) 180°C, (C) 193-194°C [with experimental data extrapolated past 60 min], (D) 199-200°C, and (E) 225-226°C.

Ellipsometry provided further evidence for the thermal activation of PAGs above the glass transition temperature of HSQ in that the refractive index of HSQ/TTBPS-Tf/PNC films with a PNC loading of 10% dropped from 1.413 to 1.365 when heated at 200°C for 2 hours without any prior irradiation whereas that of non-porous control films (no PNC) remained at about 1.38 after undergoing the same bake conditions. Hence, the curing of HSQ above its glass transition temperature was deemed incompatible with the direct-write process because it would lead to the thermal activation of the PAG and hence the decomposition of PNC throughout the film. However, due to low chain mobility, the thermal curing of HSQ below its glass transition temperature occurs on too large a timescale for feasible mass fabrication of direct-write films.

4.2 Low-Temperature Crosslinking of HSQ Films via Gelation

To harden HSQ relatively quickly while simultaneously avoiding thermal activation of the PAG in the direct-write process, bases were used to catalyze the hydrolysis of the silane bonds in HSQ to form silanol groups at relatively low temperatures.[4, 64, 112, 113, 130, 131] These silanol groups were highly reactive and condensed to form siloxane bonds, thus increasing the rigidity of the film.[2] This low-temperature gelation reaction was used during the first of the processing steps shown in Figure 3.4 to make the HSQ matrix rigid enough to support porosity without the problems associated with thermal activation of the PAG. A possible mechanism for the hydrolysis of silanes, proposed by Sommer, involves the induced polarization of the silicon center by a nucleophile followed by the attack of the electropositive silicon center by a water molecule, as shown in Figure 4.5.[2]

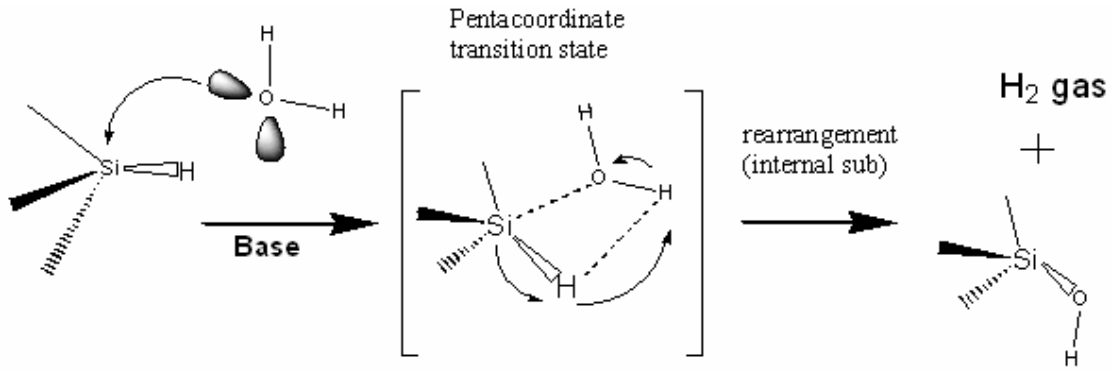

Figure 4.5 – The S_ni-Si mechanism of silane hydrolysis proposed by Sommer.[2]

The d-orbitals present in silicon atoms allow silicon centers to form pentacoordinate and hexacoordinate transition states during reactions.[2, 132] There is an internal rearrangement of the temporary bonds in the transition state that leads to a silanol

group replacing the silane group.[2, 132] According to West, the hydrolysis of cyclic silanes such as HSQ cages is thermodynamically favorable because the pentacoordinate transition state relieves the bond strains present in the original cyclic structures.[133]

4.2.1 Ammonia Gas and Photogenerated Bases as Gelation Catalysts

According to literature, the FTIR spectrum of HSQ has stretch peaks centered at (2250 cm^{-1}), (1130 cm^{-1}) and (1070 cm^{-1}) corresponding to silane, cage-type siloxane, and network-type siloxane bonds respectively.[134] When spin-coated HSQ films were exposed to ammonia gas, the FTIR stretch peak due to the silane bonds decreased, and a small peak centered at 3740 cm^{-1} appeared, as shown in Figure 4.6.

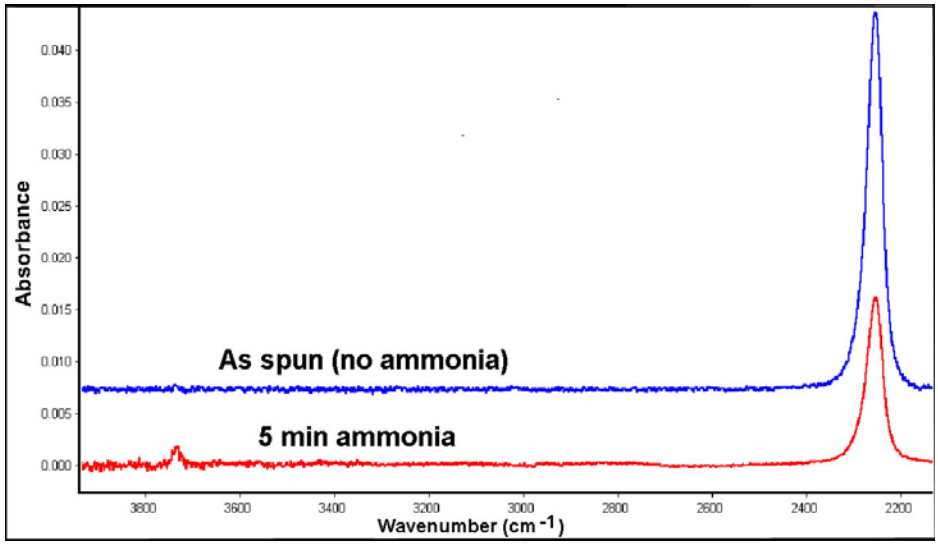

Figure 4.6 – Comparison of the silane and silanol content between an as spun HSQ film with a film gelled for 5 minutes using saturated ammonia vapor at 25°C. The baseline of the as spun spectrum was offset for clarity.

The new peak arose from the formation of silanol bonds, hence the supporting Sommer's hypothesis that silane bonds are converted to silanol bonds during gelation.[2, 4,

[64, 112, 113, 130, 131] Silanol bonds were very reactive, and subsequent condensation of adjacent silanol bonds resulted in the formation of network-type siloxane bonds thus increasing the area of the siloxane network peak in the FTIR spectra.[133] The ammonia treatment also caused the siloxane cage-type peak to decrease, and the peak corresponding to siloxane network-type bonds to increase, as shown in Figure 4.7.

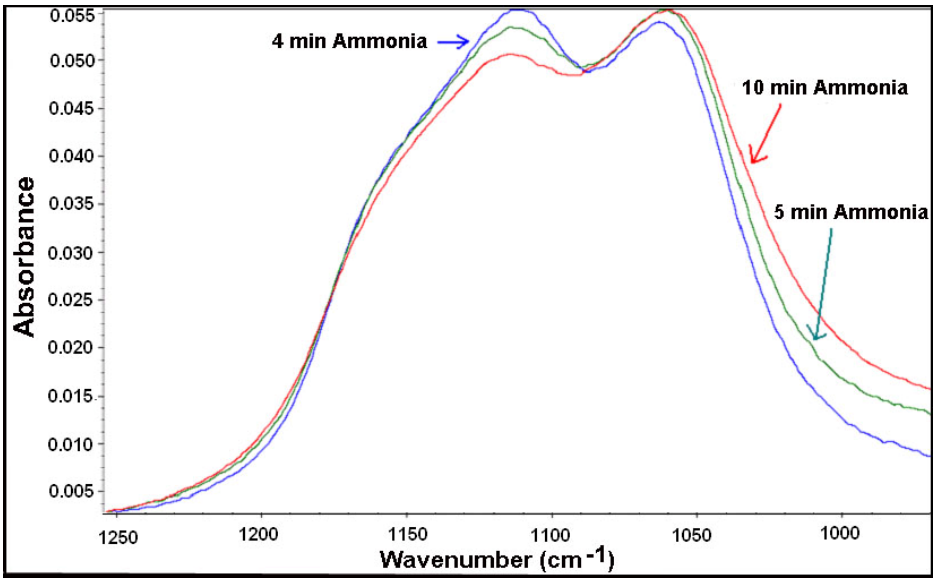

Figure 4.7 – Comparison of cage and network-type siloxane peak in HSQ films gelled for 4 (blue), 5 (green), and 10 minutes (red) using saturated ammonia vapor at 25°C.

The decrease in cage-type siloxane peaks was due to the scission of these bonds via base-catalyzed hydrolysis, which resulted in the opening up the cage structure to form a pentacoordinate transition state.[133] The transition state then preferentially rearranged during condensation to form an open network structure, which had less bond strain than the closed cage structures as described by West.[64, 65] Hence, during gelation, the ratio of siloxane cage to siloxane network peak areas decreased and as done by other researchers, this ratio was used as a measure of extent of HSQ crosslinking reaction.[48, 107, 108, 114, 135]

Similar to methods cited in literature, photobase generators (PBGs) were mixed in formulations with HSQ in order to harden the matrix upon activation of the PBG via blanket UV-exposure or by thermal activation.[112, 113] Once activated, the PBGs released bases that catalyzed the cross-linking of HSQ units via the sol-gel condensation of silanol bonds formed from the hydrolysis of silane bonds and rearrangement of hydrolyzed cage-type siloxane bonds to network-type bonds.[57, 58, 64] The average reduced moduli (E_r) of films gelled using either a basic vapor (ammonia gas) or a photobase are shown in Figure 4.8 along with their respective FTIR cage/network peak area ratios.

It can be seen from Figure 4.8 that the reduced modulus of gelled films increased as the cage/network peak area ratio decreased.[48, 108, 112-114, 135] This confirmed that as the relative amount of networked siloxane bonds to cage bonds increased, the HSQ matrix became more rigid. HSQ films that were exposed to saturated ammonia vapor for 3 minutes at ambient conditions had a final E_r of 3.65 GPa. This was observed to be about the same rigidity of gelled HSQ/PBG films with initial CTS or NBC loadings of about 3 wt% with respect to dry HSQ. The loading of N-methylnifedipine required to give an equivalent reduced modulus after activation of the PBG was only 1 wt% with respect to HSQ. As shown in Figure 4.9, when compared on the basis of equivalent loading weight in HSQ, the N-methylnifedipine PBG is the most efficient at crosslinking HSQ.

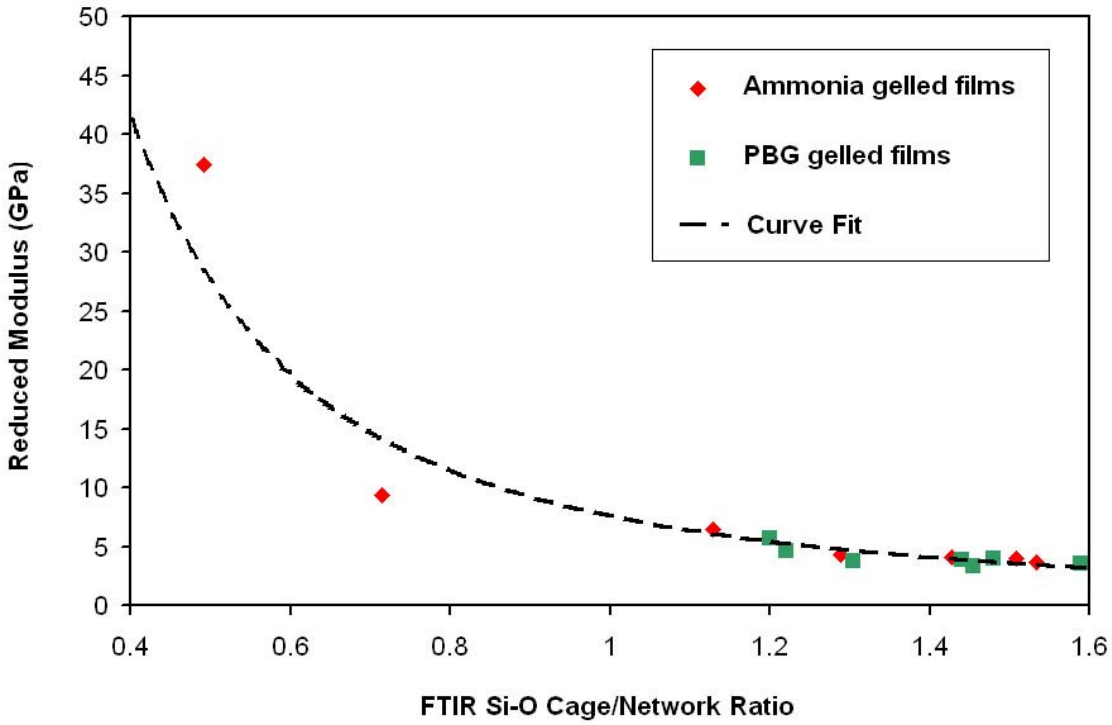

Figure 4.8 – Plot showing correlation between reduced moduli and c/n ratios for HSQ films gelled using (♦) ammonia vapor at ambient temperature and (□) UV-released bases from PBGs after PEBs. For clarity, a curve fit (----) is used to show the trend in the data.

Since the molecular weight of N-methylnifedipine is the largest of the three PBGs studied, then even on a molar basis its released base (alkylammonium hydroxide) is much more efficient at hardening HSQ than the base (cyclohexylamine) released by the other two PBGs.[4, 54, 64, 112, 113, 122, 130-132] The presence of direct-written porosity in cladding areas was indicated by refractive index values dropping below that of pure HSQ control films (1.389) that underwent similar heating cycles. By using the Lorentz-Lorenz refractive index mixing rule to estimate induced porosity, it was observed that the level of rigidity needed for direct-written films to be able to support 10 vol% porosity corresponded to E_r values of at least 3.5 GPa while 20 vol% porosity required E_r values of over 4 GPa. Films with E_r less than 3.1 GPa after gelation had refractive indices equal

to that of the HSQ control samples after the decomposition of PNC. This result implies that the matrix was not rigid enough to support porosity because pores that were formed ultimately collapsed resulting in non-porous HSQ films.

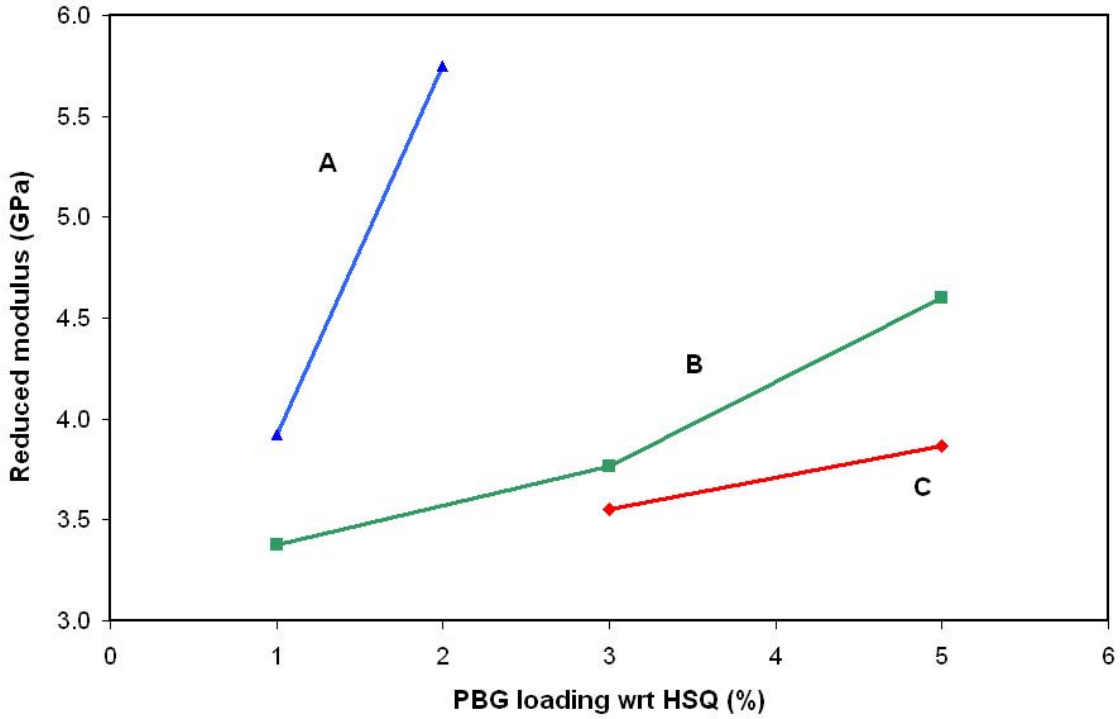

Figure 4.9 – Relative comparison of mechanical rigidity induced by bases released by (A) N-methyl nifedipine, (B) NBC, and (C) CTS at different PBG loading levels.

4.2.2 Gelation-Induced Film Shrinkage

As stated earlier, during gelation, silanol bonds are formed, which later condense via sol-gel reactions to form siloxane bonds. [5, 54, 122, 131, 132] As the silanol bonds condense into siloxane bonds, water molecules are produced as the by-products, as shown in equation 4.1.[10, 60, 64, 65, 73, 102]

$$\text{—Si-OH} + \text{HO-Si—} \rightarrow \text{—Si-O-Si—} + H_2O \quad (4.1)$$

As siloxane bonds are formed and water molecules are displaced from the sol-gel skeletons, the film density increases along with the increases in rigidity.[57, 63] Although sol-gel reactions are reversible, the water molecules produced during the gelation step of the direct-write process were permanently lost during bake steps as a result of volatilization. Researchers have shown that in addition to hardening films, the sol-gel chemical interactions result in film shrinkage, which can be very significant since a water molecule is generated for every pair of silanol bonds that react directly with each other. To determine the degree of film shrinkage induced by gelation, the thicknesses of all gelled HSQ films were tracked using ellipsometry and recorded. It was observed that both ammonia-treatments and photobase treatments caused HSQ films to shrink by about 5-6% with respect to the thicknesses of as-spun films.

In comparison to the gelation effects, standard thermal curing of HSQ (baking for about an hour above the T_g of HSQ, typically at 350-400^{o}C) only causes the film thicknesses of HSQ films to decrease by less than 1%.[63] Thermal cure reactions do not result in large amounts of film shrinkage because the structural transformations that occur during thermal crosslinking of HSQ, are only rearrangement and redistribution reactions, and there are no condensation reactions (unless the cure temperatures are above 400^{o}C, since oxidation reactions occur at these conditions).[136, 137] As discussed in a later section, the differences in film shrinkage effects caused by gelation and thermal cure reactions result in morphological differences in the internal pore structures of direct-written and thermally-processed porous films.

4.2.3 Influence of Water Content on Extent of Gelation

According to the hydrolysis mechanism shown in Figure 4.5, water is necessary for the hydrolysis of the silane bonds in HSQ to occur, and thus it predicts that the water content in the gelled films and/or the vapor above the films is a key factor affecting the extent of gelation of HSQ. In order to validate this, multiple experiments were conducted to test the ability of ammonia gas to catalyze the gelation of HSQ films that were pre-dried on hotplates at about 100^{o}C to drive off the trace amounts of water in the films. Even though the physical conditions were kept constant with those of non-dried films (referred to as 'standard conditions'), which were described in the previous sections, Table 4.1 and Figure 4.10 show that ammonia was not able to gel these films to any significant degree since their c/n ratios remained as high as original values of as-spun films.

Table 4.1 – Comparison of ranges of c/n ratios of multiple HSQ films treated with ammonia gas for 10 minutes under varying physiochemical conditions

Temperature of ammonia treatments	c/n ratio of pre-dried films	c/n ratios of films treated under standard conditions	c/n ratios in humidified chambers
25^{o}C	1.61	1.39-1.41	1.0-1.11

Although the gelation-catalysts were present in the pre-dried films, the amount of water molecules that were available to take part in the hydrolysis of silane bonds was negligible and thus very few silanol bonds were formed, leading to poor gelation results. As a confirmation of the overwhelming importance of water content in the HSQ gelation system, ammonia treatments were repeated as before but using non-dried HSQ films and

performed in chambers that were pre-humidified with steam. These humidified conditions resulted in much lower the c/n ratios, as shown in Table 4.1, indicating that higher levels of humidity favored gelation.

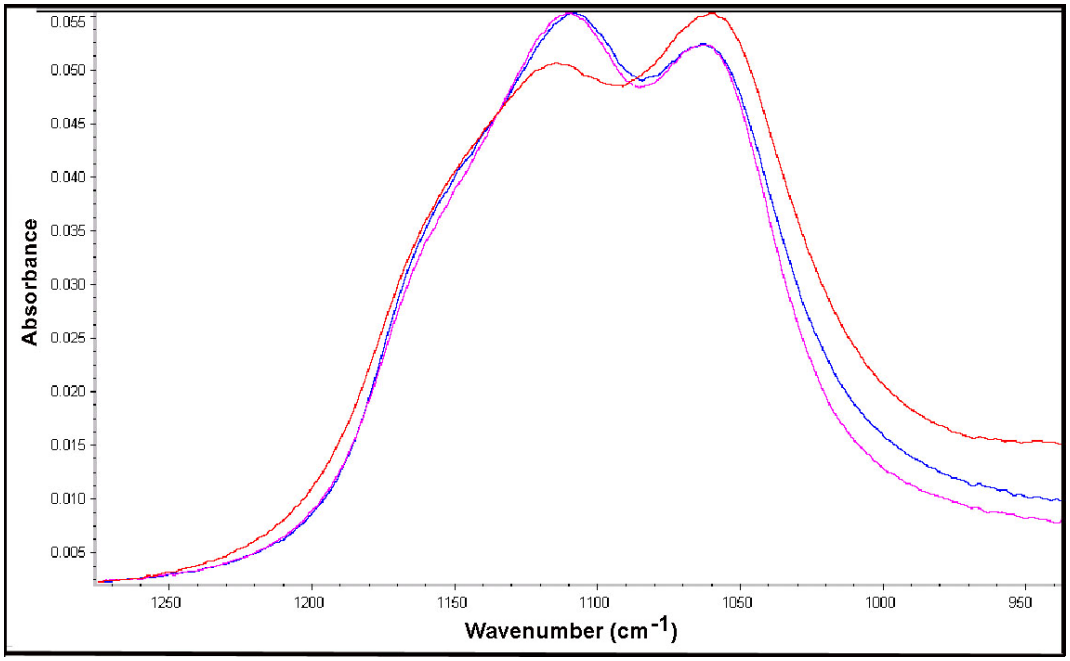

Figure 4.10 – FTIR spectra of HSQ films that were as-spun (pink), gelled for 10 minutes using standard ammonia treatments (red), and pre-dried ammonia treated films (blue)

To further test the influence of water content on the gelation of HSQ films, standard ammonia treatments were performed at elevated temperatures, and FTIR was used to compare the gelation results with those of ambient runs. As shown in Figure 4.11, the degree of crosslinking of HSQ *decreased* dramatically as the oven temperature was increased from ambient to 50°C and again when increased further to 100°C; the FTIR curves of films treated with ammonia at both 50°C and 100°C were barely distinguishable from as-spun films, indicating that a negligible amount of gelation reactions had occurred at these temperatures. These results were unexpected because according to the Arrhenius

effect, the pre-exponential rate constants for the gelation reaction should have increased as temperature was raised. Additionally, increases in temperature drove more ammonia gas from the aqueous ammonia solutions into the vapor phase, leading to increases in the amount of ammonia catalyst in the system.

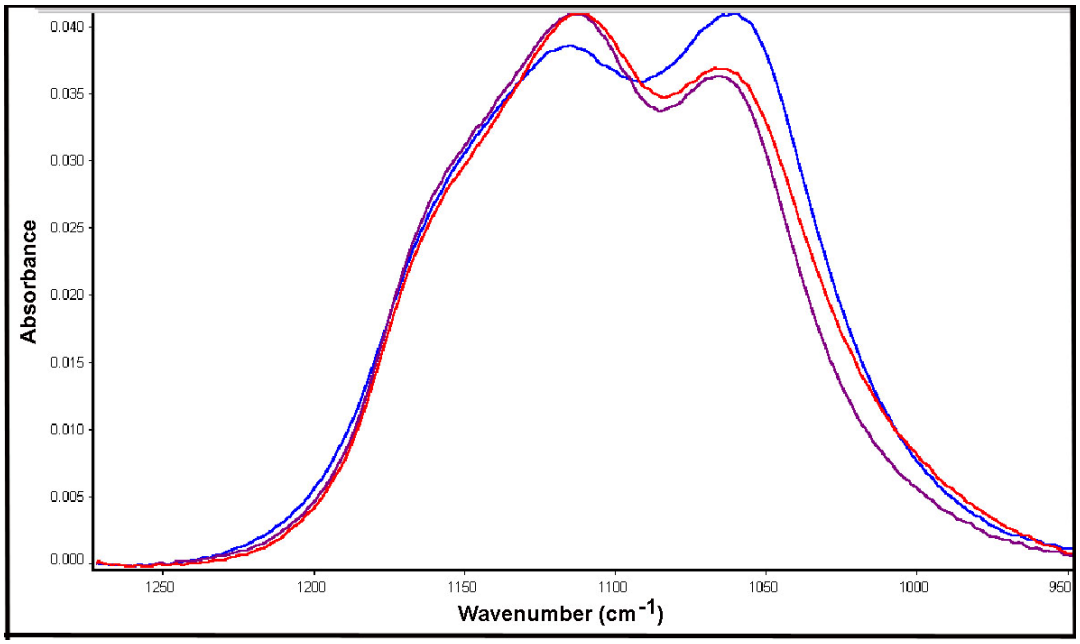

Figure 4.11 - Comparison of crosslinking in HSQ films that were exposed to ammonia for 10 minutes at 25°C (blue), 50°C (red), and 100°C (purple).

To understand the results, we must take into account that as the oven temperatures were increased, more water was driven from the HSQ films into the vapor phase. Since the HSQ films had only trace amounts initially, the above-ambient temperatures effectively hindered the base-catalyzed crosslinking of the films by removing the water molecules necessary for hydrolysis of the silane bonds within the films. The effective decrease in water content as the temperature was raised played a more crucial role in dictating the extent of gelation of the HSQ films than the increases in both the pre-

exponential rate constants and the amount of ammonia catalyst. By combining the results shown in Figure 4.11 with those shown in Figures 4.10 and Table 4.1 it is clear that the amounts of water molecules present in the system used for gelation films, either within the films or within the air above the films, was the most dominant factor affecting the degree of crosslinking of HSQ films. This is because, unlike FOx-1x® resin, HSQ films contain only trace amounts of water. Thus, water content was the limiting component for the solid-phase gelation reactions, in the absence of which bases were ineffective at promoting gelation.

4.3 Deactivation of PAG in Unirradiated Areas of Direct-Write Films

During the deactivation step shown in Figure 3.4, no drop in refractive index was observed in core regions even though the bake temperature (250°C) exceeded the thermal activation point of the TTBPS-Tf PAG (see Figure 4.4). This indicated that all the photoacid had been either neutralized or volatilized; hence, there was no acid-catalyzed decomposition of polycarbonate. The thermal stability of the refractive index profile was only limited by the onset of decomposition of the neat PNC polymer, which according to the TGAs of neat PNC was about 270°C (see Figures 4.1-4.3). Hence for high thermal stability of UV-defined patterns of porosity, it was desirable to use a photodefinable porogen with as high a decomposition point as possible in the direct-write system.

4.4 Comparison of Dielectric Properties of Thermally-Induced and UV-Written Porous Films

Figure 4.12 compares the interline (synonymous to intralevel and intralayer) dielectric constants of a B-type direct-written film to their non-porous control samples for each step of the direct-write process shown in Figure 3.4. The B-type direct-written film and its control sample had PBG:PAG:PNC wt% loadings of 2:10:20 and 2:10:0, respectively.

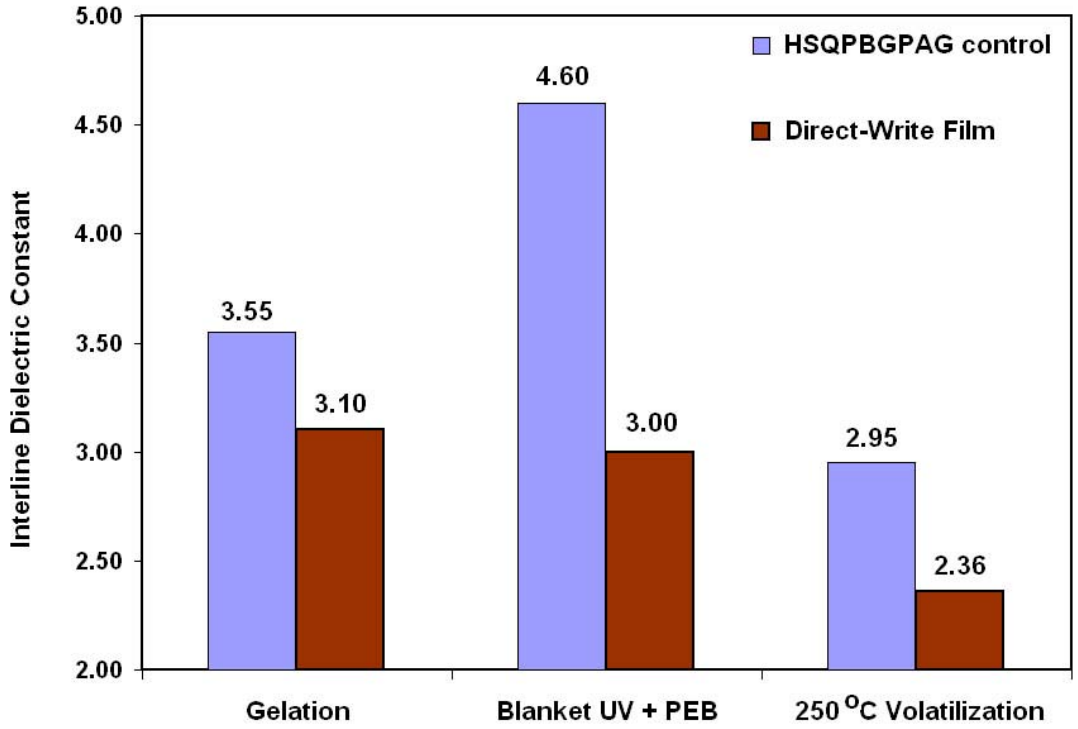

Figure 4.12 – Comparison between the intralayer dielectric constants values (at 100 kHz) of blanket irradiated direct-written and control films during processing.

After gelation, the control film had a relatively high dielectric constant compared to pure HSQ (k = 2.80) due to the effect of the PBG-released bases on the average

polarizability of the films. After gelation, the direct-write film had a slightly lower dielectric constant due to the effect of the free volume occupied by the polymer has on the polarizability of the direct-write matrix. The dielectric constant of the control sample rose dramatically owing to the large increase in polarizability that was caused by the photogeneration of acids. The dielectric constant of the direct-write film dropped slightly after UV-exposure because the porosity induced in the matrix backbone mitigated the effect of the increased polarizability from acids. The high temperature volatilization of the acids caused a decrease in the dielectric constants of both the porous and control films since the removal of polar species lowered the polarizability. The final dielectric constant of the control sample was slightly higher than HSQ (k = 2.80), probably as a result of larger film density due to catalyzed crosslinking in the previous steps.

The direct-written film exhibited a much lower dielectric constant than the control due to the induced porosity within the matrix. Porous films formed via the traditional template technique and at the same polymer loading as the direct-written film had intralayer dielectric values of 2.29 compared to a value of 2.80 for its control film. Table 4.2 shows the final values of the intralayer dielectric constants of the porous direct-written and thermally-processed films and their respective non-porous control samples.

Table 4.2 – Comparison of the final intralayer dielectric constants of porous films and their non-porous control samples at 100 kHz.

Type of Porous Film	PNC loading (wt%)	Final intralayer k of porous film	Final intralayer k of non-porous control film (0% PNC)
Direct-written (B-type)	20	2.36	2.95 (B-type)
Thermally-processed	20	2.29	2.80 (pure HSQ)

Using the Maxwell-Garnett mixing rule to compare the final the intralayer dielectric constants of the porous and non-porous films, the level of UV-induced porosity was estimated to be 21 vol% for the direct-written films and 20 vol% for the thermally-processed films. Although UV-induced porosity was formed when irradiated films were heated at 170°C, the volatilization step, which was performed at 250°C, was a necessary requirement in order to achieve a low-k value. This indicates that for low-k applications, the direct-write process is limited to substrates capable of withstanding baking temperatures of 250°C for 30 minutes. The use of PBGs and PAGs in the direct-write process also had an undesirable effect on the overall polarizability of the HSQ matrix since the intralayer dielectric constant for direct-written porous films (k = 2.36) was slightly higher than that of thermally-processed films (k = 2.29) even though the UV-induced porosity was slightly higher than the thermally-induced porosity. This is because the non-porous backbone of direct-written films (k = 2.95) have higher dielectric constant than pure HSQ (k = 2.80). This may be a result of the presence of by-products of the PAG photocleavage reactions remaining in the film after volatilization of the acid. Based on the chemical structures reported in literature, the by-products of PAG activation have permanent dipoles; hence, these species would increase to the polarization of the matrix and cause the dielectric constant to be higher than a pure HSQ film.[3]

Two scenarios would allow the final polarizability of direct-written films to be lowered even further. If an alternative matrix material could be crosslinked at low temperatures without the need for base-catalysis, then the required PAG content would be much lower since no bases would be present to partially neutralize the acid molecules. The mass ratio of PAG to polymer used in the TGA studies was only 3 wt%; thus, the

absence of PBGs in such a direct-write system would allow PAG loadings to be lowered by at least one order of magnitude. If the acid content was sufficiently low, the volatilization step may become unnecessary, hence allowing more substrates to be used for direct-write processing of low-k films. An alternate case would involve the use of PBG that released a base that is more efficient at crosslinking HSQ than the base released by N-methylnifedipine. The greater mechanical integrity would allow higher levels of UV-induced porosity to be incorporated within the direct-written matrix hence allowing lower values of the dielectric constant of the direct-written films after the volatilization step.

4.5 Comparison of Refractive Indices of Thermally-Induced and Directly-Written Porous Films

Figure 4.13 shows values of refractive index of the exposed and unexposed halves of an A-type film having PBG, PAG and PNC loadings of 5%, 10%, and 10%, respectively. The refractive index on the irradiated side dropped from 1.406 to 1.344 due to the incorporation of porosity within the matrix. In comparison, the refractive index of its control sample (abbreviated as HSQPBGPAG and having no PNC) remained at 1.379 after undergoing the same bake conditions. The refractive index values were observed to be very low even directly after the UV-exposure and PEB step because optical frequencies (~ 10^{14} Hz) are above the maximum frequencies for orientation and distortion polarization. Thus residual acid and base had a much lower influence on refractive index measurements than on dielectric constant measurements.[3, 7-9] As further evidence of this,

the refractive index values of HSQPBGPAG controls were found to be similar to pure HSQ films both after the second and third steps of the direct-write process.

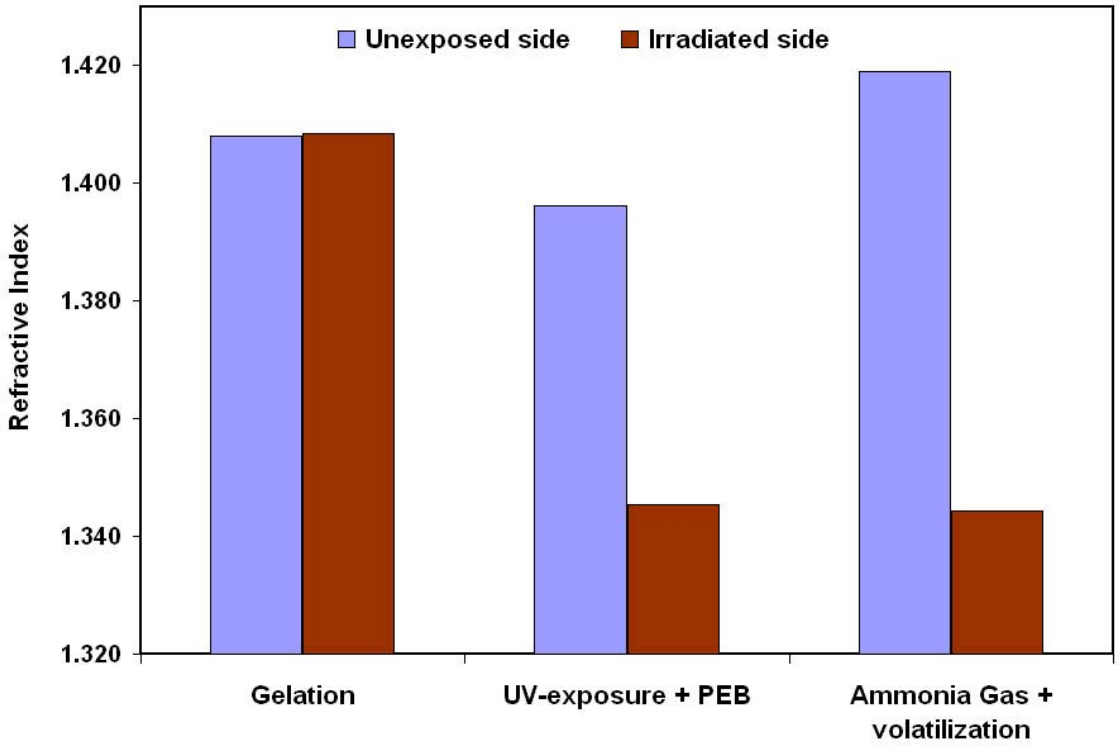

Figure 4.13 – Refractive index values on irradiated and unexposed halves of an A-type direct-write film after sequential processing steps. The PNC loading was 10 wt%.

Using the Lorentz-Lorenz refractive index mixing rule, it was estimated that air occupied about 8% of the volume in the irradiated side.[3, 7-9] The refractive index in the unexposed half of the wafer was fairly constant during the PEB because the unexposed PAG was thermally stable during the 170^{o}C bake; hence, there was the absence of acidolytic decomposition of the PNC. The slight rise in refractive index of both sides of the A-type film during the deactivation step shown in Figure 4.13 was probably due to an increase in density from film shrinkage caused by the condensation of dangling silanol

bonds during the 250°C bake. Due to the high efficiency of N-methylnifedipine PBG at crosslinking HSQ once activated, we were able to mechanically support higher levels of porosity in B-type films than the A-type films prior to pore collapse. For B-type films with PBG, PAG and PNC loadings of 2%,10%, and 20%, respectively the final refractive index on the irradiated side was 1.313 compared to a value of 1.398 for a B-type HSQPBGPAG control film (0% PNC loading).[6] Hence, for B-type films, the difference in refractive index between the porous region and a HSQPBGPAG control sample was as high as 0.085, which using of the Lorentz-Lorenz equation, indicates that the amount of porosity incorporated on the irradiated side was about 20 vol%. Thermally processed porous films with the same loading (20 wt%) had refractive index values of 1.302 compared to a value of 1.394 for a pure HSQ control that underwent the same heating procedure. The amount of thermally-induced porosity was estimated to be 21 vol% using the Lorentz-Lorenz equation. The final values of the refractive indices of both the direct-written and thermally-induced porous films and their control samples are summarized in Table 4.3.

Table 4.3 – Summarized comparison of the final refractive indices of porous films and their non-porous control samples

Type of Porous Film	PNC loading (wt%)	Final Refractive Index of porous film	Final Refractive Index of non-porous control
Direct-written (A-type)	10	1.344	1.379 (A-type)
Direct-written (B-type)	20	1.313	1.398 (B-type)
Thermally-processed	10	1.34	1.394 (pure HSQ)
Thermally-processed	20	1.302	1.394 (pure HSQ)

The final values of the refractive index of UV-induced porous films were similar to those of thermally-processed porous films of the same polymer loading and also similar to other templated films reported in literature.[21-23] The decreases in the refractive index values of the PAG/polycarbonate direct-write systems were also comparable to those of the photobleaching direct-write systems reported in literature, and the differences may be attributed to the differences in loadings levels of the decomposable polymers used.[5, 27, 103] The differences (about 1%) between levels of porosity estimated using refractive index mixing rules and those predicted by dielectric constant mixing rules are likely to be a result of uncertainties in film thickness arising from the rough surfaces of the porous films.[5, 14-16]

4.6 Comparison of Internal Pore Structure of Thermally-Induced and UV-Induced Porous Films

Figures 4.14 and 4.15 show TEM images of the microstructure of a thermally-induced porous film and UV-induced porous film, respectively. Both films had a polymer loading of 20% and, based on porosity estimates from dielectric constant mixing rules, their induced porosities were very similar (21% and 20%, respectively). It is clear by comparing the structures shown in Figures 4.14 and 4.15 that there are significant differences in the internal structure of these films. From Figure 4.14, we observe that using the traditional template technique (thermally-induced decomposition of PNC) produced closed-cell mesopores (5-10 nm in size) that were nearly spherical in shape and located in close proximity to one another (the bright, elongated 'spongy' areas are collections of mesopores).

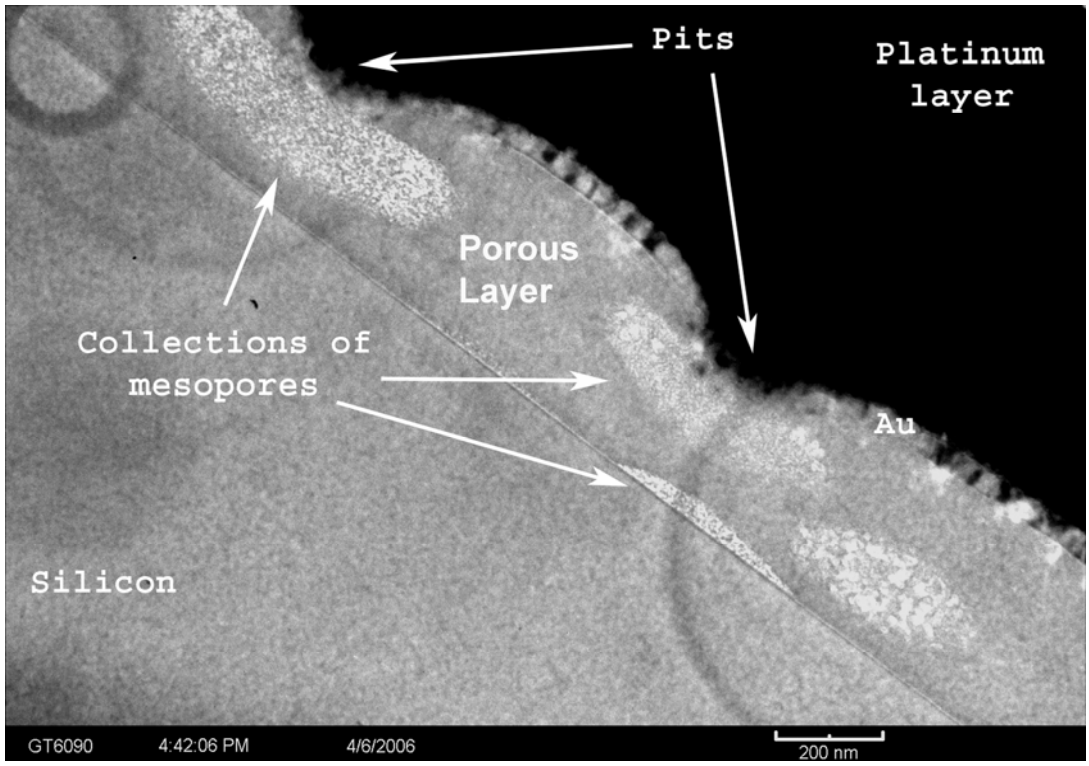

Figure 4.14 – TEM image of a thermally-processed porous film with an initial PNC loading of 20%. Length of scale bar is 200 nm

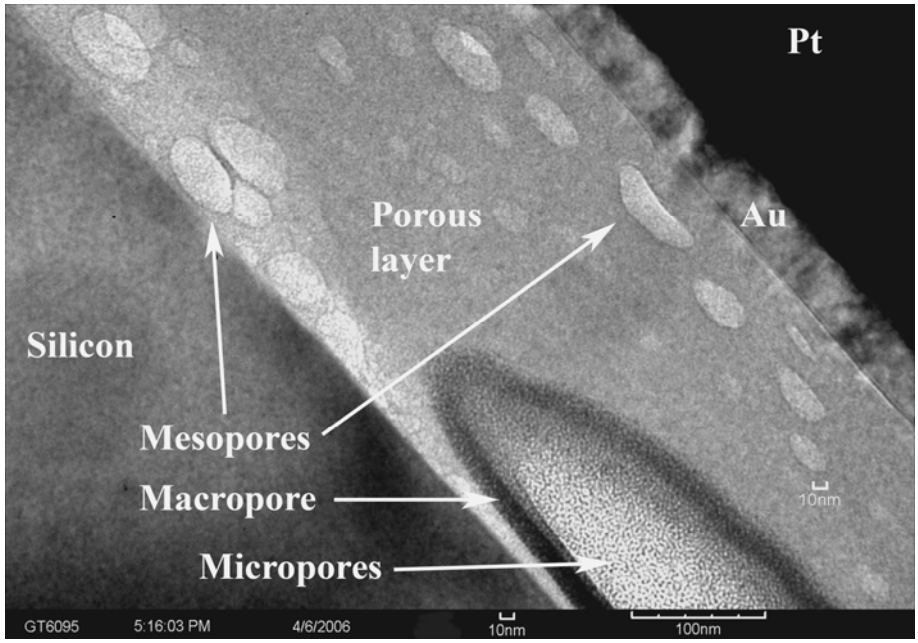

Figure 4.15 – TEM image of a B-type direct-write film with an initial PNC loading of 20% directly after the UV-decomposition step. Lengths of smaller and larger scale bars are 10 nm and 100 nm, respectively.

The agglomeration of the mesopores in large patches was likely due to phase segregation and agglomeration of polymer chains prior to decomposition, which was encouraged by the high processing temperature of the template method. As the PNC thermally decomposed, the mesopores formed in relatively close proximity to one another, and the pores may have preferentially collected as a result of internal forces acting on them. The lack of bonding groups on the backbone of PNC, **1**, negated the possibility of avoiding phase segregation via the chemical bonding of the polymer to HSQ prior to heating. [6, 14-16, 21, 22] Although the mesopores shown in Figure 4.14 were in large collections, no macropores were detected and thus complete agglomeration of polymer chains prior to decomposition did not occur.

From Figure 4.15, we observe that direct-written films contain two different sizes of UV-induced pores within the film: elongated mesopores (measuring 10 nm by about 20-30 nm), and elongated macropores (measuring 100 nm by about 200 nm in size). The intrinsic structure of HSQ contains micropores (measuring 1-2 nm size), which are visible in the lower right corner of Figure 4.15, where they are situated behind a macropore bubble that was conveniently sliced during FIB milling. Thus the micropores were not a result of PNC decomposition and are naturally present in every SOG film regardless of the type of processing it underwent. The isolated mesopores shown in Figure 4.15 were induced by the decomposition of PNC, and they were not present in large collections such as the ones shown in Figure 4.14, suggesting that processing of direct-write films below the glass transition temperature of the matrix discourages large scale movement of polymer chains prior to decomposition.

The macropore shown in Figure 4.15 is likely due to the coalescence of meso-sized air pockets after decomposition possibly as a result of rapid film shrinkage induced by acid-catalyzed condensation of residual silanol bonds generated during the gelation step. Film shrinkage would also account for the shape of the meso-sized and macro-sized pores, which all appear to be thinner in the vertical direction and wider in the lateral direction. The thermally-processed film, shown in Figure 4.14, did not contain any crosslinking agents but gradual film shrinkage may have occurred during polymer decomposition thus leading to the elongated groupings of mesopores. The TEM images of thin A-type direct-write films showed pores of similar shapes and sizes to the B-type direct-write film shown in Figure 4.15 but the amount of pores A-type films were fewer in since these films were less crosslinked and could not support more than 10% of UV-induced porosity.

4.7 Surface Morphology of Thermally-Processed and UV-Processed Films

4.7.1 Influence of Polymer Decomposition on Surface Roughness

As shown in Figure 4.16 and Figure 4.17, porous films formed via the decomposition of sacrificial polymers had significant levels of surface roughness. For direct-written films with 20% PNC loadings, the unexposed and UV-irradiated sides had rms surface roughness values of 7.3 nm and 14.5 nm respectively, while thermally-processed films of the same PNC loading had rms surface roughness values of 26 nm. The rms surface roughness values scaled with the initial PNC loading, both for UV-exposed and thermally-processed films.

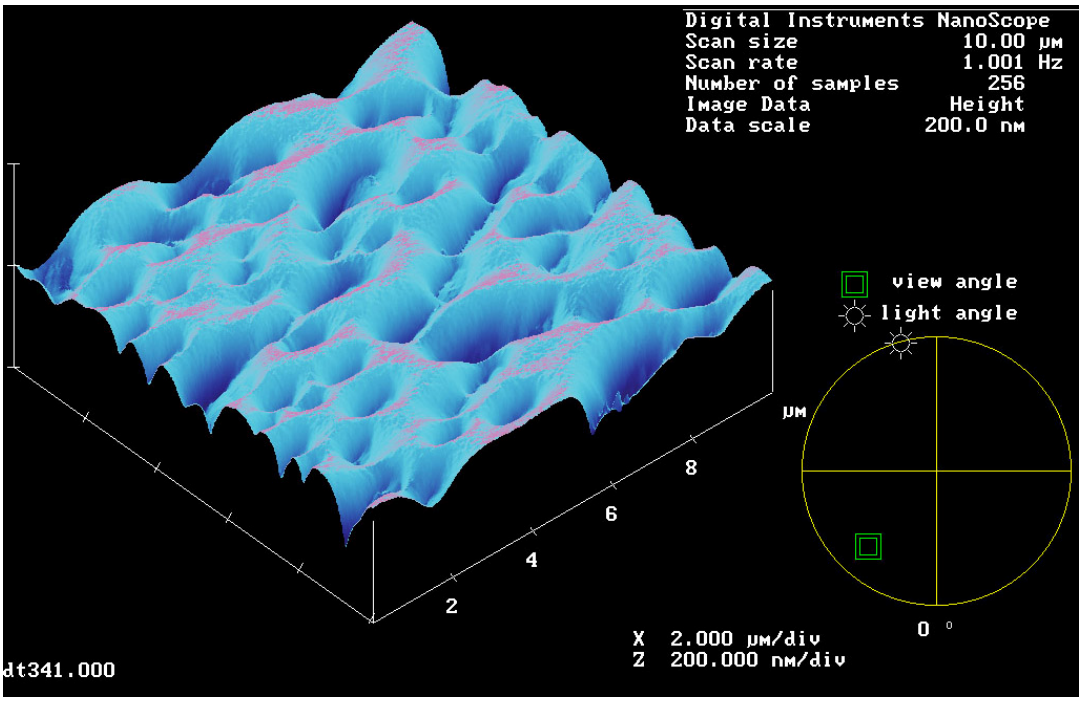

Figure 4.16 - AFM image of a thermally-processed film having a PNC loading of 20%. The rms surface roughness was 26 nm.

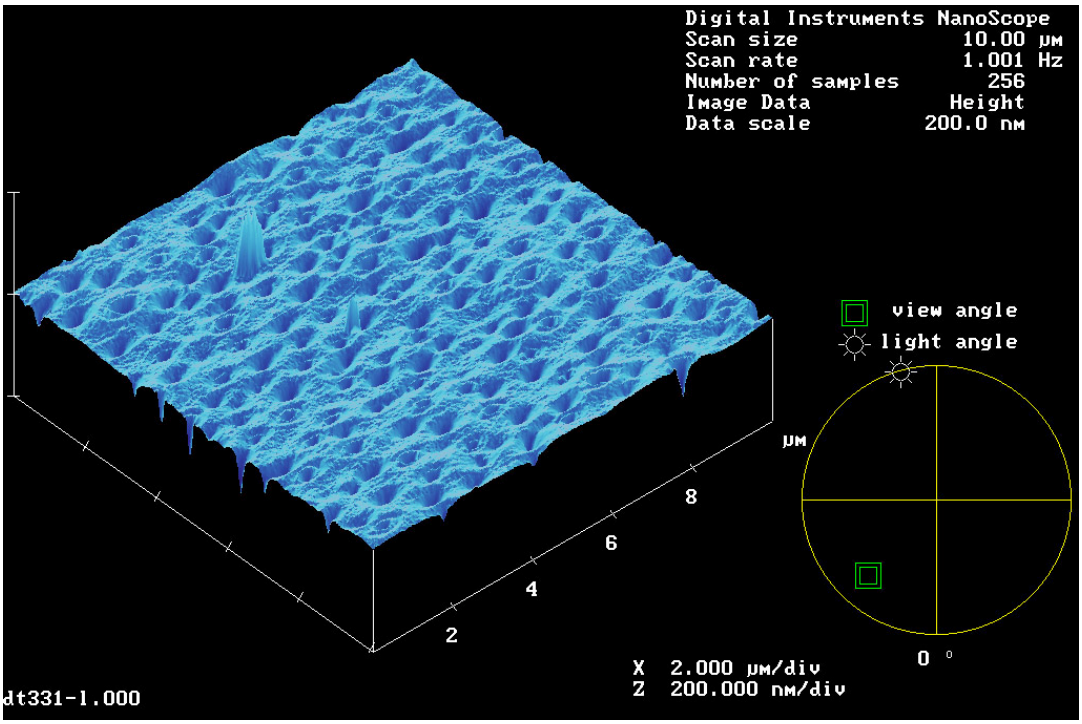

Figure 4.17 – AFM image of the irradiated side of a direct-write film having a PNC loading of 20%. The rms surface roughness was 14.5 nm.

The sizes of pits on the surface of both direct-write and thermally-processed porous films varied widely with their depths ranging from 60-150 nm and their lateral dimensions on the order of hundreds of nanometers for direct-written films and from hundreds of nanometers to 1.5 μm for thermally-processed films. Although the rms surface roughness values were observed to increase with increasing polymer loading, there did not seem to be any correlation between the polymer loading and the dimensions of the pits.

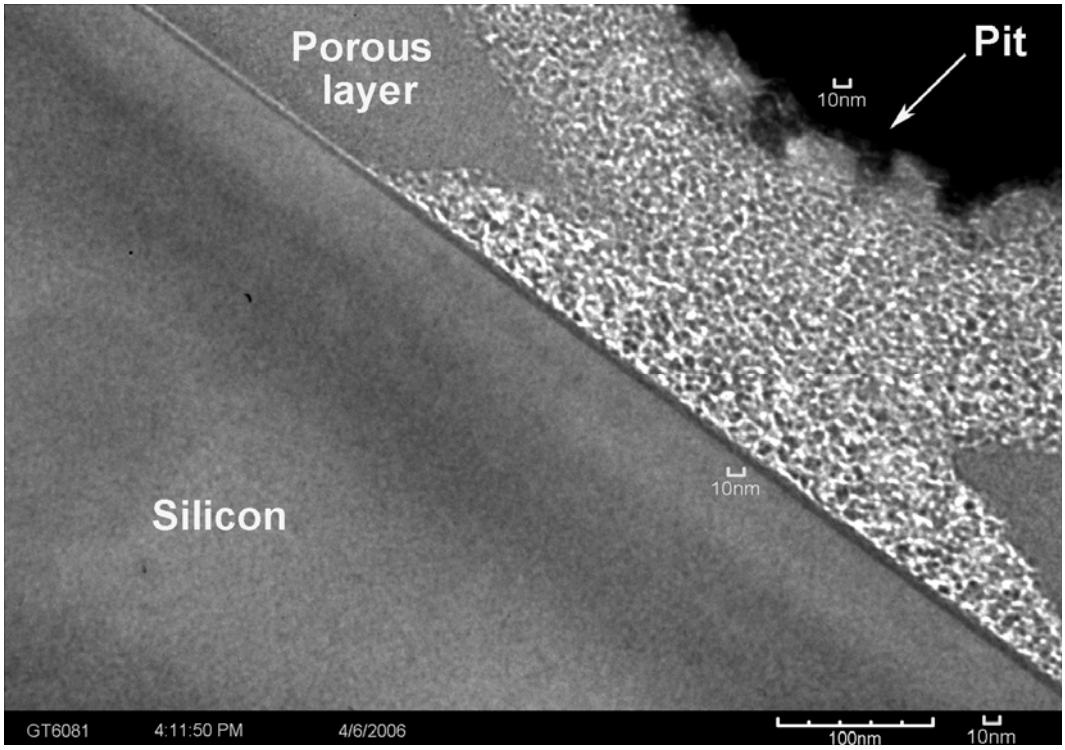

Figure 4.18 – TEM image showing the relative positions of mesoporous regions and a pit on the surface of a thermally-processed porous film with a 20% initial PNC loading. Lengths of small and large scale bars are 10 nm and 100 nm, respectively.

TEM images of thermally-processed films, such as Figure 4.14 and Figure 4.18, showed that pits were only located above the collections of mesopores that were in close

proximity to the surface of the films. This indicated that the evolution of a relatively large volume of gaseous decomposition products near the surface was the likely cause of the disruptions of the film surface. Comparisons of the lateral dimensions of the spongy patches and the pits in Figures 4.14, 4.16, and 4.18, show that the sizes of the pits in thermally-processed films were comparable to the dimensions of the porous regions in their internal structure.

TEM images, such as the one shown in Figure 4.19, showed that when the macropores of UV-exposed direct-write films were situated close to the surface of the films, depression formed directly above them, which descended into macro-sized cavities.

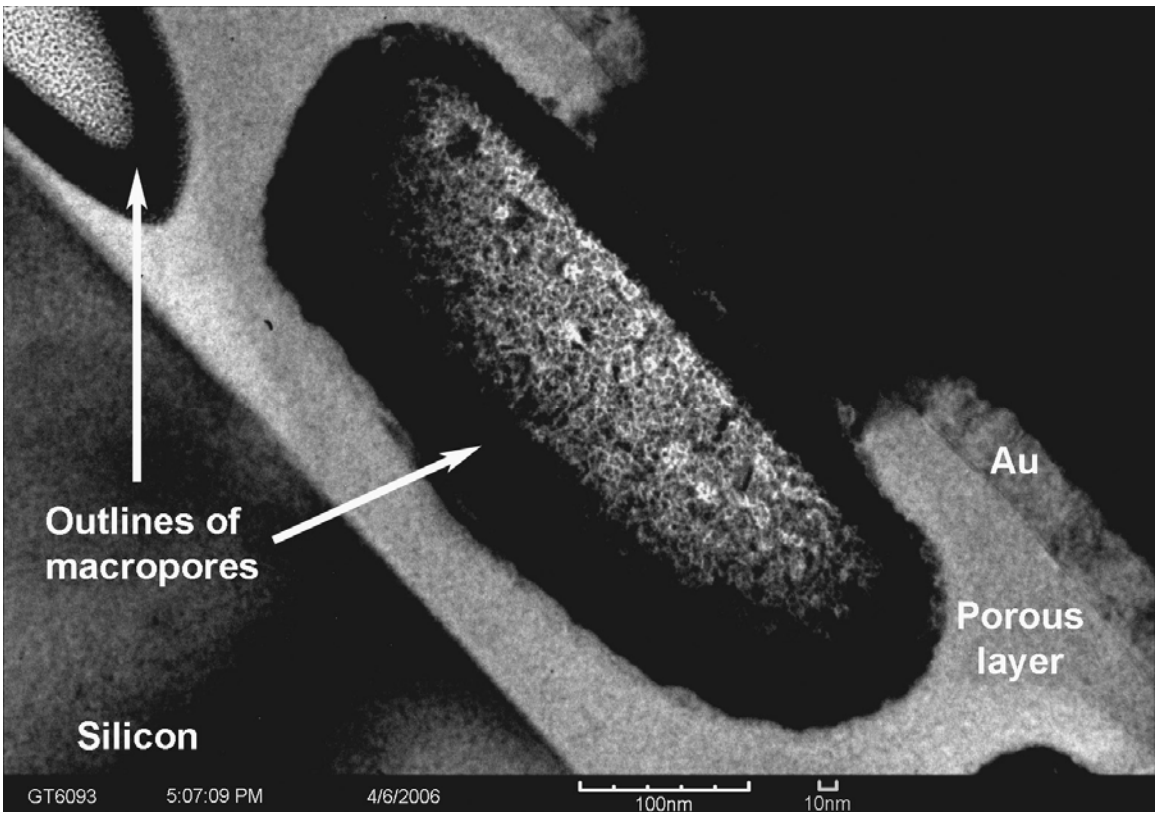

Figure 4.19 – TEM image showing a cavity produced by a macropore in a direct-written film. The sizes of the smaller and larger scale bars are 10 nm and 100 nm, respectively

This suggests that as gases were evolved during the formation of a macropores that were in close proximity to the surface, depressions were produced, which grew deeper until they eventually collapsed into macro-cavities as a result of mechanical instability. In contrast, closed macropores that were located further below the film surface did not produce pits above them, as observed in Figure 4.15. This provides further evidence that the cavities observed in the TEM images of direct-written films were produced by the collapse of the top film layer into underlying, open-celled macropores. Additionally, UV-induced mesopores, such as those shown in Figure 4.15, did not appear to influence the surface properties of the direct-write film. This suggests that the volume of gases evolved by mesopores was not sufficient to cause the large disruptions of the film surface necessary for pit formation. Thus, the location and size of pores and the overall volume of gases evolved by the decomposition of PNC were all important factors that affected the surface morphology of the porous films. The reason that the pits in AFM images of direct-written films (see Figure 4.17) did not appear as cavernous macro-cavities was due to the probing limitations of AFMs; the inner surfaces of the cavities were inaccessible to the AFM tips as they raster-scanned across the top surfaces of the UV-processed porous films.

From the TEM and AFM results, it was clear that pores were not uniformly distributed within the irradiated films and at the local level, there were large variations in both pore sizes and levels of porosity arising from the inhomogeneity within the structure of direct-written film. As a consequence, any functionality influenced by porosity (optical, dielectric, and mechanical properties) was non-uniform in nature even within blanket exposed films, and observations based on bulk material characteristics were only

crude estimates of the true characteristics of regions within these films. Since the quantitative values of induced-porosity calculated using Lorentz-Lorenz and Maxwell-Garnett mixing rules assumed that air was well mixed with the matrix within the films (ie. film homogeneity), they only provided estimates of the average properties of the films and are not strictly valid for determining actual levels of porosity at specific locations.

Additionally, light scattering that was induced by the rough surfaces of porous films adversely affected their refractive index measurements since ellipsometry calculations are based on the assumption that interfaces are smooth. The influence of roughness on the characterization of dielectric constant was less pronounced than the influence on optical measurements because the average film thicknesses (280-430 nm) of the films that were coated onto the IDEs were much larger than the values of rms roughness values (14-26 nm) of the porous films. For this reason, the porosity estimates based on the dielectric constant data are more reliable than those calculated using optical data. However, the porosities estimated by refractive index and dielectric constant mixing rules were observed to be in close agreement, and they were comparable to those reported in literature for similar sacrificial polymer loadings.[85, 87, 88, 98-100]

4.7.2 Influence of Polymer Mobility on Surface Roughness

From the TEM results shown in Figure 4.14 and 4.15 it can be inferred that the lower surface roughness of direct-written films in comparison to thermally-induced porosity may have been due to the lower tendency for the polymer to phase segregate in the glassy-state than in the rubbery-state of the matrix. To test this hypothesis, spun-

coated HSQ-PNC films were extensively crosslinked at room temperature using saturated ammonia vapor prior to thermal decomposition of the PNC similar to other thermally-processed films. Table 4.4 and Figure 4.20 indicate that these pre-gelled thermally-processed films had surfaces that were much smoother (rms roughness of 7.9-11.1 nm) than their high-temperature cured counterparts (rms roughness of 26 nm), and slightly smoother than the direct-written films (rms roughness of 14.5 nm). The AFM measurements were done multiple times on each sample to ensure that the results were statistically significant.

Table 4.4 – Comparison of the surface properties of porous films that underwent different processing conditions above and below T_g of HSQ. All films had PNC loadings of 20%

Crosslinking Method	Crosslinking temperature (^oC)	Method of PNC decomposition	Decomposition temperature (^oC)	rms surface roughness (nm)
Gelation (Photobase)	170	Direct-write	170	14.5
Thermal	270	Thermal	325	26
Gelation (30 min ammonia vapor)	25	Thermal	325	11.1
Gelation (10 min ammonia vapor)	25	Thermal	325	7.9

The room temperature ammonia treatments resulted in the glass-state gelation of HSQ, as described earlier, effectively crosslinking HSQ at temperatures for which PNC mobility was very low. When the ammonia-gelled films were then heated to 325^{o}C during the thermal decomposition step, the final surface roughness values were relatively low and comparable to the direct-written films. During the glassy-state crosslinking, the

extent of phase segregation of PNC was lower than thermally-crosslinked films, which were cured in the rubbery state (270^{o}C). The reduction in PNC phase segregation in UV-processed films hindered the formation of large collections of closely-spaced mesopores, hence reducing the tendency for pit formation on their film surfaces. The reduction in pit formation resulted in low surface roughness values compared to high-temperature processed films, as clearly seen in Table 4.4.

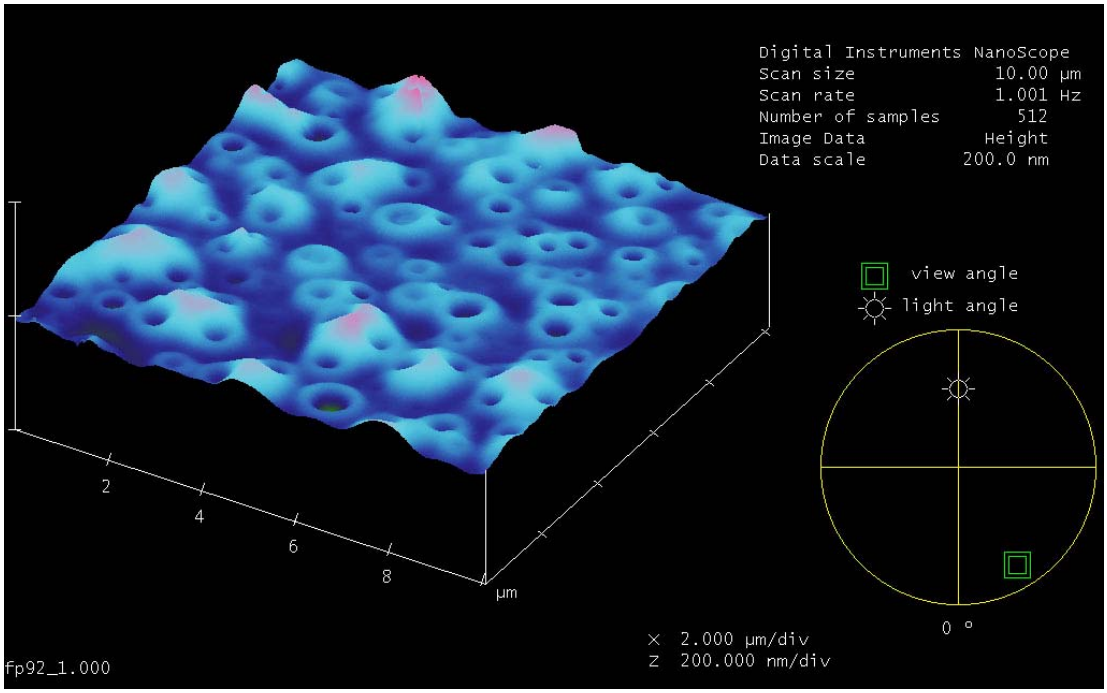

Figure 4.20 - AFM image of a porous film that was gelled at ambient for 30 minutes using ammonia gas before thermal-decomposition of PNC. The PNC loading was 20% and the resultant porous film had an rms roughness of 11.1 nm.

The ammonia-gelled porous films had smoother surfaces than the direct-written porous films of the same polymer loading because their ammonia treatments produced a greater extent of crosslinking of HSQ than that induced by the photobases used in the direct-write process. HSQ films gelled for 10 and 30 minutes using ammonia gas were

had E_r values of 6.4 GPa and 9.4 GPa, respectively. HSQ films gelled using photobases (loadings similar to direct-write formulations) had E_r values of about 5.8 GPa. Thus, even though the ammonia-treated films were exposed to much higher temperatures during their decomposition step than the direct-written films, the average polymer mobility in the ammonia pre-treated thermally-porous films was lower than in UV-processed films. From this we can conclude that the physical condition during crosslinking was the dominant factor influencing the surface morphology of porous films. This is because it greatly affected the extent of polymer movement prior to decomposition and subsequent pore formation; thus, it determined the final internal morphology of the porous films.

In the ideal case, the gelation step of the direct-write process would produce such a high degree of crosslinking that the sacrificial polymer would be essentially frozen in place while at the same time displaying minimal film shrinkage in order to avoid deforming and coalescing adjacent pores. Such a scenario would produce smooth porous films free of macropores and free of phase segregated mesopores. It was not clear why the rms roughness of the 30 min gelled film was larger than the 10 min gelled film, since the greater extent of crosslinking within the former film should have reduced the extent of polymer migration at high temperatures in comparison to the latter sample. It is expected that future TEM analyses of the microstructure of pre-gelled thermally processed films should provide insight in understanding these AFM results. Nevertheless, the differences in roughness in between thermally processed films that were crosslinked $<T_g$ of HSQ and those crosslinked $>T_g$ of HSQ are statistically significant, and the AFM results provide further evidence that a reduction in polymer

mobility prior to decomposition results in smoother porous films once decomposition has taken place.

4.7.3 Influence of Surface Roughness on Light Scattering from Porous Layers

The effects of rough surfaces on light scattering have been widely investigated by researchers, and it has been established that the degree of scattering of a coherent beam of incident light increases as the dimensions of the surface deformities and/or degree of surface roughness increases.[118-120] It was experimentally observed that the direct-written and the thermally-processed porous films had a hazy appearance, which was not observed in non-porous control films. This haziness appeared to increase with the initial PNC loading of the porous films. It is believed that this haziness was a manifestation of the degree of roughness-induced light scattering arising from the large degree of scattering caused the lateral pit dimensions being on the same order of magnitude as the wavelengths of visible light. Since AFM studies showed that the rms values of surface roughness increased with the initial polymer loading and the lack of influence of polymer loading on the dimensions of the pits, the increase in haziness was due to increased roughness the porous films. Owing to light scattering, the reflected light detected by the ellipsometer was no longer coherent; hence, it adversely affected the ellipsometry measurements by increasing the uncertainty of the refractive index values and the porosity values estimated using them.

The influence of roughness on the characterization of dielectric constant was less pronounced than the influence on optical measurements because the average film thicknesses (280-430 nm) of the films that were coated onto the IDEs were much larger

than the values of rms roughness (14-26 nm) of the porous films, and the uncertainty induced in modeling the IDEs was relatively small. For this reason, the porosity estimates based on the dielectric constant data were more reliable than that calculated using optical data.

CHAPTER 5: PROPERTIES OF SOLVENT-INDUCED POROUS FILMS

5.1 Gelation of HSQ by Non-protic Polar Organic Solvents

5.1.1 Influence of Solvent Polarity on Gelation Time of FOx-1x Resin

Uncontaminated FOx-1x resin remain stable as a liquid solution in plastic vials for over a year at ambient conditions. However, when samples of FOx-1x resin were mixed with polar non-protic organic solvents at ambient temperature, these mixtures were observed to spontaneously solidify into insoluble gels within seconds to weeks depending on the polar solvents used. To ensure a fair comparison between the influences of each of the solvents, the solvents were chosen to ensure that they were all hydrophilic, capable of hydrogen bonding with the silane bonds in HSQ, and completely miscible with the resin's MIBK solvent, thus avoiding complications arising from differences related to phase equilibria.[118-120] As shown in Table 5.1, the time taken for gelation to occur depended largely on the polarity of the solvents; the solvents with stronger permanent dipoles, such as Propylene Carbonate (PC), were capable of gelling the HSQ resin within a matter or seconds whereas weakly polar solvents, such as Tetrahydrofuran (THF), took several days to gel HSQ under similar conditions.

Although MIBK deviated from the trend, in general it was observed that solvents with stronger dipole moments were more effective gelation catalysts than weakly polar solvents.[118-120] Researchers have shown that polar solvents are able to form of temporary bonds with silanes resulting in the formation of a reactive transition state. The silicon atoms act as electropositive centers in the transition state, which makes them vulnerable to nucleophilic attack by trace water molecules present in the FOx-1x/polar

solvent mixtures. Thus, water molecules displace the solvents to form a hydrated, second transition state similar to the S_ni-Si mechanism discussed earlier (refer to Figure 4.5). As shown in Figure 4.5, the rearrangement of the hydrated transition states result in the formation of a silanol bonds, which facilitate sol-gel condensation reactions.

Table 5.1 – Gelation times of FOx-1x resin with various non-protic polar solvents

solvent	Literature values of permanent dipole moment [118, 119]	Approximate gelation time of mixtures
THF	1.75	1 week
MIBK	2.66	one month
Acetone	2.69-2.88	1 week
NMP	4.1	5 hrs
GBL	4.27	30-60 min
PC	4.91-4.94	3-4 seconds

Transmission-mode FTIR studies that were performed on FOx-1x liquid samples before and after mixing with polar solvents confirmed that during solvent-induced gelation silanol bonds were formed as silane bonds were gradually depleted and that no permanent bonds were formed between HSQ and the organic solvents. Similar to base-catalyzed gelation, FTIR studies also showed that solvent-induced gelation also results in the reduction of the cage/network ratio (ratio of areas underneath the FTIR stretch peaks corresponding to cage-type and network-type siloxane bonds in HSQ).

5.1.2 Influence of Solvent Penetration on Gelation of HSQ Films

FTIR-ATR data showed that HSQ films that were soaked in polar solvents showed large decreases in the c/n ratio of HSQ from 1.58-1.61 for as-spun films to c/n values below 1.00. However, unlike HSQ films that were gelled using ammonia or photogenerated bases (see Figure 4.8), no trend was observed between the c/n ratio of solvent-soaked HSQ films and their mechanical properties, as displayed in Figure 5.1.

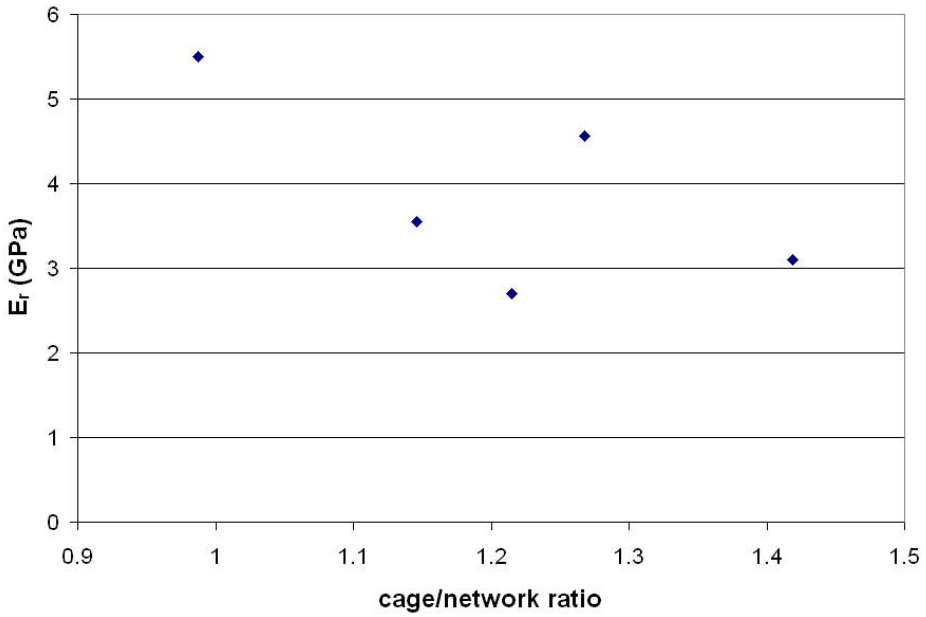

Figure 5.1 – Plot comparing data from FTIR-ATR and nanoindentation analyses of HSQ films soaked in high polar organic solvents

At first glance, the chemical and mechanical data of the solvent-gelled films appeared to contradict each other in that rigidity did not necessarily increase as the degree of network formation increased. However, it was recognized that FTIR-ATR was only able to probe the top layer of films (i.e. the bonds on the surface) due to evanescent decay of the IR beam in the ATR mode, whereas nanoindentation characterized the bulk

mechanical properties of each indented film. Thus, the combined FTIR-ATR and nanoindentation results implied that the ability of polar solvents to crosslink the entire structure of dipped HSQ films was highly dependent on their ability to penetrate and gain access to the inner parts of the films. Thus, when spun-coated HSQ films were dipped into dishes filled with polar solvents, only the surface HSQ bonds were hydrolyzed. However, the underlying parts of the HSQ films were not crosslinked, otherwise this would have led to bulk-scale effects on the mechanical properties of the films (typified by observed increases in E_r during nanoindentation).

Further evidence of the inability of PC and other highly polar solvent to penetrate the soaked HSQ films was provided by ellipsometry. When soaked films were later baked to volatilize any entrapped solvents, the refractive index of these films remained constant at 1.39, which was the same value as the initial refractive index of the pure non-porous HSQ control films. Since the formation of porosity would have decreased the refractive index of the processed HSQ films, the ellipsometry data indicated that no porosity was induced during baking and conversely that there was a negligible amount of solvent penetration (i.e. the only solvent that was removed was the residual solvent on the surface of the films).

Although the strongest polar organic solvents shown in Table 5.1 (NMP, GBL, PC) were effective gelation catalyst when mixed well with HSQ in the liquid-phase, they were unable to fully crosslink HSQ films except on the film/solvent interface. Due to the strong dipoles and hydrogen bonds in NMP, GBL, PC, these solvents had very strong intermolecular interactions that resulted in high viscosities.[118, 119] As a result of high viscosities, these fluids were poor swelling agents since there ability to seep into HSQ

was limited.[138] An additional factor of low penetration of these solvents was their high efficiency at catalyzing gelation of HSQ within short gelation times. Upon contacting HSQ films with these solvents, the top layer of the films became crosslinked on a much shorter timescale than the time taken for the viscous solvents to seep into the inner film structure. The rapid crosslinking of the HSQ surface by the viscous and strongly polar solvents effectively created a barrier to further permeation of the solvents into the inner structure of the HSQ films. Although the surface of the films were gelled (as shown by the FTIR-ATR data), the bulk of the films remained fairly soft (as indicated by the nanoindentation data).

When solvents of lower polarity (THF, MIBK, and Acetone) were used as the soaking media, the HSQ films were completely removed within seconds. This occurred because these solvents were excellent swelling agents for HSQ, and the timescale taken to swell and completely dissolve HSQ films was much shorter than the time taken to fully crosslink the matrix into an insoluble, rigid structure. No solvent was found that could satisfy all the following criteria simultaneously: effectively serving as a good swelling agent for HSQ films while also serving as a good gelation agent to catalyze the crosslinking of the entire film structure, and not dissolving the films.

5.2 Gelation and Solvent-Induced Porosity via PC/MIBK Mixtures

5.2.2 Influence of Soak Temperature on Gelation of HSQ Films

Since the development of a solvent-induced porosity process required that the entire matrix structure be crosslinked prior to solvent removal (otherwise pores would collapse due to the surface tension effects), a good swelling agent for HSQ was used as a

co-solvent to allow the highly polar solvents to penetrate the HSQ films and initiate gelation throughout the matrix. MIBK was found to satisfy the criteria for the swelling agent co-solvent while PC, which was shown earlier (refer to Table 5.1) to be an extremely effective gelation agent, was the second co-solvent in the two-component solution. Since MIBK and PC were perfectly miscible and also hydrophilic, PC/MIBK formed a single phase even when mixed with the trace amounts of water molecules present in the HSQ films.[89] Thus these PC/MIBK solutions were used both as gelation catalysts and as pore-generators in solvent-processed porous HSQ films.

When FTIR analyses were performed on HSQ films that were soaked in PC/MIBK in pre-heated ovens at different temperatures then dried using a nitrogen spray, it was observed that the degree of gelation of HSQ increased as the soak temperature was increased, as shown qualitatively in Figure 5.2 and quantitatively in Table 5.2.

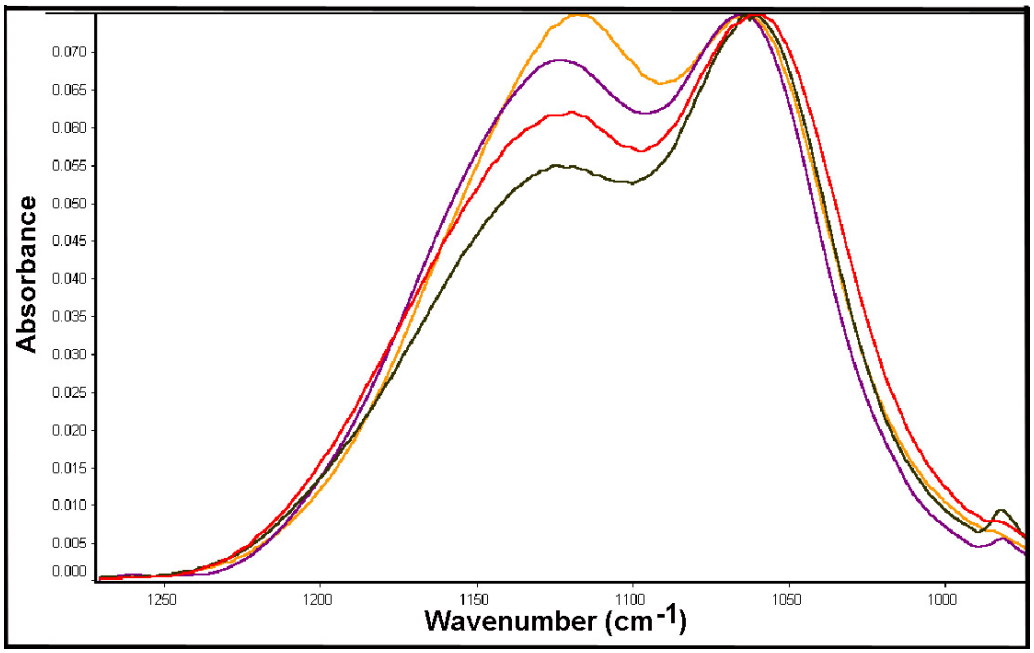

Figure 5.2 – FTIR data showing influence of soak temperature on PC/MIBK-induced gelation. Temperatures are 25°C (yellow), 60°C (purple), 75°C (red), 100°C (black).

Table 5.2 – Comparison of c/n ratios of HSQ films soaked at different temperatures for 20 minutes

Soak Temp (^{o}C)	c/n ratio
N/A (as spun film)	1.58-1.60
25^{o}C	1.32
60^{o}C	1.24
75^{o}C	1.00
100^{o}C	0.81

As the soak temperatures increased, the viscosity of PC/MIBK decreased allowing these co-solvents mixtures to seep into the inner layers of HSQ more easily and thus catalyze crosslinking of HSQ more effectively. Ellipsometry was used to confirm that PC/MIBK co-solvents were effectively penetrating the inner layers of soaked films. When soaked films were later baked to volatilize any entrapped solvents, the refractive index of these films dropped from 1.39 to 1.26-1.30 depending on the physical conditions of the soak and bake steps. These large drops in refractive index values of processed HSQ films signified that porosity was induced during solvent removal, thus proving that the PC/MIBK mixtures effectively penetrated the HSQ films and served both as gelation catalysts and pore-generators. The effect of processing temperature on the final porosity of solvent-processed HSQ films is discussed in greater detail in the following section.

5.2.2 Influence of Bake Temperature on Gelation and Porosity of HSQ Films

5.2.2.1 Influence of Temperature on Degree of Crosslinking and Porosity (in the absence of residual PC/MIBK)

HSQ films that were previously soaked in PC/MIBK at 100^{o}C were subsequently baked on hotplates for 30 minutes at temperatures ranging from 125^{o}C to 150^{o}C. As

shown in Table 5.3, FTIR analyses of these samples indicated that the c/n ratio of HSQ steadily decreased as the bake temperature was increased. Thus, higher bake temperatures favored more crosslinking of HSQ since low c/n ratios indicate higher degree of crosslinking. This may be due to high temperatures encouraging the condensation of residual silanol bonds that remained after the PC/MIBK soak step. The condensation of residual silanol bonds into siloxane bonds would result in greater crosslinking of HSQ and the lowering of the c/n ratios, since the FTIR peaks due to network-type siloxane would increase.

From Table 5.3 it is observed that as the bake temperature increased, the refractive index dropped and the solvent-induced porosity values estimated from the Lorentz-Lorenz equation increased. Hence, high bake temperatures encouraged both the gelation of HSQ and the volatilization of entrapped solvents. Since the increased crosslinking allowed the host matrix to mechanically support higher levels of induced porosity without pore collapse, high bake temperatures favored the formation of high levels of solvent-induced porosity within the HSQ films.

Table 5.3 – Comparison of the properties of as-spun films and solvent-processed films that were baked at different temperatures (soak temperature for all films was 100^{o}C)

Bake temperature (^{o}C)	c/n ratio	Final Refractive Index	Porosity estimated by Lorentz-Lorenz equation
N/A (as spun film)	1.58-1.60	1.39	N/A
120	1.05	1.29-1.30	21-25%
130	0.97	1.27-1.28	28-29%
145	0.87	1.27	29%
150	0.84	1.26	30%

When the levels of solvent-induced porosity in Table 5.3 are compared with those of porous films that relied on decomposition of PNC, it is observed that the levels of porosity were much higher than both thermally-induced and direct-written films. The lowest refractive index achieved using direct-written and thermally induced processing was about 1.30, corresponding to induced porosities of about 20-21 vol% for an initial PNC loading of 20%. PC/MIBK co-solvent processing achieved refractive indices as low as 1.26, corresponding to induced porosities of 30 vol%. Similar to direct-write processing, the solvent-induced porosity technique was performed at temperatures corresponding to the glassy-regime of HSQ; thus, high porosity levels did not require high processing temperatures.

5.2.2.2 Influence of Residual PC/MIBK on Degree of Crosslinking

The detection of FTIR peaks corresponding to carbonyl bonds (centered at about 1780 cm^{-1}), was used as a confirmation of the presence of residual solvent molecules within solvent-processed films since these bonds were present in both PC and MIBK molecules. As observed in Table 5.4 and Figure 5.3, the presence of residual polar solvents resulted in high degrees of crosslinking (typified by low c/n ratios). The results in Table 5.4 and Figure 5.3 indicated that the presence of residual PC/MIBK throughout lower temperature bake conditions was more effective at crosslinking HSQ than using only higher temperature bake conditions in the absence of residual solvents. Since the PC/MIBK co-solvents acted as gelation catalysts, the presence of residual solvents during the bake steps ensured that the rate of crosslinking of HSQ remained high, even at relatively low bake temperatures.

Table 5.4 – Tabulated data showing relative influences of residual PC/MIBK and processing temperatures on the degree of crosslinking of HSQ films

Soak Temperature	Bake temperature (°C)	Residual solvent peak detected?	c/n ratio
100	105	**Yes**	**0.66**
	120	No	1.05
	130	No	0.97
	145	No	0.87
	150	No	0.84
120	125	**Yes**	**0.55**
	150	No	0.58

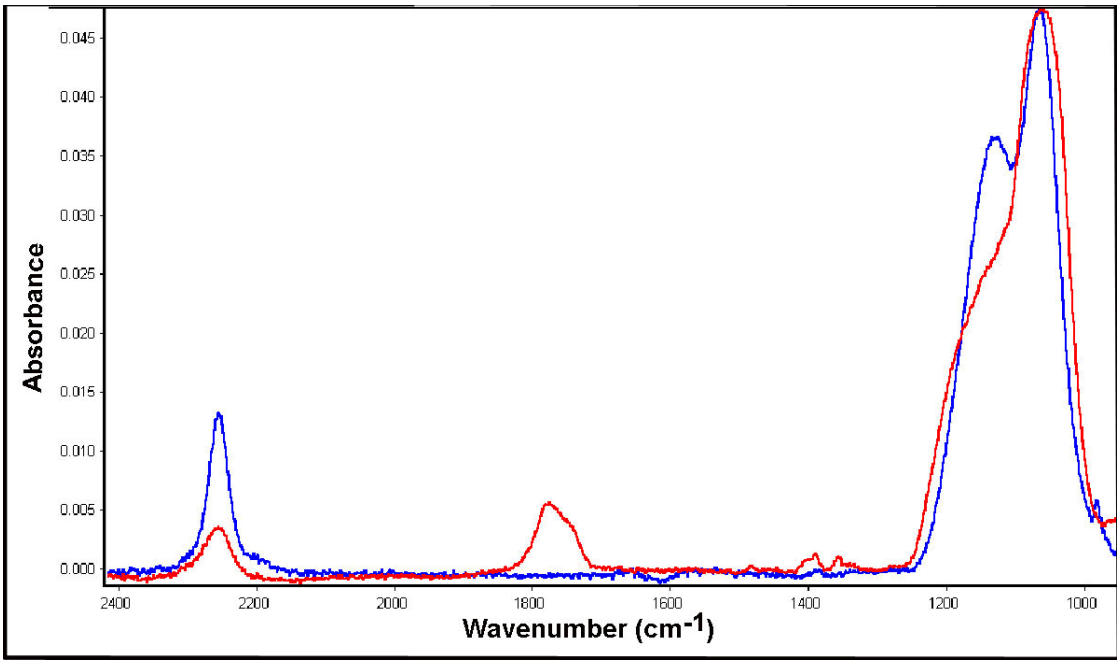

Figure 5.3 – Comparison of FTIR spectra of HSQ films baked at 105°C (red) and 145°C (blue). Both were previously soaked in PC/MIBK at 100°C.

The results in Table 5.4 also indicated that higher soak temperatures encouraged greater crosslinking, but it was observed that the increase in gelation came at the expense of having to use much higher bake temperatures to ensure complete removal of the solvents. A 150°C bake temperature was needed to volatilize all solvents after a 120°C

soak whereas 120°C was a sufficiently high temperature to remove all solvents when the soak temperature was 100°C. Although films with residual solvents entrapped in their structure were highly crosslinked, and thus able to mechanically support large amounts of porosity, the difficulty of removing residual solvents from such highly crosslinked films resulted in the inability to form pores. It was observed that films with residual solvents remained non-porous and had high refractive index values (1.39-1.41) due to the effect of polar solvents on the overall polarizability of the matrices. Since high refractive index values were undesirable for optical applications, soak and bake temperatures were carefully chosen to avoid residual PC/MIBK during solvent-processing of the porous undercladding layers shown in Figure 3.6.

5.3 Surface Morphology of Solvent-Induced Porous HSQ Films

As shown in Figure 5.4, AFM studies showed that solvent-processed porous films had relatively smooth surfaces compared to the porous films that were produced as a result of PNC decomposition (see Figures 4.16, 4.17, and 4.19). AFM scans of solvent-induced porous films did not show any evidence of pit formation or other large-scale surface defects, and their rms roughness values ranged from 2.7 nm to 3.3 nm. Haziness was not detected during visual inspection of these films, which agreed with the hypothesis that the haziness of thermally-induced and UV-induced porous films was due to light scattering from their rough surfaces. Using the knowledge gained from the combination of TEM and AFM studies of the porous films that were discussed in the previous chapter, it is expected that the solvent-processed films lacked macro-sized pores and macro-sized porous patches of phase-segregation of mesopores, since both

phenomena would have resulted in deformations of the film surfaces. Since the solvent-induced pores were not macro-sized nor closely spaced, Rayleigh scattering effects would be minimal for these films. Hence, they may be potential materials for optical application. However, further studies, including TEM analyses, are needed to confirm that this is the case.

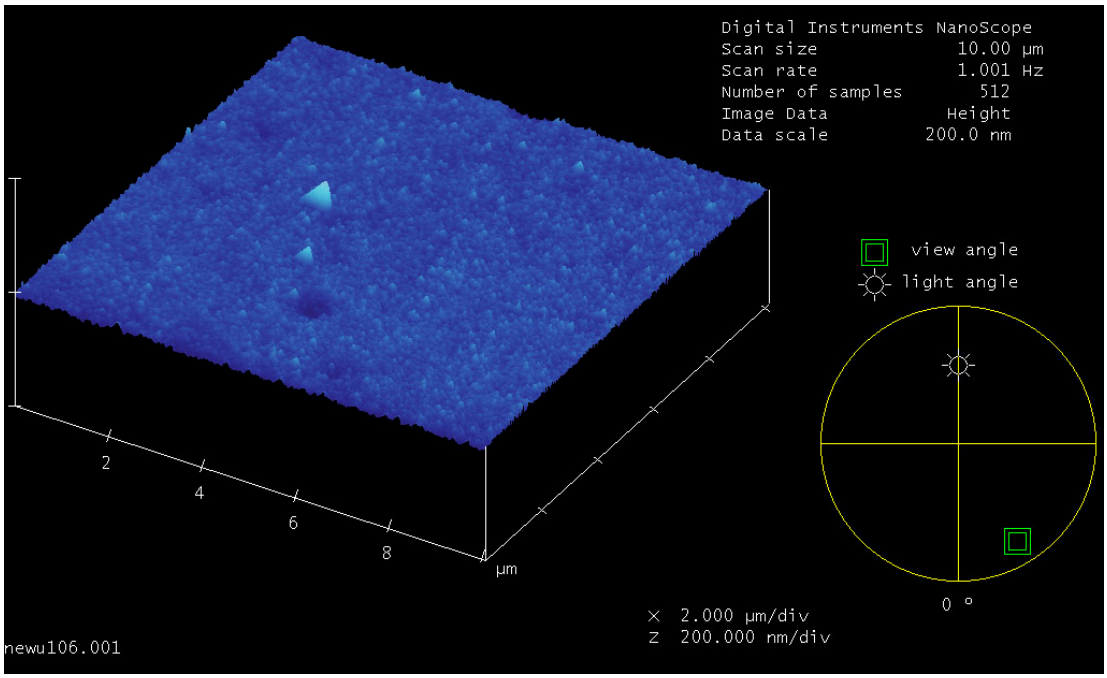

Figure 5.4 – AFM image of surface of a solvent-induced porous films. The rms roughness was 2.7 nm

The reason for the lack of macropores and large patches of mesopores may be due to a combination of factors. Since the solvents were perfectly miscible with HSQ there may have been lower tendency for the solvent molecules to phase-segregate from the HSQ skeleton than for PNC chains and thus the solvent-induced pores were not located in large collections. Additionally, both the crosslinking of HSQ and the baking of the

solvents were performed in the glassy regime, in which the mobility of the solvent-porogen would have been low and thus phase-segregation was unfavorable. Rapid solvent volatilization from the thin films discouraged the agglomeration of solvents prior to pore formation, thus ensuring that the pores that were generated remained small in size (i.e. no macropores).

In summary, the process of penetrating a spun film with co-solvents, which had the dual-functionality of serving both as gelation agents and as pore-generators was a fairly simple technique in comparison to some of the other techniques cited in literature. Unlike the processing of porous silica, the PC/MIBK process did not require tight control of multiple physiochemical conditions (pH, temperature, water content, alcohol content, etc).[52-55] Additionally, the polar solvent-processing did not need aggressive processing conditions, such as the supercritical drying requirement for producing aerogels..[52] The amount of induced porosity and subsequent film properties were a function of temperature, with porosities as high as 30% and refractive indices as low as 1.26 achieved at optimal process conditions.

Due to their low refractive index values and smooth surfaces, solvent-processed porous films were selected to be the lower cladding layers for the fabricated waveguides, which are discussed in the following chapter of the thesis. However, due to the need to confine light both laterally and vertically within the guiding layers of the waveguides, it was necessary to incorporate patterned direct-write layers in order to form lateral refractive index profiles within the waveguide structures.

CHAPTER 6: PROPERTIES OF DIRECTLY-WRITTEN TYPE I AND TYPE II POROUS WAVEGUIDES

6.1 Cutoff Thicknesses of Guiding Layers

According to ellipsometry data, the final refractive indices (at a wavelength of 632 nm) the solvent-processed layers ranged from 1.26-1.31, depending on the physical conditions used in the processing of the solvent-induced porous film. From sample to sample, the refractive indices of the cured HSQ layers and PECVD-deposited SiO2 layers were observed to remain fairly consistent at about 1.39 and 1.46, respectively. Depending on the PNC loading in the direct-write layer the refractive index values of the non-porous and porous regions of the direct-write layers ranged from 1.41-1.42, and 1.35-1.37, respectively. By substituting the typical values of experimentally measured refractive indices of each layer into equations (3.5) and (3.6), the cutoff thicknesses of the direct-write guiding layers of type I waveguides were calculated, as shown in Table 6.1. Since the $n_c > n_s$ in type II waveguides, n_s was replaced by n_c in the denominators of equations (3.5) and (3.6) when calculating the cutoff thicknesses of the SiO_2 guiding layers in type II waveguides.

Table 6.1 – Calculated cutoff thicknesses of first two modes in type I and type II slab waveguides for light propagating with a wavelength of 632 nm

Waveguide type	n_s	n_c	n_f	a_{TE}	$\tan^{-1}(\sqrt{a_{TE}})$	h_∞ (measured in μm)	
						$\nu = 0$ (1st mode)	$\nu = 1$ (2nd mode)
Type I	1.39	1.00	1.42	11.06	1.28	0.443	1.531
Type I	1.39	1.00	1.41	16.64	1.33	0.566	1.901
Type II	1.30	1.42	1.46	2.83	1.03	0.307	1.238
Type II	1.30	1.41	1.46	2.08	0.96	0.256	1.090
Type II	1.26	1.41	1.46	2.79	1.03	0.274	1.108

As observed from Table 6.1, cutoff thicknesses were low when the asymmetric parameter values were low (i.e. $h_\infty \rightarrow 0$ as $a_{TE} \rightarrow 0$). This was due to the refractive index profiles approaching that of symmetric waveguides, which have cutoff thickness values of zero. The asymmetric parameter values were low when the refractive indices of the cover and substrate layers were similar and also when $n_f >> (n_c, n_s)$. Thus type II waveguides had lower a_{TE} values and lower cutoff thicknesses than type I waveguides, since the differences between the refractive indices of the cores of type II waveguides and their respective adjacent layers were larger than the differences in type I waveguides. As stated earlier, the guiding layers in all fabricated waveguides were made thick enough to support the mode propagation.

6.2 Effective Indices and Propagation Constants of Guided Modes in Type I and Type II Waveguides

Figures 6.2 and 6.3 show experimentally measured thicknesses and refractive indices, which were typical for type I and type II waveguides, respectively. Table 6.2 summarizes the calculated values for the number of modes supported, along with the effective indices (N_{eff}) of core regions and propagation constants (β) corresponding to each of the guided modes supported by the waveguide structures shown in Figures 6.2 and 6.3 Similar to the results in Table 6.2, numerical models of numerous variations of the type I and II layouts consistently showed that the guiding regions of type II waveguides had higher N_{eff} values and slightly higher β values than those of type I waveguides. This was because the n_f values of the SiO2 guiding layers in type II waveguides were much higher than the n_f values of the non-porous regions in the direct-

write guiding layers of type I waveguides. Thus, the cores of type II waveguides had larger aggregate refractive indices than the cores of type I waveguides.

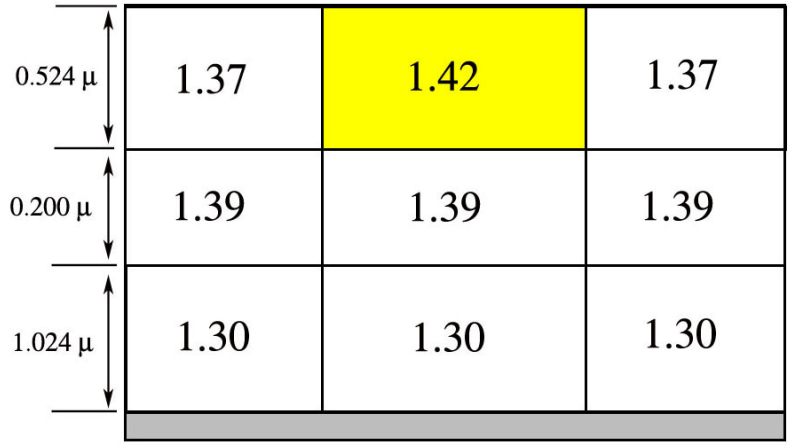

Figure 6.2 – General layout of a fabricated type I waveguide with experimentally measured layer thicknesses and refractive indices shown in their respective positions. Yellow region is the core of the waveguide structure

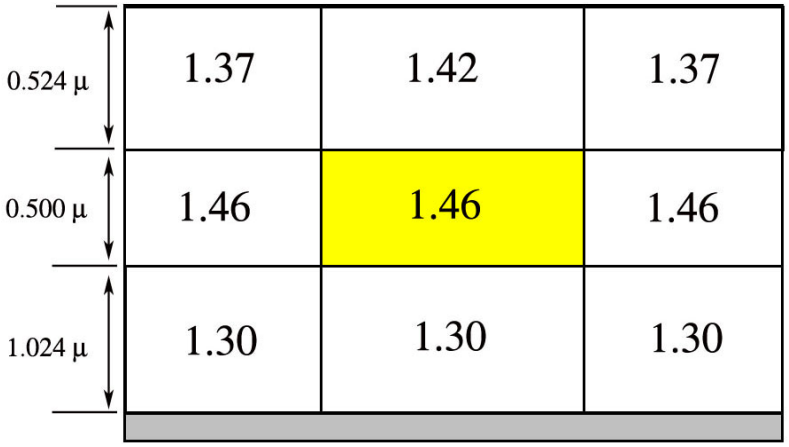

Figure 6.3 – General layout of a fabricated type II waveguide with experimentally measured layer thicknesses and refractive indices shown in their respective positions. Yellow region is the core of the waveguide structure

Table 6.2 – Comparison of overall optical properties of guided TE modes in Figures 6.2 and 6.3, which are typical type I and type II waveguide layouts

Type of waveguide	# guided TE modes supported	Core properties for 1st TE guided Mode		Core properties of core for 2nd TE guided Mode	
		N_{eff}	β (μm^{-1})	N_{eff}	β (μm^{-1})
I	1	1.38	13.65	N/A	N/A
II	2	1.42	14.07	1.35	13.37

Although the PECVD SiO2 layers in type II waveguides could be deposited to wide ranges of thickness and thus support more than two guided modes, it is well known that higher modes have profiles that are less confined, and they tend to have greater propagation losses than the first mode. For this reason, the deposition thickness of SiO_2 layers was intentionally limited to avoid exciting very lossy higher-order modes. Even with the number of modes being limited to only two, optical analyses of the propagation losses of waveguides showed that the second modes were excessively lossy compared to the losses of the first mode, as discussed in the following section.

6.3 Propagation Losses of Type I and Type II Waveguides

Optical characterization experiments showed that the cores of type I and type II porous waveguides had widely spread propagation losses ranging from 16 – 27 dB/cm for the first guided TE mode. As described by Mule, all the exponential fits were done using weighted residuals, with 95% confidence and the R^2 values were above 0.95.[85, 87, 88, 95-100] Figure 6.4, shows a typical exponential fit of the normalized attenuation of the first TE mode propagating along a type I core.

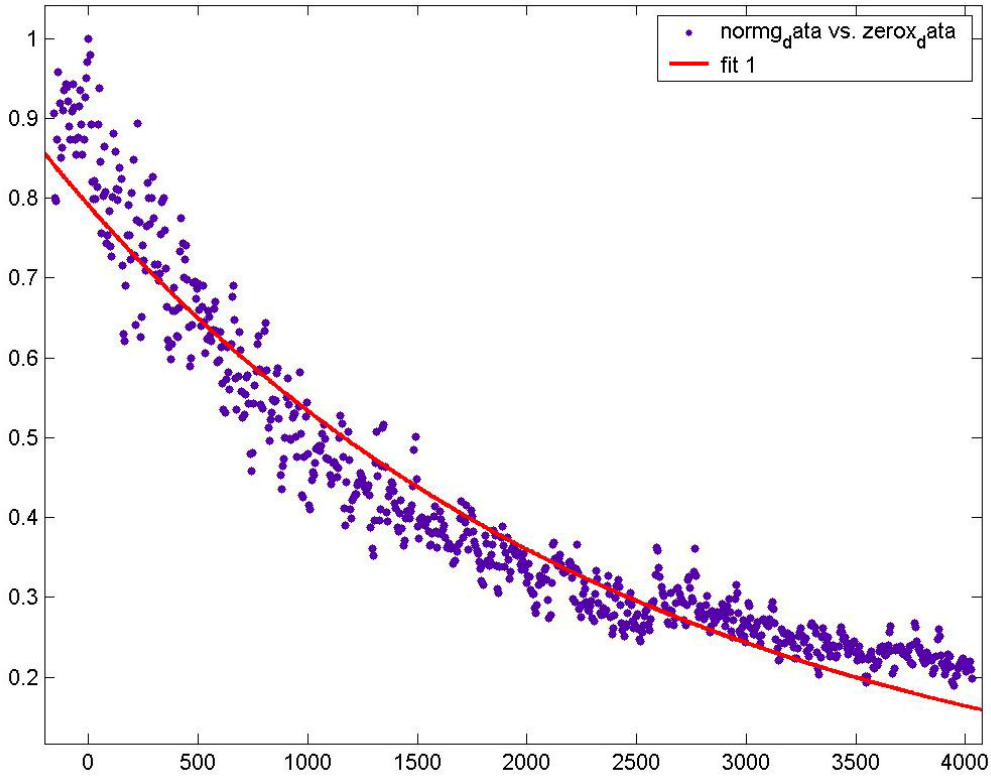

Figure 6.4 – Normalized exponential decay fit of the attenuation the first TE guided mode propagating in a type I waveguide core, which is 18 dB/cm for this sample. The abscissa shows the distance in the z-direction in units of μm.

Interestingly, the attenuation losses for the second guided mode in type II waveguides (type I waveguides could not be fabricated thick enough to support two modes) had a fairly narrow distribution of about 36-40 dB/cm for multiple waveguide cores. Figure 6.5, shows a typical exponential fit of the normalized attenuation of the second TE mode propagating along a type II core. Although it was not unexpected that the second guided modes in type II waveguides would be more lossy than the first guided modes, it was still surprising that the second guided modes have losses almost twice that of the first guided modes. This may be an indication that the large attenuations in waveguides thick enough to support two guided modes was due to mode coupling from

the less-lossy first guided mode to the more lossy guided mode as a result of mode perturbations arising from surface roughness, non-homogenous refractive indices in the porous layers, or Rayleigh scattering from UV-induced macrospores and large collections of UV-induced mesopores within the direct-written layers.[44, 45, 83, 84]

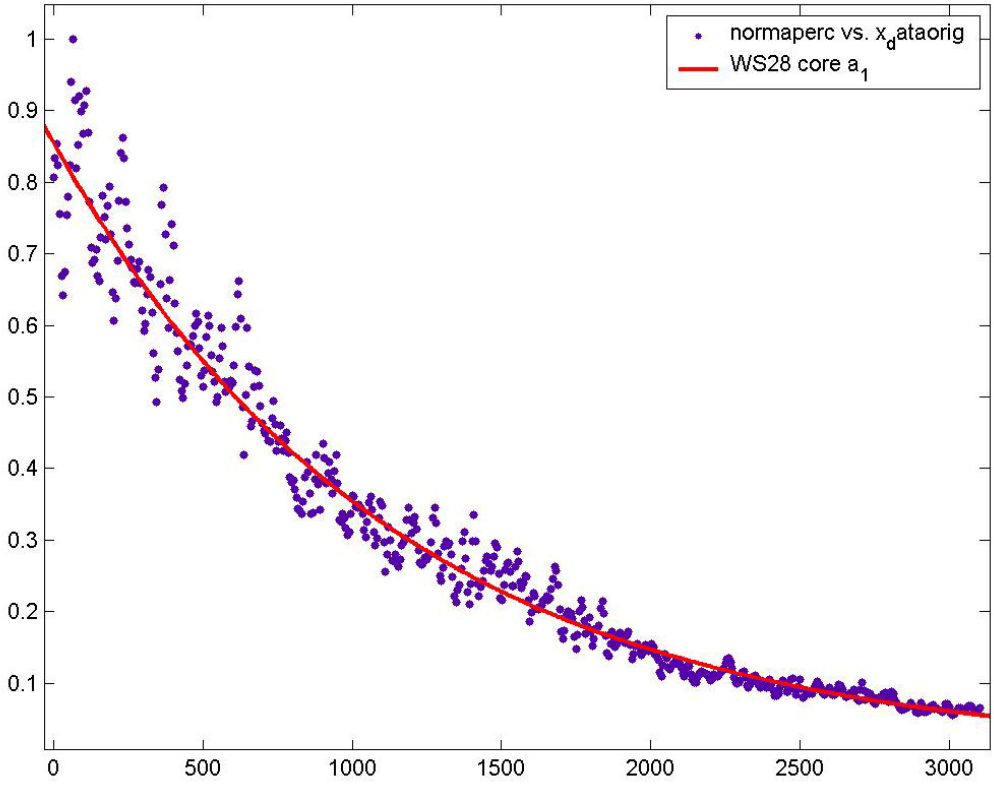

Figure 6.4 – Normalized exponential decay fit of the attenuation the second TE guided mode propagating in a type II waveguide core, which is 40 dB/cm for this sample. The abscissa shows the distance in the z-direction in units of μm.

For both types of porous direct-write waveguides, all the supported TE guided modes had much higher propagation losses than what is acceptable for optoelectronics applications (typical losses along channels are < 1-2 dB/cm).[45, 91, 92, 95, 96] The relatively large UV-induced pores produced in the direct-write layers were likely at least partially responsible for the large propagation loss values, since they would have caused large

amounts of light attenuation due to Rayleigh scattering. The UV-induced pore sizes may have been produced as a result of HSQ film shrinkage caused by gelation and if film shrinkage is reduced, it may result in smaller pore sizes. More work needs to be done in order to identify suitable materials and processing conditions that may allow direct-write porous waveguides to be fabricated with low (< 2 dB/cm) propagation losses.

CHAPTER 7: CONCLUSIONS

Two techniques (solvent-induced and direct-write processing) were developed to create porosity in HSQ films, both of which made use of gelation to crosslink the matrix in the glassy-state. For direct-written and thermal processed porous films with an initial PNC loading of 20%, the lowest refractive indices achieved using were about 1.31 and 1.30, respectively. In comparison, pure HSQ had a refractive index of about 1.39. Lorentz-Lorenz and Maxwell-Garnett mixing rules estimated that thermally-processed and UV-processed films with an initial PNC loading of 20% had induced porosities of about 20-21 vol%.

TEM images showed that closed-cell elongated mesopores and closed-cell elongated macropores were produced in the internal structure of direct-written films. It is believed that the flattened shape of the UV-induced pores was a result of their deformation during film shrinkage, which was caused by the gelation reactions. Although TEM images showed evidence of polymer agglomeration prior to decomposition in thermally-processed porous films, no evidence of phase-segregation was observed in the direct-written porous films, which were processed in the glassy-regime. The lack of phase segregation in direct-written porous films was likely due to low polymer mobility in the glassy phase compared to the rubbery phase. Both thermally-induced and UV-induced porosity caused pits to form on the surface, leading to increases in the surface roughness of films. AFM measurements of films with an initial PNC loading of 20% showed that thermally-processed and direct-written porous films had rms roughness values of about 26 nm and 14 nm, respectively. Based on TEM

results, the lower surface roughness values of direct-written films was due to the lack of agglomeration of mesopores due to low polymer mobility in the glassy phase.

The glass-state solvent-processing method used PC/MIBK co-solvent mixtures as combination gelation agents and pore generators. Solvent processing produced porous films with refractive indices ranging from 1.26-1.30, depending on the bake temperatures used. Based on the Lorentz-Lorenz mixing rule, films with refractive index values of 1.26 were estimated to have induced porosities of 30 vol%. The surfaces of solvent-processed porous films had rms roughness values of 2.7 – 3.3 nm; thus, these films were much smoother than the UV-processed and thermally-processed porous films. Based on desirable processing conditions (low processing complexity, short processing time, low processing temperatures), the high solvent-induced porosities, and smooth surfaces, the solvent-processing method presented in this thesis is a more attractive method for fabricating porous HSQ films than UV-processing.

Two types of slab waveguide structures were fabricated, which used solvent-processed films as the undercladding layers, and the direct-write films as either the guiding layers (type I), or the cover layers (type II). Optical characterization experiments showed that the cores of type I and type II porous waveguides had propagation losses ranging from 16 – 27 dB/cm for the first guided TE mode. The attenuation losses for the second guided mode in type II waveguides were about 36-40 dB/cm (type I waveguides could not be fabricated thick enough to support two modes). The relatively large UV-induced pores produced in the direct-write layers were likely responsible for the large propagation loss values, since they caused large amounts of Rayleigh scattering. The material selection for direct-write processing need to be investigated further to produce

smooth porous films with small, homogeneously- dispersed pores. This would decrease the scattering losses of the waveguides, and thus improve their overall attenuation properties.

REFERENCES

1. Palik, E. D., *Handbook of optical constants*. Academic Press: San Diego, 1998.

2. Sommer, L. H., *Stereochemistry, Mechanism and Silicon; an Introduction to the Dynamic Stereochemistry and Reaction Mechanisms of Silicon Centers*. McGraw-Hill New York, 1965.

3. Maex, K.; Baklanov, M. R.; Shamiryan, D.; Iacopi, F.; Brongersma, S. H.; Yanovitskaya, Z. S., Low dielectric constant materials for microelectronics. *Journal of Applied Physics* **2003,** 93, (11), 8793-8841.

4. Lee, H.-J.; Lin, E. K.; Wang, H.; Wen-li, W.; Wei, C.; Moyer, E. S., Structural comparison of hydrogen silsesquioxane based porous low-k thin films prepared with varying process conditions. *Chemistry of Materials* **2002,** 14, (4), 1845-1852.

5. Padovani, A. M.; Rhodes, L.; Bidstrup Allen, S. A.; Kohl, P. A., Chemically bonded porogens in methylsilsesquioxane. I. Structure and bonding. *Journal of the Electrochemical Society* **2002,** 149, (12), 161-170.

6. Padovani, A. M.; Riester, L.; Rhodes, L.; Bidstrup Allen, S. A.; Kohl, P. A., Chemically bonded porogens in methylsilsesquioxane. II. Electrical, optical, and mechanical properties. *Journal of the Electrochemical Society* **2002,** 149, (12), 171-180.

7. Baklanov, M. R.; Kondoh, E.; Lin, E. K.; Gidley, D. W.; Lee, H. J.; Mogilnikov, K. P.; Sun, J. N., Comparative study of porous SOG films with different non-destructive instrumentation. In *Proceedings of the IEEE 2001 International Interconnect Technology Conference*, Burlingame, CA, USA, 2001; pp 189-191.

8. Baklanov, M. R.; Mogilnikov, K. P., Non-destructive characterisation of porous low-k dielectric films. *Microelectronic Engineering* **2002,** 64, 335-349.

9. Murray, C.; Flannery, C.; Streiter, I.; Schulz, S. E.; Baklanov, M. R.; Mogilnikov, K. P.; Himcinschi, C.; Friedrich, M.; Zahn, D. R. T.; Gessner, T., Comparison of techniques to characterise the density, porosity and elastic modulus of porous low-k SiO_2 xerogel films. *Microelectronic Engineering* **2002,** 60, 133-41.

10. Iacopi, F.; Donaton, R. A.; Coenegrachts, B.; Komiya, T.; Struyf, H.; Lepage, M.; Van Aelst, J.; Boullart, W.; De Roest, D.; Vos, I.; Baklanov, M. R.; Vereecke, G.; Van Hove, M.; Stucchi, M.; Tokei, Z.; Meynen, H.; Bremmer, J. N.; Vanhaelemeersch, S.; Maex, K. In *Studies on XLK film characterization and integration in copper damascene processes*, Proceeding of Advanced Metallization Conference (AMC), held October 2-5 in San Diego, CA, United States and October 19-20 in Tokyo, Japan, 2000; Dan Edelstein, G. D., Yukio Yasuda, Takayuki Ohba, Ed. Materials Research Society, Warrendale, Pa,

USA: held October 2-5 in San Diego, CA, United States and October 19-20 in Tokyo, Japan, 2000; pp 287-293.

11. Sun, J.-N.; Hu, Y.; Frieze, W. E.; Chen, W.; Gidley, D. W., How pore size and surface roughness affect diffusion barrier continuity on porous low-k films. *Journal of the Electrochemical Society* **2003,** 150, (5), 97-101.

12. Wang, J. H.; Chen, W. J.; Chang, T. C.; Liu, P. T.; Cheng, S. L.; Lin, J. Y.; Chen, L. J., Structural and electrical characteristics of low-dielectric constant porous hydrogen silsesquioxane for Cu metallization. *Journal of the Electrochemical Society* **2003,** 150, (8), 141-146.

13. Nahar, R. K., Physical understanding of moisture induced degradation of nanoporous aluminum oxide thin films. *Journal of Vacuum Science & Technology, B: Microelectronics and Nanometer Structures* **2002,** 20, (1), 382-385.

14. Carter, K. R.; DiPietro, R. A.; Sanchez, M. I.; Swanson, S. A., Nanoporous polyimides derived from highly fluorinated polyimide/poly(propylene oxide) copolymers. *Chemistry of Materials* **2001,** 13, (1), 213-21.

15. Labadie, J. W.; Hedrick, J. L.; Wakharkar, V.; Hofer, D. C.; Russell, T. P., Nanopore foams of high temperature polymers. *IEEE Transactions on Components, Hybrids, and Manufacturing Technology* **1992,** 15, (6), 925-30.

16. Hedrick, J. L.; Miller, R. D.; Hawker, C. J.; Carter, K. R.; Volksen, W.; Yoon, D. Y.; Trollsas, M., Templating nanoporosity in thin-film dielectric insulators. *Advanced Materials* **1998,** 10, (13), 1049-1053.

17. Padovani, A. Low Dielectric Constant Porous Spin-on Glass for Microelectronic Applications. PhD, Georgia Institute of Technology, Atlanta, 2002.

18. Padovani, A. M.; Bidstrup Allen, S. A.; Kohl, P. A., Templated nanoporous spin-on glass for high density interconnect applications. In *2002 Proceedings of 8th International Advanced Packaging Materials Symposium*, Institute of Electrical and Electronics Engineers (IEEE), New York, NY, USA: Stone Mountain, GA, USA, 2002; pp 20-24.

19. Padovani, A. M.; Rhodes, L.; Riester, L.; Lohman, G.; Tsuie, B.; Conner, J.; Bidstrup, S. A.; Kohl, P. A., Porous methylsilsesquioxane for low-k dielectric applications. *Electrochemical and Solid-State Letters* **2001,** 4, (11), 25-28.

20. Miller, R. D.; Michl, J., Polysilane high polymers. *Chemical Reviews* **1989,** 89, (6), 1359-1410.

21. Mimura, S.; Naito, H.; Kanemitsu, Y.; Matsukawa, K.; Inoue, H., Optical properties of organic-inorganic hybrid thin films containing polysilane segments prepared from polysilane-methacrylate copolymers. *Journal of Organometallic Chemistry* **2000,** 611, (1-2), 40-44.

22. Miura, S.; Kobayashi, A.; Naito, H.; Matsuura, Y.; Matsukawa, K.; Inoue, H., Photoinduced refractive index changes in organic polysilane-inorganic hybrid thin films. *Synthetic Metals* **2003,** 137, 1405-1406.

23. Nagayama, N.; Shimono, M.; Sato, T.; Yokoyama, M., Refractive index modification due to the Uv-photodecomposition of polysilane and its application as phase mask. *Molecular Crystals and Liquid Crystals Science and Technology, Section A: Molecular Crystals and Liquid Crystals* **2000,** 349, 119-122.

24. Nakayama, Y.; Kurando, T.; Hayashi, H.; Oka, K.; Dohmaru, T. In *Photoinduced annihilation of σ bonds in amorphous poly(methylphenylsilane)*, Kobe, Japan, 1996; Elsevier: Kobe, Japan, 1996; pp 657-60.

25. Watanabe, A.; Ito, O.; Matsuda, M.; Suezawa, M.; Sumino, K., Photodegradation of polysilanes studied by far-infrared spectroscopy. *Japanese Journal of Applied Physics, Part 1 (Regular Papers & Short Notes)* **1994,** 33, (7A), 4133-4.

26. Watanabe, A.; Matsuda, M., Photodegradation of alkyl- and aryl-substituted polysilanes studied by flash photolysis. *Macromolecules* **1992,** 25, (1), 484-488.

27. Matsukawa, K.; Fukui, S.; Higashi, N.; Niwa, M.; Inoue, H., Preparation and properties of organic-inorganic hybrid thin films containing polysilane segments from polysilane-methacrylate copolymers. *Chemistry Letters* **1999**, (10), 1073-1074.

28. Matsukawa, K.; Katada, K.; Nishioka, N.; Matsuura, Y.; Inoue, H., Preparation of photo-induced refractive index pattern using polysilane-silica hybrid thin films. *Journal of Photopolymer Science and Technology* **2004,** 17, (1), 51-52.

29. Matsukawa, K.; Matsuura, Y., Photo-induced optical and chemical properties of polysilane/inorganic nano-hybrids. In *Organic/Inorganic Hybrid Materials-2004. (Materials Research Society Symposium Proceedings)*, Boston, MA, USA, 2005; Vol. 847, pp 45-56.

30. Frechet, J. M. J.; Bouchard, F.; Eichler, E.; Houlihan, F. M.; Iizawa, T.; Kryczka, B.; Willson, C. G., Thermally depolymerizable polycarbonates via acid-catalyzed thermolysis of allylic and benzylic polycarbonates: a new route to resist imaging. *Polymer Journal* **1987,** 19, (1), 31-49.

31. Jayachandran, J. P.; Reed, H. A.; Zhen, H.; Rhodes, L. F.; Henderson, C. L.; Bidstrup, S. A.; Kohl, P. A., Air-channel fabrication for microelectromechanical systems via sacrificial photosensitive polycarbonates. *Journal of Microelectromechanical Systems* **2003,** 12, (2), 147-159.

32. Crivello, J. V., *Chemistry of Photoacid Generating Compounds*. ACS: Washington DC, USA, 1989; Vol. 61, p 62-66.

33. Crivello, J. V., Discovery and development of onium salt cationic photoinitiators. *Journal of Polymer Science, Part A: Polymer Chemistry* **1999,** 37, (23), 4241-4254.

34. Crivello, J. V.; Kong, S., Photoinduced and thermally induced cationic polymerizations using dialkylphenacylsulfonium salts. *Macromolecules* **2000,** 33, (3), 833-842.

35. Crivello, J. V.; Lam, J. H. W., New Photoinitiators for Cationic Polymerization. *Journal of Polymer Science, Polymer Symposia* **1977**, (56), 383-395.

36. Crivello, J. V.; Lam, J. H. W., Photoiniated Cationic Polymerization by Diarylchloronium and Diarylbromonium Salts. *Journal of Polymer Science, Polymer Letters Edition* **1978,** 16, (11), 563-571.

37. Crivello, J. V.; Lee, J. L., Complex Triarylsulphonium Salt Photoiniators. *Polymer Photochemistry* **1982,** 2, (3), 219-226.

38. Crivello, J. V.; Ma, J.; Jiang, F., Synthesis and photoactivity of novel 5-arylthianthrenium salt cationic photoinitiators. *Journal of Polymer Science, Part A: Polymer Chemistry* **2002,** 40, (20), 3465-3480.

39. Fouassier, J. P.; Burr, D.; Crivello, J. V., Photochemistry and photopolymerization activity of diaryliodonium salts. *Journal of Macromolecular Science - Pure and Applied Chemistry* **1994,** A31, (6), 677-701.

40. Shirai, M.; Suyama, K.; Okamura, H.; Tsunooka, M., Development of novel photosensitive polymer systems using photoacid and photobase generators. *Journal of Photopolymer Science and Technology* **2002,** 15, (5), 715-30.

41. Shirai, M.; Tsunooka, M., Photoacid and photobase generators: chemistry and applications to polymeric materials. *Progress in Polymer Science* **1996,** 21, (1), 1-45.

42. Yi, D. K.; Kim, D.-Y., Novel approach to the fabrication of macroporous polymers and their use as a template for crystalling nanorings. *Nanoletters* **2002,** 3, (2), 207-211.

43. Cai, Q.; Yang, J.; Bei, J.; Wang, S., A novel porous cells scaffold made of polyactide-dextran blend combining phase-separation and particle-leaching techniques. *Biomaterials* **2002,** 23, 4483-4492.

44. Tummala, R. R., *Fundamentals of microsystems packaging* McGraw-Hill: New York, 2001.

45. Wong, C. P., *Polymers for electronic and photonic applications*. Academic Press: Boston, 1993.

46. Chae, K. H.; Sung, K. H., A polymeric photobase generator containing oxime-urethane groups: Crosslinking reaction and application to negative photoresist. *Journal of Polymer Science, Part A: Polymer Chemistry* **2004,** 42, (4), 975-984.

47. Frechet, J. M. J.; Cameron, J. F., Photogenerated amines and diamines. Novel curing systems for thin film coatings. In *Polymeric Materials Science and Engineering, Proceedings of the ACS Division of Polymeric Materials Science and Engineering*,

American Chemical Society (ACS), Columbus, OH, USA: Atlanta, GA, USA, 1991; Vol. 64, pp 55-56.

48. Winkle, M. R. a.; Graziano, K. A., Acid-hardening positive photoresist using photochemical generation of base. *Journal of Photopolymer Science and Technology* **1990,** 3, (3), 419-422.

49. Xu, Y.; Zheng, D. W.; Tsai, Y.; Tu, K. N.; Zhao, B.; Liu, Q. Z.; Brongo, M.; Ong, C. W.; Choy, C. L.; Sheng, G. T. T.; Tung, C. H., Synthesis and characterization of porous polymeric low dielectric constant films. *Journal of Electronic Materials* **2001,** 30, (4), 309-313.

50. Baklanov, M. R.; Mogilnmov, K. P., Characterization of porous dielectric films by ellipsometric porosimetry. *Optica Applicata* **2000,** 30, 491-6.

51. Iacopi, F.; Baklanov, M. R.; Sleeckx, E.; Conard, T.; Bender, H.; Meynen, H.; Maex, K., Properties of porous HSQ-based films capped by plasma enhanced chemical vapor deposition dielectric layers. *Journal of Vacuum Science and Technology B: Microelectronics and Nanometer Structures* **2002,** 20, 109-115.

52. Jin, C.; Luttmer, J. D.; Smith, D. M.; Ramos, T. A., Nanoporous silica as an ultralow-k dielectric. *MRS Bulletin* **1997,** 22, (10), 39-42.

53. Jin, C.; List, S.; Yamanaka, S.; Lee, W. W.; Taylor, K.; Hsu, W.-Y.; Olsen, L.; Luttmer, J. D.; Havemann, R.; Smith, D.; Ramos, T.; Maskara, A., Deposition and characterization of porous silica xerogel films. *Materials Research Society Symposium Proceedings* **1997,** 443, (Low-Dielectric Constant Materials II), 99-104.

54. Iler, R. K., *The chemistry of silica: solubility, polymerization, colloid and surface properties, and biochemistry*. Wiley: New York, 1979.

55. Suh, J. M.; Bae, S. J.; Jeong, B., Thermogelling multiblock poloxamer aqueous solutions with closed-loop sol-gel-sol transitions upon increasing pH. *Advanced Materials* **2005,** 17, (1), 118-120.

56. SIA, *International Technology Roadmap for Semiconductors: 2003 Edition*. Semiconductor Industry Association: San Jose, 2003.

57. Liou, H.-C.; Pretzer, J., Effect of curing temperature on the mechanical properties of hydrogen silsesquioxane thin films. *Thin Solid Films* **1998,** 335, (1-2), 186-191.

58. Liu, W.-C.; Yang, C.-C.; Chen, W.-C.; Dai, B.-T.; Tsai, M.-S., The structural transformation and properties of spin-on poly(silsesquioxane) films by thermal curing. *Journal of Non-Crystalline Solids* **2002,** 311, (3), 233-240.

59. Bremmer, J. N.; Gray, D.; Liu, Y.; Gruszynski, K.; Marcus, S., Rapid thermal processing of hydrogen silsesquioxane for low dielectric constant performance. In *Low-Dielectric*

Constant Materials V (Materials Research Society Symposium Proceedings), San Francisco, CA, USA, 1999; Vol. 565, pp 273-278.

60. Bremmer, J. N.; Liu, Y.; Gruszynski, K. G.; Dall, F. C., cure of hydrogen silsesquioxane for intermetal dielectric applications. In *Low-Dielectric Constant Materials III (Materials Research Society Symposium Proceedings)*, San Francisco, CA, USA, 1997; Vol. 476, pp 37-44.

61. Harrison, P. G., Silicate cages: precursors to new materials. *Journal of Organometallic Chemistry* **1997,** 542, (2), 141-183.

62. Jousseaume, V.; Fayolle, M.; Guedj, C.; Haumesser, P. H.; Huguet, C.; Pierre, F.; Pantel, R.; Feldis, H.; Passemard, G., Pore sealing of a porous dielectric by using a thin PECVD a-SiC:H conformal liner. *Journal of the Electrochemical Society* **2005,** 152, (10), 156-161.

63. Siew, Y. K.; Sarkar, G.; Hu, X.; Hui, J.; See, A.; Chua, C. T., Thermal curing of hydrogen silsesquioxane. *Journal of the Electrochemical Society* **2000,** 147, (1), 335-339.

64. Toivola, Y.; Thurn, J.; Cook, R. F., Structural, electrical, and mechanical properties development during curing of low-k hydrogen silsesquioxane films. *Journal of the Electrochemical Society* **2002,** 149, (3), 9-17.

65. Yang, C.-C.; Chen, W.-C., The structures and properties of hydrogen silsesquioxane (HSQ) films produced by thermal curing. *Journal of Materials Chemistry* **2002,** 12, (4), 1138-1141.

66. Lifshitz, N.; Lai, W. Y. C.; Smolinsky, G., Water-related degradation of contacts in the multilevel MOS IC with spin-on glasses as interlevel dielectrics. *IEEE Electron Device Letters* **1989,** 10, (12), 562-564.

67. Noguchi, J.; Ohashi, N.; Jimbo, T.; Yamaguchi, H.; Takeda, K.-i.; Hinode, K., Effect of NH_3-plasma treatment and CMP modification on TDDB improvement in CU metallization. *IEEE Transactions on Electron Devices* **2001,** 48, (7), 1340-1345.

68. Yu, S.; Wong, T. K. S.; Hu, X.; PITA, K., The Effect of TEOS/MTES Ratio on the Structural and Dielectric Properties of Porous Silica Films. *Journal of The Electrochemical Society* **2003,** 150, (5), 116-121.

69. Kim, K.-M.; Chujo, Y., Polymer Hybrids with Functionalized Silsesquioxanes via Two Physical Interactions in One System. *Journal of Polymer Science Part A: Polymer Chemistry* **2003,** 41, 1306-1315.

70. Kim, S. M.; Yoon, D. Y.; Nguyen, C. V.; Han, J.; Jaffe, R., L. In *Experimental and theoretical study of structure-dielectric property relationships for polysilsesquioxanes*, Low-Dielectric Constant Materials IV (Mat. Res. Soc. Symp. Proc., vol 115), San Francisco, CA, 1998; Materials Research Society, Warrendale, Pennsylvania: San Francisco, CA, 1998.

71. Yim, J.-H.; Baklanov, M. R.; Gidley, D. W.; Peng, H.; Jeong, H.-D.; Pu, L. S., Pore structure of modified cyclic silsesquioxane thin films made porous using a cyclodextrins-based porogen. *Journal of Physical Chemistry B* **2004,** 108, (26), 8953-8959.

72. Zhong, B. M., H.; Iocopi, F.; Weidner, K.; Mailhouitre, S.; Moyer, E.; Bargeron, C.; Schalk, P.; Peck, A.; Hove, M.V.; Maex, K., A new ultra-low K ILD material based on organic-inorganic hybrid resins. In *Materials Research Society Symposium Proceedings*, San Francisco, CA, USA, 2002; Vol. 716, pp 575-580.

73. Guizhi Li; Lichang Wang; Hanli Ni; Jr., C. U. P., Polyhedral Oligomeric Silsesquioxane (POSS) Polymers and Copolymers: A Review. *J. Inorganic and Organometallic Polymers* **2001,** 11, (3), 123-154.

74. Lee, H. J.; Lin, E. K.; Wu, W. L.; Fanconi, B. M.; Lan, J. K.; Cheng, Y. L.; Liou, H. C.; Feng, M. S.; Chao, C. G., X-Ray Reflectivity and FTIR Measurements of N2 Plasma Effects on the Density Profile of Hydrogen Silsesquioxane Thin Films. *Journal of The Electrochemical Society* **2001,** 148, (10), 195-199.

75. Gorman, B. P.; Mueller, D. W.; Chyan, O.; Reidy, R. F., Analytical TEM characterization of metal penetration and supercritical pore-sealing of ash-damaged porous low-k dielectrics. In *Advanced Metallization Conference 2005 (AMC 2005) Proceedings*, 2006 ed.; Colorado Springs, CO, USA, 2006; pp 392-397.

76. Baklanov, M. R.; Mogilnikov, K. P.; Jin-Heong, Y., Ellipsometric porosimetry of porous low-k films with quasi-closed cavities. In *Materials Research Society Proceedings*, San Francisco, CA, USA, 2004; Vol. 812, pp 55-60.

77. Baklanov, M. R.; Mogilnikov, K. P.; Polovinkin, V. G.; Dultsev, F. N., Determination of pore size distribution in thin films by ellipsometric porosimetry. *Journal of Vacuum Science & Technology B (Microelectronics and Nanometer Structures)* **2000,** 18, (3), 1385-91.

78. Furusawa, T.; Ryuzaki, D.; Yoneyama, R.; Homma, Y.; Kenji, H., Oxygen Plasma Resistance of Low-k Organosilica Glass Films. *Electrochemical and Solid State Letters* **2001,** 4, (3), 31-34.

79. Xu, J.; Moxom, J.; Yang, S.; Suzuki, R.; Ohdaira, T., Porosity in porous methyl-silsesquioxane (MSQ) films. *Applied Surface Science* **2002,** 194, 189-194.

80. Iacopi, F.; Tokei, Z.; Le, Q. T.; Shamiryan, D.; Conard, T.; Brijs, B.; Kreissig, U.; Van Hove, M.; Maex, K., Factors affecting an efficient sealing of porous low-k dielectrics by physical vapor deposition Ta(N) thin films. *Journal of Applied Physics* **2002,** 92, (3), 1548.

81. Hu, J. C.; Wu, C. W.; Gau, W. C.; Chen, C. P.; Chen, L. J.; Li, C. H.; Chang, T. C.; Chu, C. J., Self-organized nanomolecular films on low-dielectric constant porous methyl silsesquioxane at room temperature. *Journal of the Electrochemical Society* **2003,** 150, (4), 61-66.

82. Dagenais, M.; Leheny, R. F.; Crow, J., *Integrated Optoelectronics*. Academic Press: San Diego, 1995.

83. Tamaki, K.; Takase, H.; Eriyama, Y.; Ukachi, T., Recent progress on polymer waveguide materials. *Journal of Photopolymer Science and Technology* **2003,** 16, (5), 639-48.

84. Nishihara, H.; Haruna, M.; Toshiaki, S., *Optical Integrated Circuits*. McGraw-Hill: New York, 1989.

85. Egorov, A. A., Theory of Waveguide Light Scattering in an Integrated Optical Waveguide in the Presence of Noise. *Radiophysics and Quantum Electronics* **2005,** 48, (1), 57-67.

86. Foley, B. M.; Melman, P.; Vo, K. T., Novel Loss Measurement Technique for Optical Waveguides by Imaging of Scattered Light. *Electronics Letters* **1992,** 28, (6), 584-585.

87. Imai, M.; Koseki, M.; Ohtsuka, Y., Light Scattering from a glass thin-film optical waveguide. *Journal of Applied Physics* **1981,** 52, (11), 6506-6508.

88. Miyanaga, S.; Imai, M.; Asakura, T., Radiation Pattern of Light Scattering from the Core Region of Dielectric-Slab-Optical-Waveguides. *IEEE Journal of Quantum Electronics* **1978,** 14, (1), 30-37.

89. Mule, A. V. Volume grating coupler-based optical interconnect technologies for polylithic gigascale integration. Georgia Institute of Technology, Atlanta, 2004.

90. Tsushima, H.; Watanabe, E.; Yoshimatsu, S.; Okamoto, S.; Oka, T.; Imoto, K., Novel manufacturing process of waveguide using selective photobleaching of polysilane films by UV light irradiation. In *Proceedings of SPIE Conference*, 1 ed.; SPIE-Int. Soc. Opt. Eng: Orlando, FL, USA, 2003; Vol. 5246, pp 119-30.

91. Yeatman, E. M.; Dawnay, E. J. C., Doped Sol-Gel Films for Silica-on-Silicon Photonic Components. *Journal of Sol-Gel Science and Technology* **1997,** 8, 1007-1011.

92. Yeatman, E. M.; Pita, K.; Ahmad, M. M.; Vannucci, A.; Fiorello, A., Strip-Loaded High-Confinement Waveguides for Photonic Applications. *Journal of Sol-Gel Science and Technology* **1998,** 13, 517-521.

93. Kraus, J. D., *Electromagnetics: with applications*. 5th ed.; McGraw-Hill: Boston, 1999.

94. Rao, N. N., *Elements of Engineering Electromagnetics*. 4th ed.; Prentice Hall: Englewood Cliffs, New Jersey, 1994.

95. Hattori, H.; Sakaguchi, S.; Kanamori, T.; Terunuma, Y., Scattering characteristics of crystallites in fluoride optical fibers. *Applied Optics* **1987,** 26, (13), 2683-2687.

96. Keast, D. J.; Storey, B. E., A possible contribution to light loss in calcium tungstate and yttrium aluminium garnet laser crystals by scattering. *BRIT. J. APPL. PHYS. (J. PHYS. D)* **1968,** 1, 524-527.

97. Pirasteh, P.; Charrier, J.; Dumeige, Y.; Joubert, P.; Haesaert, S.; Chaillou, A.; Haji, L.; Le Rendu, P.; Nguyen, T. P., Light propagation and scattering in porous silicon nanocomposite waveguides. *Physica Status Solidi, Part a* **2005,** 202, (8), 1712–1716.

98. Walter, D. J.; Houghton, J., Attenuation in Thin Film Optical Waveguides due to Roughness-Induced Mode Coupling. *Thin Solid Films* **1978,** 52, 461-476.

99. Li, H.; Torrance, K. E., An experimental study of the correlation between surface roughness and light scattering for rough metallic surfaces. In *Proceedings of SPIE Vol. 5878 (Advanced Characterization Techniques for Optics, Semiconductors, and Nanotechnologies II)*, SPIE, Bellingham, WA: 2005.

100. Yegorov, A. A., Use of waveguide light scattering for precision measurements of the statistical parameters of irregularities of integrated optical waveguide materials. *Optical Engineering* **2005,** 44, (1), 14601-1-10.

101. Blanc, D.; Pelissier, S.; Saravanamuttu, K.; Najafi, S. I.; Andrews, M. P., Self-Processing of Surface-Relief Gratings in Photosensitive Hybrid Sol-Gel Glasses. *Advanced Materials* **1999,** 11, (18), 1508-1511.

102. Heaney, A. D.; Erdogan, T., Solgel-derived photosensitive germanosilicate glass monoliths. *Optics Letters* **2000,** 25, (24), 1765-1767.

103. Matsuura, Y.; Miura, S.; Naito, H.; Inoue, H.; Matsukawa, K., Preparation of porous titania thin films from polysilane-titania hybrid by UV irradiation. *Journal of Photopolymer Science and Technology* **2002,** 15, (5), 761-4.

104. Nakayama, Y.; Kurando, T.; Hayashi, H.; Oka, K.; Dohmaru, T., Photoinduced annihilation of σ bonds in amorphous poly(methylphenylsilane). *J. Non-Cryst. Solids* **1996,** 198-200, 657-660.

105. Cameron, J. F.; Grant Willson, C.; Frechet, J. M. J., Photogeneration of amines from α-keto carbamates: Photochemical Studies. *Journal of the American Chemical Society* **1997,** 118, 12925-12937.

106. Sarker, A. M.; Lungu, A.; Mejiritski, A.; Kaneko, Y.; Neckers, D. C., Tetraorganylborate salts as convenient precursors for photogeneration of tertiary amines. *Journal of the Chemical Society. Perkin Transactions 2* **1998**, (10), 2315-2331.

107. Epling, G. A.; Walker, M. E., A new photochemically removable protecting group for amines. *Tetrahedron Letters* **1982,** 23, (38), 3843-3846.

108. Matuszczak, S.; Cameron, J. F.; Frechet, J. M. J.; Wilson, C. G., Photogenerated amines and their use in the design of a positive-tone resist material based on electrophilic aromatic substitution. *Journal of Materials Chemistry* **1991,** 1, (6), 1045-50.

109. Tsunooka, M.; Tachi, H.; Yamamoto, T.; Shirai, M., Quaternary ammonium N,N-dimethyldithiocarbamates as photobase generators. *Polymer Preprints (American Chemical Society, Division of Polymer Chemistry)* **2001,** 42, (2), 720-721.

110. Chae, K. H.; Jang, D.-J., A new photobase generator containing oxime-urethane group and its application. *Macromolecular Symposia* **1999,** 142, (Advanced Polymeric Materials), 173-183.

111. Chae, K. H.; Song, H. B., Crosslinking reaction of glycidyl methacrylate copolymers containing oxime-urethane groups using photogenerated pendant amines. *Polymer Bulletin* **1998,** 40, (6), 667-674.

112. Harkness, B. R.; Takeuchi, K.; Tachikawa, M., Demonstration of a directly photopatternable spin-on-glass based on hydrogen silsesquioxane and photobase generators. *Macromolecules* **1998,** 31, (15), 4798-4805.

113. Harkness, B. R.; Takeuchi, K.; Tachikawa, M., Photopatternable thin films from silyl hydride containing silicone resins and photobase generators. *Polymers for Advanced Technologies* **1999,** 10, (11), 669-677.

114. Cameron, J. F.; Frechet, J. M. J., Photogeneration of organic bases from *o*-nitrobenzyl-derived carbamates. *Journal of the American Chemical Society* **1991,** 113, (11), 4303-4313.

115. Jensen, K. H.; Hanson, J. E., Synthesis and Photochemistry of Tertiary Amine Photobase Generators. *Chemistry of Materials* **2002,** 14, (2), 918-923.

116. Sarker, A. M.; Kaneko, Y.; Nikolaitchik, A. V.; Neckers, D. C., Photoinduced electron-transfer reactions: highly efficient cleavage of C-N bonds and photogeneration of tertiary amines. *Journal of Physical Chemistry A* **1998,** 102, (28), 5375-5382.

117. Willson, C. G.; Cameron, J. F.; Frechet, J. M. J. In *Photogeneration of amines and application to chemically amplified resist design*, Polymeric Materials Science and Engineering, Proceedings of the ACS Division of Polymeric Materials Science and Engineering, New Orleans, LA, USA, 1996; New Orleans, LA, USA, 1996; p 437.

118. Reynolds, L.; Gardecki, J. A.; Frankland, S. J. V.; Horng, M. L.; Maroncelli, M., Dipole Solvation in Nondipolar Solvents: Experimental Studies of Reorganization Energies and Solvation Dynamics. *Journal of Physical Chemistry* **1996,** 100, 10337-10354.

119. Riddick, J. A.; Bunger, W. B.; Sakano, T. K., *Organic Solvents*. Wiley: New York, 1986.

120. Dean, J. A., *Lange's Handbook of Chemistry*. 15th ed.; McGraw-Hill: New York, 1999.

121. Zhou, Y.; Yi, T.; Li, T.; Zhou, Z.; Li, F.; Huang, W.; Huang, C., Morphology and wettability tunable two-dimensional superstructure assembled by hydrogen bonds and hydrophobic interactions. *Chemistry of Materials* **2006,** 18, (13), 2974-2981.

122. Loy, D. A.; Mather, B.; Straumanis, A. R.; Baugher, C.; Schneider, D. A.; Sanchez, A.; Shea, K. J., Effect of pH on the gelation time of hexylene-bridged polysilsesquioxanes. *Chemistry of Materials* **2004,** 16, (11), 2041-2043.

123. Oliver, W. C.; Pharr, G. M., Improved technique for determining hardness and elastic modulus using load and displacement sensing indentation experiments. *Journal of Materials Research* **1992,** 7, (6), 1564-1580.

124. Friedrich, M.; Wagner, T.; Salvan, G.; Park, S.; Kampen, T. U.; Zahn, D. R. T., Optical constants of 3,4,9,10-perylenetetracarboxylic dianhydride films on silicon and galliumarsenide studied by spectroscopic ellipsometry. *Applied Physics A: Materials Science & Processing* **2001,** 75, (4), 501-506.

125. Maxwell-Garnett, J. C., Colours in Metal Glasses, in Metallic Films, and in Metallic Solutions II. *Philosophical Transactions of the Royal Society of London. Series A, Containing Papers of a Mathematical or Physical Character* **1906,** 205, 237-288.

126. Lorentz, H. A., *The Theory of Electrons*. G.P. Stechert & Co.: New York, USA, 1906.

127. Choy, T. C., *Effective Medium Theory: Principles and Applications*. Oxford University Press USA: New York, USA, 1999.

128. Sathiarajy, T. S.; Thangarajz, R., The experimental and calculated optical properties of Ni–Al_2O_3 coatings using effective medium theories. *J. Phys. D: Appl. Phys.* **1997,** 30, (5), 769–775.

129. Anemogiannis, E.; Glytsis, E. N.; Gaylord, T. K., Efficient Solution of Eigenvalue Equations of Optical Waveguiding Structures. *Journal of Lightwave Technology* **1994,** 12, (12), 2080-2084.

130. Iacopi, F.; Donaton, R. A.; Coenegrachts, B.; Komiya, T.; Struyf, H.; Lepage, M.; Van Aelst, J.; Boullart, W.; De Roest, D.; Vos, I.; Baklanov, M. R.; Vereecke, G.; Van Hove, M.; Stucchi, M.; Tokei, Z.; Meynen, H.; Bremmer, J. N.; Vanhaelemeersch, S.; Maex, K., Studies on XLK film characterization and integration in copper damascene processes. *Advanced Metallization Conference 2000, Proceedings of the Conference, San Diego, CA, United States, Oct. 2-5 and University of Tokyo, Tokyo, Japan, Oct. 19-20, 2000* **2000**, 287-293.

131. Shea, K. J.; Loy, D. A., A Mechanistic Investigation of Gelation. The Sol-Gel Polymerization of Precursors to Bridged Polysilsesquioxanes. *Acc. Chem. Res.* **2001,** 34, (9), 707-716.

132. Brook, M. A., *Silicon in Organic, Organometallic, and Polymer chemistry* John Wiley & Sons: New York 2000.

133. West, R., Cyclic organosilicon compounds. II. Ring size and reactivity in the alkali-catalyzed hydrolysis of silanes. *Journal of the American Chemical Society* **1954,** 76, 6015-17.

134. Sommer, L. H., *Stereochemistry, mechanism and silicon; an introduction to the dynamic stereochemistry and reaction mechanisms of silicon centers*. McGraw-Hill New York, 1965; p 189.

135. Lee, S. K.; Jung, B.-J.; Ahn, T.; Song, I.; Shim, H.-K., Photolithographic Micropatterning of an Electroluminescent Polymer Using Photobase Generator. *Macromolecules* **2003,** 36, (24), 9252-9256.

136. Tagawa, S.; Nagahara, S.; Iwamoto, T.; Wakita, M.; Kozawa, T.; Yamamoto, Y.; Werst, D.; Trifunac, A. D., Radiation and photochemistry of onium salt acid generators in chemically amplified resists. In *Advances in Resist Technology and Processing XVII*, Houlihan, F. M., Ed. Society of Photo-Optical Instrumentation Engineers, Bellingham, WA, USA: Santa Clara, CA, USA, 2000; Vol. 3999 (I), pp 204-213.

137. Dektar, J. L.; Hacker, N. P., Photochemistry of triarylsulfonium salts. *Journal of the American Chemical Society* **1990,** 112, (16), 6004-15.

138. Rajapakse, N.; Finston, H. L.; Frled, V., Liquid-Liquid Phase Equilibria in the Propylene Carbonate + Methyl Isobutyl Ketone + Water System. *Journal of Chemical and Engineering Data* **1986,** 31, (4), 408-410.